Investigation of Particle Dynamics in Complex Plasma with PK-4

Lukas Wimmer

Gießen 2025

Investigation of Particle Dynamics in Complex Plasma with PK-4

Lukas Wimmer

Dissertation
der Fakultät für Physik
der Justus-Liebig-Universität
Gießen

vorgelegt von
Lukas Wimmer
aus Braunau am Inn

Gießen, den 30.04.2025

Erstgutachter: Professor Dr. Markus Thoma
Zweitgutachter: Professor Dr. Simone Sanna
Tag der mündlichen Prüfung: 07.07.2025

Contents

List of Figures

Zusammenfassung

Komplexe Plasmen sind Niedertemperaturplasmen, die mikrometergroße geladene Partikel enthalten, welche durch Coulomb-Wechselwirkungen miteinander interagieren. Diese Partikel erwerben in der Plasmakomponente durch die Aufnahme von Elektronen und Ionen eine signifikante negative Ladung. Dadurch entstehen gekoppelte Systeme, in denen kollektive Phänomene wie Kristallisation, Phasenübergänge und Wellenausbreitung direkt auf Teilchenskala beobachtet werden können. Das PK-4 Experiment bietet eine einzigartige Plattform zur Untersuchung dieser Phänomene unter gut kontrollierten Laborbedingungen. Die Experimente können sowohl unter Erdschwerebedingungen als auch in Mikrogravitation – etwa während Parabelflugkampagnen oder an Bord der Internationalen Raumstation – durchgeführt werden.

Diese Arbeit präsentiert eine umfassende Untersuchung der Partikeldynamik in komplexen Plasmen mithilfe des PK-4 Experiments. Der Schwerpunkt liegt auf dem Verhalten von Staubakustikwellen, elektroreologischen Effekten und der Ionenreibungskraft. Um die Herausforderungen bei der Detektion schnell bewegter und schwach beleuchteter Partikel zu bewältigen und eine statistisch signifikante Datenauswertung zu gewährleisten, wurden fortschrittliche Bildverarbeitungstechniken und automatisierte Auswertungsmethoden entwickelt. Dazu gehören der Einsatz von Hochgeschwindigkeitskameras sowie durch maschinelles Lernen verbesserte Werkzeuge zur Signalanalyse und Trajektorienrekonstruktion.

Ein zentrales Ergebnis ist die Identifikation und Rekonstruktion geneigter Wellenfronten in Staubakustikwellen. Diese zeigen Abweichungen von idealisierten theoretischen Vorhersagen, was auf die kombinierte Wirkung von Schwerkraft und Randeffekten zurückzuführen ist. Eine beobachtete räumliche Verschiebung der Wellenstruktur, die zu Asymmetrien in der Ausbreitung führt, konnte auf zusätzliche elektrische Felder zurückgeführt werden. Darüber hinaus wurde der Einfluss elektroreologischer Effekte auf die Wellenausbreitung unter Mikrogravitation sowohl experimentell als auch durch Modellierung der Ladungsverteilung bestätigt. Erstmals konnte die Kristallisation eines Partikelsystems beobachtet werden, das sich während des Ordnungsprozesses in Bewegung befand. Die Bildung von kettenartigen Partikelstrukturen wurde mit Ladungsverschiebungen in Verbindung gebracht, die durch elektroreologische Effekte beeinflusst wurden. Im finalen Projekt wurde die auf einzelne Mikropartikel wirkende Ionenreibungskraft mittels eines datengetriebenen Verfahrens auf Basis der Bayes'schen Optimierung quantifiziert. Diese Methode ermöglichte die Extraktion wichtiger Plasmaparameter und bestätigte an-

alytische Kraftmodelle, was zu einem tieferen Verständnis der Ladungsdynamik und der Partikel-Ionen-Wechselwirkungen führte.
Zusammenfassend zeigt diese Arbeit, dass die Kombination moderner datenwissenschaftlicher Methoden mit der experimentellen Plasmaphysik unter gut kontrollierten Bedingungen zu einer signifikanten Verbesserung der Messgenauigkeit führt. Dies trägt wesentlich zum Verständnis fundamentaler plasmaphysikalischer Prozesse bei. Die entwickelten Methoden und erzielten Ergebnisse leisten einen wichtigen Beitrag zum tieferen Verständnis des Verhaltens komplexer Plasmen und schaffen eine Grundlage für zukünftige Untersuchungen sowohl in erdgebundenen als auch in weltraumbasierten Plasmasystemen. Die vorgestellten Open-Source-Methoden dienen als Grundlage für die Weiterentwicklung von Modellen und die Analyse zukünftiger Experimente mit verbesserter statistischer Auswertung.

Summary

Complex plasmas are low temperature plasmas containing micrometer-sized charged particles that exhibit Coulomb interactions. When introduced into the plasma environment, these particles acquire a significant negative charge by collecting electrons and ions. This leads to the formation of coupled systems where collective effects such as crystallization, phase transitions, and wave propagation can be observed directly at the particle scale. The PK-4 experiment offers a unique platform for investigating these phenomena under well-controlled laboratory conditions. Experiments can be conducted both on the ground and in microgravity environments, such as during parabolic flight campaigns and aboard the International Space Station.

This thesis presents a detailed investigation of particle dynamics in complex plasmas using the PK-4 facility. The primary focus is placed on the behavior of dust acoustic waves, electrorheological effects, and the ion drag force. To address the challenges of detecting fast-moving and weakly illuminated particles to ensure a statistically significant data analysis, advanced image processing techniques and automated evaluation methods were developed. These include the use of high speed digital cameras and machine learning–enhanced tools for signal enhancement and trajectory reconstruction.

One of the key findings is the identification and reconstruction of tilted wavefronts in dust acoustic waves. These wavefronts exhibit deviations from ideal theoretical predictions due to the combined influence of the gravitational force and boundary effects. A spatial shift in the wave structure, leading to asymmetries in propagation, is shown to be induced by additional electric fields. Furthermore, the influence of electrorheological effects on wave propagation under microgravity conditions was confirmed through experimental observations and charge distribution modeling. For the first time, crystallization was observed in a particle system that remained in motion throughout the process. The formation of string-like particle arrangements was found to be linked to charge distributions shaped by electrorheological interactions. Finally, the ion drag force acting on individual microparticles was quantified using a data driven approach based on Bayesian optimization. This method allowed for the extraction of key plasma parameters and provided validation of analytical force models, yielding deeper insight into charge dynamics and particle ion interactions.

In conclusion, the integration of modern data science techniques with experimental plasma physics conducted under well-controlled conditions has led to significant improvements in measurement precision. This, in turn, has enhanced the understanding of fundamental

plasma physical processes. The methods and results presented in this work contribute to a deeper insight into the behavior of complex plasmas and lay the groundwork for future investigations in both terrestrial and space based plasma environments. The published open-source methods provide a flexible framework for the implementation of additional models and can be used to analyze future experiments, enabling the generation of higher statistical significance.

Chapter 1

Introduction

Sometimes, particles act in ways that do not match what we are used to in everyday life. Take, for example, the sudden brilliance of a lightning strike, a powerful equalization of electrostatic charges across the sky. Or the energy released in combustion, where matter transforms in a blaze of heat and light. These processes hint at a hidden world of physics, one where energy and matter interact in extraordinary ways. But beyond Earth, this unusual behavior is not the exception, it is the norm.

The vast expanse of space is almost entirely filled with a form of matter that is rarely encountered on Earth, yet it is responsible for some of the most breathtaking natural phenomena, such as the auroras dancing across our polar skies [1]. This is plasma, the fourth state of matter. Unlike solids, liquids, and gases, plasma consists of particles that have been ionized, meaning they possess so much energy that electrons are stripped from their atoms, creating a dynamic and electrically charged environment.

Unlike a typical gas, plasma conducts electricity with ease, flowing along invisible paths shaped by electromagnetic fields [2]. It permeates the cosmos, making up more than 99% of the visible universe, from the fiery heart of our Sun to the distant stars and the vast interstellar medium [3]. Understanding plasma is essential for addressing some of the biggest questions in astrophysics, including how stars form, the role plasma plays in protoplanetary disks, and how it shapes the evolution of galaxies [4, 5].

Yet plasma is not just a cosmic curiosity, it holds the key to one of the most urgent scientific challenges on Earth, the quest for sustainable energy. In fusion reactors, superhot plasma might one day give us almost unlimited energy, but to control it, we need a deep understanding of how it behaves [6]. Plasma also plays a crucial role in advanced technology, for example, it is generated by high-energy lasers during semiconductor manufacturing processes [7].

By exploring plasma in its many forms, both in space and in the laboratory, we take a step closer to unlocking the mysteries of the cosmos and shaping the future of energy and technology on our planet.

1.1 Complex Plasma

The term plasma was first introduced in the 1920s by Irving Langmuir and Lewi Tonks, who used it to describe the glowing, ionized gas produced by an electric discharge inside a tube [8]. At the time, they could hardly have imagined that this strange state of matter, often referred to as the fourth state, would turn out to be the most common form of matter in the universe [9].

As experimental research into plasma physics progressed, scientists began to notice unexpected instabilities and structural formations within laboratory plasmas. These disturbances were eventually attributed to the presence of microscopic dust particles, often introduced through sputtering of the tungsten cathode [10]. What was first seen as a problem in the experiment soon became an exciting area of research in the study of dusty or complex plasmas.

At the same time, space scientists were turning their attention to similar effects in astrophysical environments. The presence of dust-plasma interactions became evident in the brilliant tails of comets, where charged dust grains interact with the streaming solar wind [11]. The same principles were invoked to explain the luminous glow of the interstellar medium, particularly in regions like the Orion Nebula, which remains visible even to the naked eye [12]. In the 1980s, NASA's Voyager probes made another groundbreaking discovery, the mysterious radial "spokes" in Saturn's B ring, features that are now thought to result from plasma-dust interactions within the planet's complex magnetospheric environment [13].

A complex plasma (or dusty plasma) is loosely defined as an electron-ion plasma that contains an additional component of micron- or submicron-sized charged particles. These dust grains acquire charge primarily through the collection of ambient plasma electrons and ions, though other charging mechanisms can also contribute. In typical laboratory discharge experiments, dust particles tend to charge negatively, as electrons, being much lighter than ions, reach them more frequently [9].

This charge accumulation transforms dusty plasmas into highly interactive, multi-particle Coulomb systems [3]. Unlike neutral gases, where collisions dominate interactions, dusty plasmas exhibit collective behavior governed by electrostatic forces. These interactions lead to various fascinating effects, including self-organized structures, crystalline-like arrangements, and dynamic waves that provide an experimental playground for studying fundamental physics [10].

Far from being an anomaly, dusty plasmas are now recognized as a key component of many astrophysical and space environments. Understanding their behavior is crucial for shedding light on the mysteries of planetary rings, cometary tails, interstellar clouds, and even the formation of planets themselves [11]. Whether in controlled laboratory conditions or in the vastness of space, the study of complex plasmas continues to push the boundaries of our knowledge, revealing how matter and fields interact in ways that challenge and deepen our understanding of the universe [14].

1.1.1 Charge and Charge Distribution

Dusty plasmas are complex systems where the dynamics are heavily influenced by the charge on the dust particles [9]. A comprehensive understanding of the dust charging mechanisms is therefore essential for interpreting and modeling such systems. Similar to the principles underlying electrostatic probe diagnostics, where measured current-voltage characteristics provide insights into key plasma parameters such as electron and ion densities and temperatures, the charging of dust particles is likewise dependent on the local plasma environment [15].
Theoretically, accurate knowledge of the plasma parameters, including electron temperature and plasma density, enables a precise estimation of the dust grain charge. Charging arises primarily through the collection of electrons and ions from the surrounding plasma. Due to their significantly lower mass, electrons reach the dust surface more readily and are typically collected first, resulting in a net negative charge on the dust particle. This negative potential subsequently attracts the more massive ions, which accumulate near the dust grain and form a shielding cloud, thereby contributing to the overall quasi-neutrality of the plasma.

Debye Length and Shielding Effects

The boundary of this shielding cloud is determined by the radial distance at which the potential energy of the charged species is approximately equal to their thermal energy, given by $k_B T_s$. Assuming local thermodynamic equilibrium for the electron and ion species, their respective number densities, n_e and n_i, follow a Boltzmann distribution, which can be linearized as [9]:

$$n_{e,i} = n_{0e,0i} \exp\left(\pm \frac{e\phi_s}{k_B T_{e,i}}\right) \approx n_{0e,0i}\left(1 \pm \frac{e\phi_s}{k_B T_{e,i}}\right), \tag{1.1}$$

where n_{0s} represents the number density of the respective species at a sufficient distance from the shielding cloud, where plasma quasi-neutrality is maintained.
To describe the space charge potential ϕ_s, Poisson's equation provides a fundamental relation between the electrostatic potential and charge density:

$$\nabla^2 \phi_s = \nabla \cdot E = \frac{\rho}{\varepsilon_0} = \frac{e}{\varepsilon_0}(n_{0e} - n_{0i}). \tag{1.2}$$

Substituting the linearized density expressions, the equation simplifies to:

$$\nabla^2 \phi_s = \frac{e^2}{\varepsilon_0}\left(\frac{n_{0e}}{k_B T_e} + \frac{n_{0i}}{k_B T_i}\right)\phi_s. \tag{1.3}$$

From this, the inverse square of the Debye length is given by:

$$\lambda_D^{-2} = \frac{e^2}{\varepsilon_0}\left(\frac{n_{0e}}{k_B T_e} + \frac{n_{0i}}{k_B T_i}\right), \tag{1.4}$$

where the electron and ion Debye lengths are defined as:

$$\lambda_{De,i} = \left(\frac{k_B T_{e,i} \varepsilon_0}{4\pi n_{0e,i} e^2} \right)^{1/2}. \tag{1.5}$$

The effective shielding length, corresponding to the thickness of the sheath surrounding a resting particle, is given by the combined Debye length:

$$\lambda_D = \frac{\lambda_{De}\lambda_{Di}}{(\lambda_{De}^2 + \lambda_{Di}^2)^{1/2}}. \tag{1.6}$$

This characteristic length defines the scale of electrostatic screening in a plasma and determines how quickly the electrostatic potential around a charged object fades with distance. The screening effect becomes increasingly prominent when the dust particles are significantly smaller than the Debye length. In such regimes, the plasma's capacity to shield electrostatic charges extends over a spatial range much larger than the physical dimensions of the dust particles. This disparity introduces additional complexity to the interparticle interactions and the collective behavior of the system, thereby influencing the overall dynamics of the dusty plasma [15].

Orbital Motion Limited Charge Approximation

The Orbital Motion Limited (OML) theory provides a foundational framework for describing the collection of electrons and ions by a dust particle in a plasma. It is based on the conservation of energy and angular momentum, and enables analytical estimation of the dust grain charge by considering the effective cross-section for plasma particle collection [15]. The applicability of the OML model rests on the following idealized assumptions:

(i) The dust grain is electrically isolated, such that interactions with neighboring dust grains do not perturb the trajectories of incoming electrons or ions.

(ii) Electrons and ions travel collisionlessly through the plasma, i.e., their mean free path exceeds the Debye length, and they do not experience collisions prior to reaching the dust surface.

(iii) The effective potential U_{eff} experienced by charged particles does not exhibit a repulsive barrier. For grains where the particle radius a satisfies $a < \lambda_D < \rho_c$, with ρ_c denoting the critical impact parameter, below particles are not reflected before reaching the grain surface.

Under these conditions, the dust potential and corresponding heat collection can be determined from the following key relations:

$$L = m_i v_{i0} \rho_c = m_i v_i a, \tag{1.7}$$

$$\frac{1}{2} m_i v_{i0}^2 = \frac{1}{2} m_i v_i^2 + \frac{e Q_d}{4\pi\varepsilon_0 a}, \tag{1.8}$$

where m_i is the ion mass and v_{i0} is the ion velocity far from the dust grain. Ions with $\rho < \rho_c$ are collected by the grain and reach its surface with velocity v_i, as depicted in Figure 1.1.
The charge of the dust particle Q_d, is given by $Q_d = C \cdot \Phi_{fl}$, where C is the capacitance of the grain. For a conducting spherical grain in the limit $a \ll \lambda_D$, the capacitance is approximated by:

$$C = 4\pi\varepsilon_0 a \exp(-a/\lambda_D) \approx 4\pi\varepsilon_0 a. \tag{1.9}$$

Using these relations, the effective cross-section for electron and ion collection can be expressed as:

$$\sigma_{ce,ci} = \pi\rho_c^2 = \pi a^2 \left(1 \pm \frac{2e\Phi_{fl}}{m_{e,i} v_{e0,i0}^2}\right). \tag{1.10}$$

This formulation accounts for the influence of the electrostatic potential of the dust particle on the collection cross-section, where the sign convention reflects the attraction or repulsion of charged species based on the dust potential. The charging currents $I_{e,i}$ on the dust grain can be obtained by integrating over the Maxwell-Boltzmann distribution function $f_{e,i}(v)$:

$$I_{e,i} = n_{e,i} \int v\sigma_{ce,ci} f_{e,i}(v)\, d^3v. \tag{1.11}$$

This results in the following expressions for the ion and electron currents:

$$I_i = \pi a^2 n_i e \sqrt{\frac{8k_B T_i}{\pi m_i}} \left(1 - \frac{e\Phi_{fl}}{k_B T_i}\right), \tag{1.12}$$

$$I_e = -\pi a^2 n_e e \sqrt{\frac{8k_B T_e}{\pi m_e}} \left(\frac{e\Phi_{fl}}{k_B T_e}\right). \tag{1.13}$$

If the electron and ion currents balance each other, $I_e = I_i$, the equilibrium dust charge potential can be determined. Assuming negatively charged dust grains and ion velocities significantly lower than their thermal velocities, the maximum charge on the grain can be estimated by incorporating Equation [1.9]. This yields:

$$Q_d = C_0 \frac{4\pi\varepsilon_0 a k_B T_e}{e} \ln\left[\frac{n_i}{n_e}\left(\frac{m_e T_e}{m_i T_i}\right)^{1/2}\right], \tag{1.14}$$

where $C_0 \sim 0.73$ is a correction factor that accounts for deviations from idealized conditions and depends on plasma parameters [16]. While OML theory is widely applied for estimating dust charging, its validity is strongly constrained, providing only an upper bound for the grain charge under the given assumptions. In the context of this study, the predictive accuracy of OML theory is insufficient, necessitating further refinement by incorporating ion-neutral collisions.

Trapped Ions

The effects of electron and ion collisions on the dust charging process and electrostatic shielding are often considered negligible. However, under certain conditions, a significant population of trapped ions can accumulate around a dust particle due to charge exchange collisions with the neutral gas background. Ions that undergo collisions with neutrals while in the vicinity of a grain may experience a substantial loss of kinetic energy, preventing their escape from the potential well generated by the microparticle. Consequently, the positive ion current to the grain can increase significantly, altering the shielding properties of the dust grain.
Additionally, under specific plasma conditions, some ions may enter stable orbital motion around the grain. These ions remain confined within the electrostatic potential without directly impacting the grain surface or escaping into the bulk plasma. Their presence modifies the local potential distribution around the microparticle, leading to a reduction in the absolute magnitude of the negative floating potential Φ_{fl}. The combined effects of ion collisionality and trapped ions can reduce the negative floating potential of microparticles by up to 50%, depending on the plasma parameters [17].

Dense Particel Cloud

As the density of dust particles in the plasma increases, the total charge carried by the microparticles can constitute a significant fraction of the overall charge carried by ions and electrons. In this regime, the condition of quasi-neutrality remains valid but must be modified to explicitly account for the presence of dust particles:

$$n_i = n_e + Z_d n_d, \tag{1.15}$$

where $Z_d = |Q_d/e|$ denotes the charge number of a microparticle, and n_d represents the dust particle density. However, when the dust density becomes sufficiently high, charge collection by the dust grains can lead to a significant depletion of the electron density. Incorporating this effect and combining Equations 1.12, 1.13, and 1.15 yields the following relation [15]:

$$\sqrt{\frac{T_i}{T_e}}\exp(-z) = \sqrt{\frac{m_e}{m_i}}(1 + z\frac{T_i}{T_e})(1 + P_H), \tag{1.16}$$

where the Havnes parameter is introduced as

$$P_H = \frac{Z_d n_d}{n_i}, \tag{1.17}$$

quantifying the relative contribution of dust grains to the charge balance. The dimensionless microparticle charge potential, z, is then related to the charge number through the expression [15]:

$$z = \frac{Z_d e^2}{4\pi\varepsilon_0 a k_B T_e} \tag{1.18}$$

1.1.2 Forces Acting on Dust Particles

The characterization of particle charge enables a detailed examination of the interactions between the plasma and the microparticle. In this study, we focus on the fundamental forces governing a cold, unmagnetized laboratory plasma. The forces acting on microparticles immersed in the plasma environment are systematically categorized based on their relative magnitudes of influence. Figure 1.1 presents a schematic representation of a microparticle with radius a subjected to an external electric field E. The figure highlights the primary forces governing the particle's dynamics, along with the key parameters essential for their characterization. A detailed discussion of each force and its implications will be provided in the subsequent subsections.

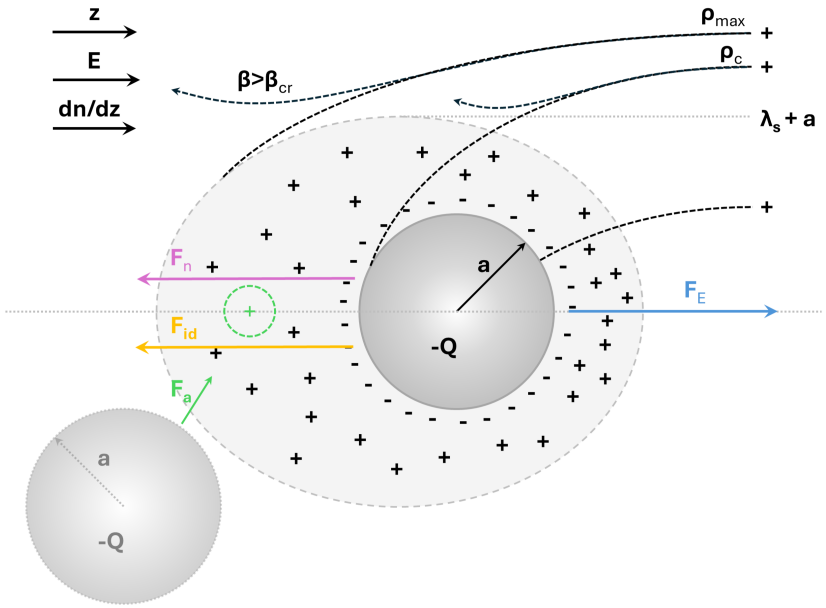

Figure 1.1: The figure illustrates the charge distribution around a microparticle of radius a, drifting along the electric field E under the influence of the force F_E. The dynamics of the particle are governed by two counteracting forces: the neutral drag force F_n and the ion drag force F_{id}. The microparticle is shielded by electrons $(-)$ and ions $(+)$, maintaining quasi-neutrality within a characteristic shielding length of $\lambda_s + a$. This shielding results in a perturbed charge potential z, which is influenced by the background plasma flow. A nearby secondary particle within interaction radius of the primary microparticle experiences an attractive force F_a, induced by an increased positive space charge (green dashed area) in its wake. An incoming ion is affected by the charge potential as it approaches the microparticle. If it enters within the Coulomb radius ρ_c, it is captured. Beyond this region, it is scattered, and at distances exceeding $\rho_{\max}$, the ion interacts in the far field, with its trajectory determined by the scattering parameter β.

Gravitational Force

In ground-based experiments, the most prominent force acting on the microparticle is gravity, given by

$$F_g = m_d \cdot g = \frac{4}{3}\rho_d a^3 g, \tag{1.19}$$

where m_d is the mass of the particle, ρ_d is the dust density, and g is the gravitational acceleration. The gravitational force scales with the particle volume, $F_g \propto a^3$, and has a dominant influence on larger microparticles with radii $a \gtrsim 3\,\mu m$. In contrast, for smaller particles, the electric force becomes the dominant factor, while gravity ranks third in influence after the thermophoretic force [18].

Electrostatic Force

Under typical complex plasma conditions, the radius of the microparticle is significantly smaller than the Debye length, $a \ll \lambda_D$. Consequently, the electric field force can be described as

$$F_E = Z_d \cdot e \cdot E, \tag{1.20}$$

where Z_d is the charge number of the particle, e is the elementary charge, and E is the external electric field. This force exhibits a linear dependence on the particle radius, $F_E \propto a$, and serves as the dominant force for small microparticles, effectively counteracting gravity for particle sizes $a \lesssim 3\,\mu m$. The microparticle is assumed to be isolated within a low-pressure discharge plasma, experiencing an effective potential without significant distortion [19].

Thermophoretic Force

Temperature gradients present a significant challenge in experimental conditions but can also be actively utilized to control microparticles through the thermophoretic force. This force arises due to the asymmetry in momentum transfer, where atoms at higher temperatures carry more momentum than those at lower temperatures. As a result, the microparticle experiences a net force directed toward the region of lower gas temperature, described by:

$$F_{th} = -3.33 \cdot \left(\frac{k_B a^2}{\sigma}\right) \Delta T, \tag{1.21}$$

where ΔT denotes the temperature gradient, and σ represents the effective cross-section of the plasma gas. The thermophoretic force scales as $F_{th} \propto a^2$ and plays a crucial role in influencing both large and small microparticles. Under certain conditions, it can even lead to the levitation of microparticles in the presence of gravitational forces [20].

Neutral Drag Force

A particle moving through a plasma experiences a friction force due to interactions with surrounding neutral atoms or molecules, with these interactions limited to elastic scattering. Epstein [21] formulated a method to determine the drag force acting on a sphere moving in a plasma, under the assumption that the particle radius is small compared to the mean free path of the neutral atoms. Additionally, the velocity of the sphere must be small in comparison to the thermal velocity of the neutral atoms. The drag force is given by:

$$F_n = -\gamma_{Ep} m_d v_d, \tag{1.22}$$

where the damping rate coefficient is defined as:

$$\gamma_{Ep} = \left(\frac{4\pi\delta_{Ep}}{3}\right)\left(\frac{n_n m_n v_{th,n}}{m_d}\right) a^2. \tag{1.23}$$

Here, n_n denotes the number density, m_n the mass and $v_{th,n}$ represents the thermal velocity of the neutral gas atoms. The interaction coefficient δ_{Ep} is taken to be 1.44 throughout this work [21, 22]. The neutral drag force scales quadratically with the particle radius, $F_n \propto a^2$.

Ion Drag Force

The ion drag force plays a crucial role in laboratory plasmas and is a major focus of this thesis. This force arises due to momentum transfer from streaming ions to charged microparticles, significantly influencing the dynamics of complex plasma systems subjected to electric fields. Given the negative charge of the microparticles and the positive charge of the ions, their interaction occurs via either elastic scattering or ion capture.
An early theoretical model proposed by Barnes [23] postulated that the ion drag force can be decomposed into three distinct components. These include the collection drag force, F_{dir}, which results from the direct impact of ions onto the particle surface and is also responsible for particle charging, the Coulomb drag force, F_{Coul}, which arises due to Coulomb interactions between ions and microparticles, and the ion flow force, which is associated with the distortion of the Debye sphere surrounding the particle. However, the ion flow force is typically assumed to be negligibly small, leading to the common approximation of the ion drag force as:

$$F_{id} = F_{dir} + F_{Coul}. \tag{1.24}$$

The collection force is derived using Orbital Motion Limited theory and is expressed as:

$$F_{dir} = \pi a^2 m_i n_i u_i v_s \left(1 - \frac{2e\Phi_{fl}}{m_i v_s^2}\right), \tag{1.25}$$

where $v_s = (u_i^2 + v_{th,i}^2)^{1/2}$ represents the mean ion velocity, with u_i being the ion drift velocity and $v_{th,i}$ the ion thermal velocity.
The elastic Coulomb drag force is given by:

$$F_{Coul} = 4\pi\rho_{\pi/2}^2 m_i n_i u_i v_s \Gamma_C, \tag{1.26}$$

where $\rho_{\pi/2}$, the impact parameter for 90° deflection, is defined as:

$$\rho_{\pi/2} = \frac{ae\Phi_{fl}}{m_i v_s^2}. \tag{1.27}$$

The Coulomb cross-section, Γ_C, accounts for the effect of ions deflected by the dust grain potential denoted as the Coulomb logarithm. The collision parameter, ρ_c, sets the minimum boundary, see Figure 1.1, while the maximum boundary for the Coulomb collision cross-section is set by the Debye length λ_D, giving:

$$\Gamma_C = \frac{1}{2}\ln\left(\frac{\lambda_D^2 + \rho_{\pi/2}^2}{\rho_c^2 + \rho_{\pi/2}^2}\right), \tag{1.28}$$

Hutchinson and Khrapak proposed a modified Coulomb logarithm that accounts for collisions outside the Debye sphere and incorporates a velocity-dependent screening length, λ_s, to improve the ion drag model. The modified Coulomb logarithm is given by:

$$\ln\Lambda = \ln\frac{\rho_{\pi/2} + \lambda_s}{\rho_{\pi/2} + a}, \tag{1.29}$$

with

$$\lambda_s^2 = \frac{\lambda_{De}^2}{1 + 2k_B T_e/(m_i v_s^2)} + a. \tag{1.30}$$

Continuous numerical calculations by Hutchinson have shown that an effective ion velocity should be used to correctly evaluate the Coulomb logarithm. The impact parameter is modified as $\rho_{\pi/2} = ae\Phi_{fl}/(m_i v_{eff}^2)$, where the effective velocity is given by:

$$u_{eff}^2 = \frac{2k_B T_i}{\pi m_i} + u_i^2\left[1 + \left(\frac{|u_i|/u_B}{0.6 + 0.05\ln(\mu) + (\lambda_{D,e}/5a)(\sqrt{T_i/T_e} - 0.1)}\right)^3\right]. \tag{1.31}$$

Here, μ is the atomic mass number of the ion, and $u_B = \sqrt{k_B T_e/m_i}$ is the Bohm velocity. The qualitative description of the ion drag force has evolved significantly, but Khrapak et al. demonstrated in the early 2000s that the described force underestimates reality. This discrepancy is due to the formation of a phenomenon called a void—a particle-free region in the center of a dense particle cloud—driven by the ion drag force. To address this, the standard Coulomb logarithm was modified to include small-angle ion-grain coupling:

$$\Lambda_C = 2\int_0^\infty e^{-x}\ln\left(\frac{2\lambda_D x + \rho_{\pi/2}}{2ax + \rho_{\pi/2}}\right)dx. \tag{1.32}$$

The complexity of ion drag arises from the challenge of accurately describing the interaction potential and cross-section between microparticles and ions, as well as distinguishing between various interaction mechanisms. Khrapak et al. conducted a detailed analytical investigation of these interactions, classifying them based on the ion kinetic speed and shielding potential using the ion thermal scattering parameter [24]:

$$\beta_T = \frac{\rho_{\pi/2}}{\lambda_D}. \tag{1.33}$$

This parameter enables the definition of interaction regimes and facilitates the selection of the most appropriate interaction cross-section for a given physical scenario. The relevant parameter space is closely linked to the conditions of the PK-4 experiment. The thermal scattering parameter serves as a fundamental criterion for determining whether a complex plasma system operates in a weakly coupled, intermediate, or strongly coupled regime, by quantifying the relative influence of thermal motion and electrostatic interactions [25]. Figure 1.1 presents a visualization of the interaction types categorized by scattering parameters.

For weak interactions, where $\beta_T \ll 1$, the complex plasma system behaves similarly to an ideal gas, with short-range Coulomb interactions dominating and exhibiting minimal collective effects. In this regime, interactions remain largely uncorrelated, and ion drag follows conventional Coulomb collision models. As the system transitions into the intermediate regime, $\beta_T \approx 1$, the plasma exhibits liquid-like behavior, characterized by moderate energy transfer and increased correlation between microparticles and ions. In this regime, both Coulomb scattering and ion capture contribute significantly to the dynamics. The analytic model describing weak and intermediate regimes, denoted as $F_{id}^{weak,int}$, employs a modified Coulomb logarithm to effectively characterize ion-particle interactions under these conditions. This model remains valid for scattering parameters up to approximately $\beta_T \approx 5$, capturing the primary features of ion drag within this range [26].

In contrast, for strong interactions, the analytic approach becomes less effective due to significant energy transfer and complex interaction dynamics. The model for this regime, denoted as F_{id}^{strong}, simplifies the system by disregarding the effects of distant collisions beyond the maximum interaction radius ρ_{max}, while assuming a logarithmic decrement below this threshold. Numerical evaluations based on a shielded Yukawa potential suggest a critical scattering parameter of $\beta_{crit} \approx 13$, which defines the onset of strong interaction dynamics [26].

Additionally, a hybrid model, F_{id}^{hybrid}, integrates hydrodynamic and kinetic theories and is supported by particle-in-cell and Monte Carlo simulations [27]. This framework, based on the kinetic approach proposed by Hutchinson and Khrapak [28], accounts for the full spectrum of interaction regimes, providing a comprehensive description of plasma dynamics across all coupling strengths.

The models describing weak and intermediate regimes, as well as the hybrid approach, constitute the primary focus of this thesis. A more detailed analysis of ion drag effects on particle dynamics and the validation of the proposed models is presented in the submitted preprint in Chapter 4.

1.1.3 Complex Plasma Waves

Plasmas, composed of various charged species, inherently exhibit instabilities due to the collective motion of these particles. A prominent class of instabilities arises from the formation of extended spatial regions of charge separation, often manifesting as wave-like structures. These instabilities can be driven, for example, by counter-streaming ions and electrons. Similar effects are observed when microparticles are introduced into the plasma, although the response dynamics differ due to the significant mass disparity between plasma species and the embedded particles [9].
The response frequency of electrons is high due to their small mass and is described by the plasma frequency:

$$\omega_{pe}^2 = \frac{n_e e^2}{m_e \varepsilon_0}. \tag{1.34}$$

Electrons, with mass m_e, in a typical plasma discharge can respond to electric field perturbations at frequencies reaching several GHz. In contrast, ions, having much larger masses, respond on a significantly slower timescale, with an angular plasma frequency given by:

$$\omega_{pi}^2 = \frac{n_i e^2}{m_i \varepsilon_0}, \tag{1.35}$$

Typical ion plasma frequencies range in the MHz regime.
The heaviest charged species in complex plasmas are dust particles, which exhibit the slowest response due to their significantly larger mass. The characteristic dust plasma frequency is:

$$\omega_{pd}^2 = \frac{n_d Z_d^2 e^2}{m_d \varepsilon_0}, \tag{1.36}$$

typically on the order of a few kHz [9]. The disparity in response frequencies among plasma species gives rise to distinct low-frequency wave modes in complex plasmas. Among these, the most prominent is the dust acoustic wave (DAW), first theoretically predicted by Rao et al. [29]. DAWs manifest as longitudinal waves within the microparticle fluid and can be spontaneously excited by local instabilities, such as ion-microparticle streaming instabilities.
The excitation and propagation of DAWs are strongly influenced by experimental conditions. In particular, a sufficiently low gas pressure is essential to minimize collisional damping, allowing sustained wave propagation. Additionally, a sufficiently high microparticle density and an electric field strong enough to accelerate ions are crucial for the onset of the instability [30].
To describe this phenomenon, the dispersion relation is derived by analyzing the linear response of the plasma to small perturbations. These perturbations are assumed to take the form $\exp(ikx - i\omega t)$, representing plane waves propagating in the x-direction, where k is the wave vector and ω the angular frequency [9]. Assuming that electrons and ions follow Boltzmann distributions (1.1) and that the electrostatic potential is governed by the

total charge density according to Poisson's equation, the response of the plasma species electrons,$\tilde{n}_e$, and ions,$\tilde{n}_i$, to an electric field perturbation, $\tilde{\phi}$, can be expressed in terms of density fluctuations as:

$$\tilde{n}_e = \frac{n_e e\tilde{\phi}}{k_B T_e}, \quad \tilde{n}_i = -\frac{n_i e\tilde{\phi}}{k_B T_i}. \tag{1.37}$$

In the case of the DAW, the dominant restoring force arises from the pressure of the ion cloud, while the inertia is primarily provided by the dust mass. To derive the wave properties, a perturbative approach is applied, utilizing the linearized continuity and momentum equations for the dust component. The continuity equation describes variations in dust density due to its motion, while the momentum equation governs the dust velocity response to the electrostatic potential. Together, these equations establish a link between dust density fluctuations, $\tilde{n}_d$, and assuming a plane wave perturbation, yielding [9]:

$$\tilde{n}_d = -\frac{n_d k^2 Z_d e\tilde{\phi}}{m_d \omega^2}. \tag{1.38}$$

Substituting these density perturbations into Poisson's equation (1.2) leads to:

$$k^2\tilde{\phi} = -\frac{e}{\varepsilon_0}\left(\tilde{n}_i - \tilde{n}_e - Z_d\tilde{n}_d\right). \tag{1.39}$$

Using the expressions for $\tilde{n}_e$, $\tilde{n}_i$, and $\tilde{n}_d$ into Poisson's equation, we obtain:

$$k^2\tilde{\phi} = -\frac{e}{\varepsilon_0}\left(-\frac{n_i e\tilde{\phi}}{k_B T_i} - \frac{n_e e\tilde{\phi}}{k_B T_e} + Z_d\frac{n_d k^2 Z_d e\tilde{\phi}}{m_d\omega^2}\right). \tag{1.40}$$

Applying the quasi-neutrality condition and assuming cold ions ($T_i \ll T_e$), the wave frequency simplifies to:

$$\omega = k\sqrt{\frac{k_B T_i}{m_d}\frac{n_d}{n_i}Z_d^2}, \tag{1.41}$$

which describes the fundamental behavior of DAWs, with the corresponding acoustic wave speed, $C_{DAW} = \omega/k$.
In Chapter 2, DAWs are a primary focus. Experimental investigations have been conducted and successfully reproduced, revealing DAWs exhibiting an atypical wave distortion.

1.1.4 Electrorheology

Electrorheological (ER) fluids are suspensions of dielectric particles in a carrier liquid that undergo rapid and reversible changes in viscosity upon exposure to an external electric field. When subjected to an electric field, the suspended particles become polarized and align into chain-like structures along the field direction, thereby increasing the fluid's resistance to flow. This tunable viscosity renders ER fluids advantageous for various applications,

including adaptive dampers, clutches, and robotic actuators. Upon removal of the electric field, the fluid promptly returns to its original low-viscosity state [31].

In complex plasmas, the effective radius of the polarizable cloud surrounding a microparticle is typically governed by the ion screening length. In the absence of an external electric field, this polarizable cloud maintains a symmetrical, spherical shape. However, when an external electric field is applied, the symmetry is disrupted, leading to the formation of an asymmetric charge distribution, as illustrated in Figure 1.1. The center of this asymmetric region, known as the ion wake, is displaced downstream relative to the microparticle due to the field-induced ion drift. This localized positive space charge region generates an attractive force, F_a, on neighboring microparticles, causing them to align within the wake and subsequently form their own wake structures. This self-reinforcing process is the underlying mechanism responsible for the formation of linear particle chains or strings [32]. The strength and nature of this effect depend not only on the applied electric field but also on the velocity of the ion drift.

In the context of ion streaming effects, the interaction is well approximated by a dipole potential. However, when the polarity of the electric field alternates at a frequency such that the microparticles experience a net force while the ions respond dynamically to the oscillations, the system transitions to a regime where quadrupole interactions dominate [32].

The unperturbed repulsive potential surrounding a microparticle is described by the Yukawa potential, $\Phi_Y(r)$, where r represents the radial distance from an incoming ion or test charge. The modification of this potential due to the attractive dipole contribution, $\Phi_D(r, \Theta)$, and the quadrupole effect, $\Phi_Q(r, \Theta)$, depends on the angular alignment of the ion current. The modified potential is then given by [32]:

$$\Phi(r, \Theta) \simeq Q \left[\frac{\exp(-r/\lambda_D)}{r} - 2\sqrt{\frac{2}{\pi}} \frac{M^2 \lambda_D^2}{r^3} \cos\Theta - \left(2 - \frac{\pi}{2}\right) \frac{M^2 \lambda_D^2}{r^3} (3\cos^2\Theta - 1) \right] \quad (1.42)$$

This interaction leads to measurable side effects and plays a fundamental role in the formation of string-like structures. In this context, strings are defined as electrorheologically connected microparticles that self-organize into chain-like configurations. These structures are identified by analyzing the angular correlations between neighboring particles at a fixed interparticle distance, which serves as a quantitative measure of string formation [33]. Empirical evidence suggests that the probability of string formation among microparticles increases under the influence of electrorheological effects [34].

The role of electrorheology is a central focus of Chapter 3, where the impact of the plasma environment on the microparticle potential is systematically examined. Additionally, the influence of electrorheological effects on DAW propagation is explored, providing experimental validation of the theoretically predicted effects through numerical simulations [35].

1.2 Plasma Kristall Experiment

The history was launched by the idea of conducting complex plasma experiments under microgravity conditions emerged approximately 35 years ago as a solution to mitigate the gravitational influence on dust particles, which posed a significant challenge in laboratory studies on Earth [36]. This marked a pivotal milestone in the field of complex plasma research. The first experiments were carried out in microgravity environments using parabolic flights, rocket launches, and eventually onboard the MIR space station in the late 1990s [37]. These efforts were primarily driven by the Max Planck Institute for Extraterrestrial Physics (MPE) in Garching, Germany, in collaboration with the Institute for High Energy Density (IHED) in Moscow, Russia. This partnership led to the establishment of the Plasma Kristall Experiment (PKE) program [36].
At the beginning of the 21th century, the first experimental apparatus under this program, PKE-Nefedov, was installed aboard the International Space Station (ISS). This experiment utilized a radio-frequency (rf) capacitive discharge chamber in which micrometer-sized silica particles were introduced into a plasma environment [38]. It enabled the observation and investigation of various fundamental plasma phenomena, including Coulomb crystals, dust particle growth, and phase transitions in complex plasmas. Following the success of PKE-Nefedov, an improved version of the experiment, PK-3+, was also deployed on the ISS, enabling further advancements in the study of complex plasmas [15].
Building upon these foundational studies, PK-4 was developed as a next-generation experimental facility and was installed in the European Columbus module of the ISS in 2014 [37]. Unlike its predecessors, PK-4 utilizes a direct current (DC) discharge in a tube geometry, allowing for the study of liquid-phase and flow phenomena in complex plasmas under microgravity conditions [37]. This experimental setup provides significant advantages for investigating various dynamical processes, including sheared laminar flow of a highly non-ideal dusty liquid and its transition to turbulence, nozzle flow, boundary layers, instabilities, shock wave (soliton) formation and propagation, particle lane formation, and size-dependent separation of dust grains [15].
Despite the considerable progress achieved through these experiments, complex plasma research remains a field of significant scientific and technological interest. A new project, COMPACT, is currently under development. This experiment features a fully adjustable RF discharge setup combined with a 3D camera system, and investigations are already underway during parabolic flight campaigns, aiming to further push the boundaries of complex plasma research [39].

1.2.1 PK-4

The PK-4 experimental setup, in detail described by Pustylnik et. al [40], consists of a cylindrical, π-shaped plasma chamber with a diameter of 3 cm and a total tube length of 86 cm. The primary working area spans 20 cm in length. Electrodes positioned at the ends of the side tubes facilitate a direct current (DC) discharge, operating current controlled within a range of -3.1 mA to 3.1 mA, with a maximum applied voltage of up to 2.7 kV in

either neon or argon gas. A schematic illustration of the setup is provided in Figure 1.2.

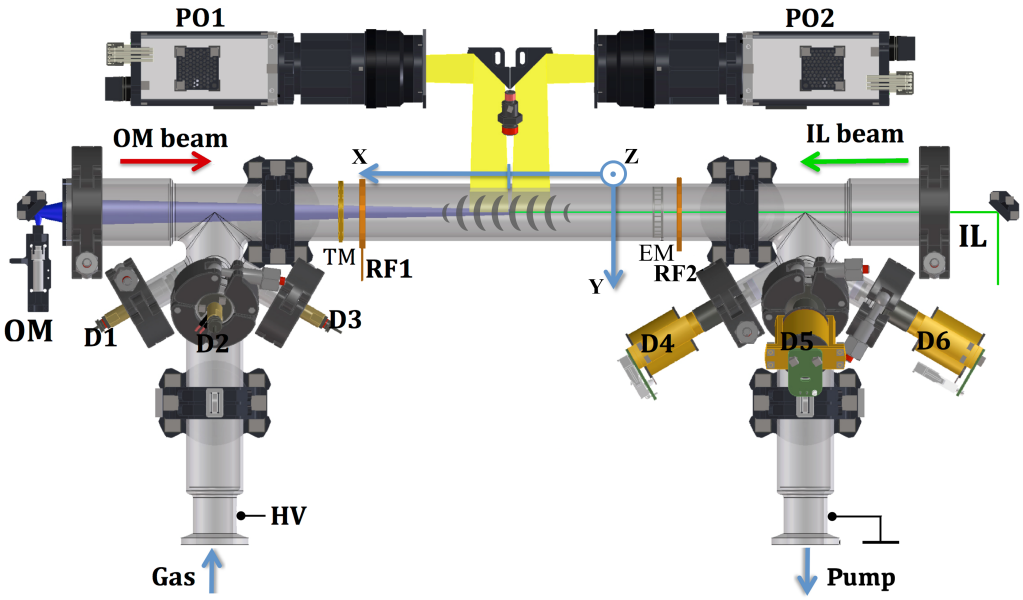

Figure 1.2: A schematic representation of the experimental setup Pk-4 is shown with an equal build used during laboratory experiments, parabolic flight and campaigns aboard the international space station (Image adapted from [41]). Key components and manipulation mechanisms are labeled, including the illumination laser (IL) and optical manipulation laser (OM). The setup further incorporates radio-frequency (RF) coils, electromagnetic (EM) manipulator, and thermal manipulator (TM). Microparticle injections are facilitated through dispensers D1–D6, while particle dynamics were recorded using particle observation cameras (PO).

The high-voltage (HV) power supply operates in two distinct modes: as a pulse generator and as an arbitrary waveform generator. The characteristics of the output signal are primarily determined by the total period T_3, as illustrated in Figure 1.3. Polarity reversal within the signal is controlled by a dedicated timing parameter T_2, which can be fully adjusted to suit experimental requirements.
The gas inlet and current control are situated on the active electrode side, whereas gas control and current measurements are performed on the passive electrode side. As a low-pressure plasma experiment, PK-4 requires a well-maintained vacuum environment within the experimental volume. The pressure can be regulated between a minimum of < 10 Pa and a maximum of 250 Pa, with a controlled gas flow rate adjustable between 0 and 10 sccm (standard cubic centimeter per minute).
PK-4 is equipped with six dispensers containing microparticles. The microparticles are composed of melamine-formaldehyde (MF), with diameters ranging from $2a = 1.3\mu$m to 10.6μm. Particle injection into the plasma is facilitated by an electromagnetic *shaker* mech-

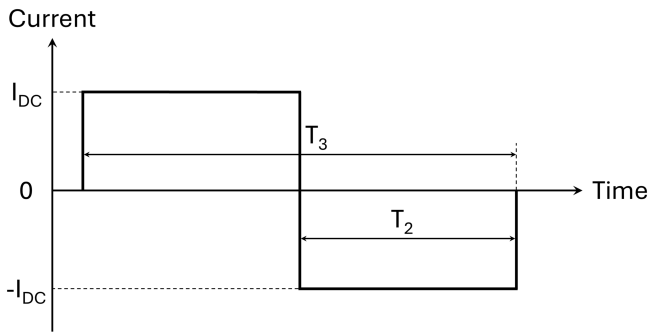

Figure 1.3: Schematic representation of the high-voltage pulse generator signal. In the context of this work, the signal is characterized by the total period T_3, which defines the overall duration of the waveform, and the polarity switching time T_2, which governs the timing of voltage polarity reversal.

anism, which agitates the container to release microparticles through a gridded bottom. This mechanism is controlled via three parameters: the duration of the applied current to the coil (T_{on}), the relaxation time (T_{off}), and the number of shaking repetitions (N_{shakes}). The plasma chamber's working area is illuminated using a diode laser sheet with 532 nm wavelength, and microparticle motion is observed via two particle observation (PO) cameras. These cameras are adjustable both along (x-axis) and perpendicular to the plasma chamber (y-axis). Since the cameras operate at a fixed focal plane and the laser sheet selectively illuminates particles at a given distance, this adjustability enables tomographic imaging techniques.
The specifications of the observation cameras differ depending on whether the experiments are conducted aboard the International Space Station (ISS) or in the ground-based laboratory setup. The ISS configuration utilizes two CCD particle observation cameras, PO1 and PO2, with distinct specifications. These cameras, when operating in full-field mode, record an area of $22.7 \times 17.0\text{mm}^2$ at a resolution of 14.2μm. To optimize data acquisition, the cameras can switch to a reduced field of view (FOV) mode ($22.7 \times 3.8\text{mm}^2$), thereby minimizing readout time and enabling a maximum frame rate of 100 fps.
The ground-based experimental setup, originally identical to that on the ISS, has been upgraded with a modern CMOS camera featuring a FOV of 1600×1200 pixels, capturing scattered light from the microparticles with spatial resolution of 11.4μm. By reducing the readout range to 1600×1 pixels, the frame rate can be increased to a maximum of 210 fps. Interference filters are incorporated to block interference from plasma or manipulation laser (OM) radiation.
Several active particle manipulation tools are integrated into the setup. The optical manipulation (OM) laser, capable of delivering up to 20 W, allows for photophoretic force application. Additionally, the system features two radio-frequency (RF) coils (RF1 and RF2). RF1 is movable within the working area and can generate electric fields with variable signals up to 5 W of power. An electromagnetic (EM) manipulator enables the generation

of localized electromagnetic pulses at fixed points within the plasma volume. Furthermore, a thermal manipulator (TM) is incorporated, allowing for the creation of a thermal gradient by heating the plasma up to 40°C, thereby inducing a thermophoretic force.

Parabolic flight and ISS campaigns

Earth's gravitational field imposes an external stress on the dust component in laboratory experiments, thereby perturbing the Coulomb-coupled system. To mitigate these gravitational effects and preserve the integrity of the system, experiments should be conducted under microgravity conditions. Such conditions can be achieved through various methods, including free-fall platforms, parabolic flights aboard aircraft, sounding rockets, or orbital missions.
Parabolic flight (PF) experiments have been conducted during campaigns 37, 39, 40, and 42 between 2020 and 2024, organized by the German Aerospace Center (DLR) and executed by Nove Space, see Figure 1.4 left panel. Each campaign consisted of three consecutive flight days, with one flight per day, each comprising 31 parabolas. A single parabola consists of an initial ∼2g phase lasting approximately 20 seconds, followed by an operational phase of equivalent duration under microgravity conditions, concluding with another 2g phase as the aircraft transitions back to steady flight. The primary focus of the experiments is on the 0g phase, which provides a limited window for data acquisition and analysis [42].
To ensure precise execution of experiments during the operational phase, the PK-4 ground-based setup has been optimized for parabolic flight conditions. A significant advantage of the system is the ability to automate and script experimental procedures using the C Scripting Language (CSL), allowing for enhanced reproducibility and efficiency in data collection [40].
Additionally, experimental time with PK-4 onboard the International Space Station (ISS) was obtained during campaigns 15, 17, and 18, with data collected and processed in this thesis. Furthermore, the most recent campaigns, 19 and 20, were conducted in the capacity of commanding the experimental procedure at the French National Space Agency (CNES) in Toulouse. The primary advantage of ISS operations is the significantly extended experimental duration compared to parabolic flights. While parabolic flights provide only short windows for experimentation, ISS operations are primarily limited by heat dissipation, allowing for approximately 40 minutes of operation before requiring an equal-duration cooling break. This extended operational time not only alters the experimental procedures but also broadens the range of observable phenomena. For instance, the build-up process of a Coulomb crystal occurs over a longer timescale and often exceeds the duration of a single parabolic flight experiment.
The ability to perform experiments under microgravity conditions offers a unique opportunity to study microparticles with higher mass, which are typically subject to significant sedimentation and gravitational distortion under laboratory conditions. As physical phenomena can manifest differently in microgravity, experimental outcomes are not always predictable. Consequently, not all experiments produced analyzable data, and some were excluded from this thesis due to insufficient or inconclusive results. Nonetheless, these

Figure 1.4: Group photo of all science teams participating in the Parabolic Flight Campaign 42 (left), and the CADMOS operations team (right) at the Toulouse Communication Center, supporting scientific operations during International Space Station campaigns.

trials offered useful experience and helped to better understand the behavior of complex plasmas in space. Some of them are worth mentioning, even if the outcomes differ from what was expected.

One series of experiments focused on the agglomeration behavior of microparticles following plasma shutdown. In these experiments, particles were trapped by alternating the polarity of the electric field, resulting in the formation of symmetric structures resembling particle strings or even crystals, as shown in the top-left panel of Figure 1.5. Following plasma shutdown, these structures dissipated, as observed in the lower-left panel. However, the shutdown procedure itself induced unintended side effects, such as irregular and random particle motion. Subsequent morphological analysis did not reveal any persistent or well-defined structures, suggesting random movement.

Another promising application of complex plasmas lies in the investigation of turbulence, owing to their capacity to emulate fluid-like behavior. To study turbulent particle dynamics, an obstacle was designed and introduced into the experimental setup to perturb the drift motion of the particles (Figure 1.5, top-right panel), a configuration previously examined in simulations [43]. However, the obstacle significantly disturbed the background plasma, generating strong wake structures and influencing the outer boundaries. These effects were not anticipated by prior simulations, which failed to account for such extensive plasma modifications. As a result, turbulence could not be observed under any of the experimental conditions tested. An alternative approach to induce turbulence involved introducing a counter-directed neutral gas flow within the plasma tube (Figure 1.5, lower-right panel). Although some irregularities emerged in the particle trajectories, a reproducible and well-defined onset of turbulent cascades was not observed. Due to the limited reproducibility and the absence of a clear cascade formation, this approach was ultimately not pursued further. The lack of turbulence is most likely attributed to the rel-

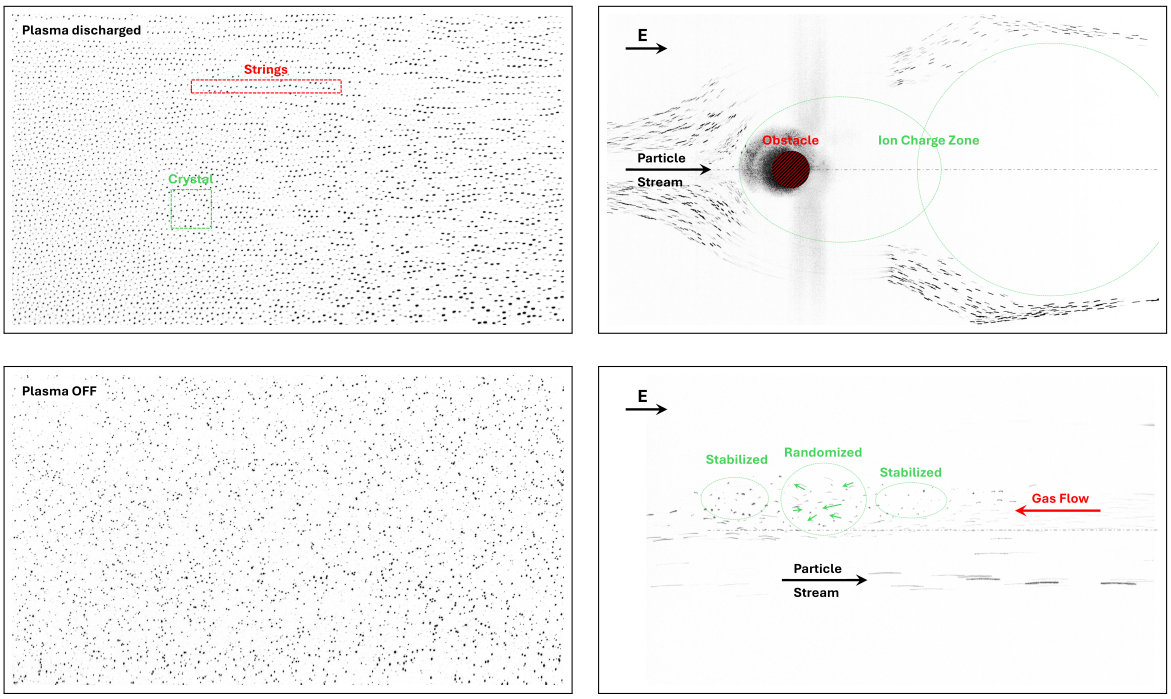

Figure 1.5: Example experiments conducted during PFCs, not included in further analysis. All images are contrast- and brightness-enhanced, and color-inverted. Left panel: Microparticles within a plasma discharge (top) form ordered structures such as strings and crystalline arrangements. After plasma shutdown (bottom), these structures dissolve, yielding a random distribution. Right panel: Attempts to induce turbulence. The introduction of an obstacle (top) generated a wakefield in the plasma but did not lead to the onset of turbulence. Similarly, the application of a counter-propagating neutral gas flow (bottom) failed to trigger sustained turbulent motion.

atively high damping rate of the system, which suppresses the development of instabilities necessary for a turbulent regime.
Despite these challenges, successful experiments were conducted to investigate microparticle dust-acoustic waves, electrorheological effects on microparticles and the ion drag force, yielding valuable data that contribute to the understanding of complex plasma interactions, published in three consecutive manuscripts.

1.2.2 Data Acquisition and Evaluation

In addition to the experimental challenges associated with data generation, it is equally critical to acquire and evaluate the collected data with the highest possible precision. The PK-4 facility utilizes digital cameras to capture images of microparticles in motion or at rest. The raw data consist of either drift lines or stationary dots, ideally on an non-illuminated black background. However, in practical scenarios, background illumina-

tion presents a significant challenge, as it influences the signal-to-noise ratio (SNR), which ultimately limits the detectability of the particles. During this Thesis machine learning techniques are utilized to overcome these challenges and bring systematic data acquisition and measurement to the next level. Representative sample images illustrating the investigated phenomena, dust-acoustic waves and isolated particle drifts, are presented in Figure 1.6.
All data evaluation processes in this project were performed using Python, and the corresponding codes are available as open-source repositories on GitHub [44, 45].

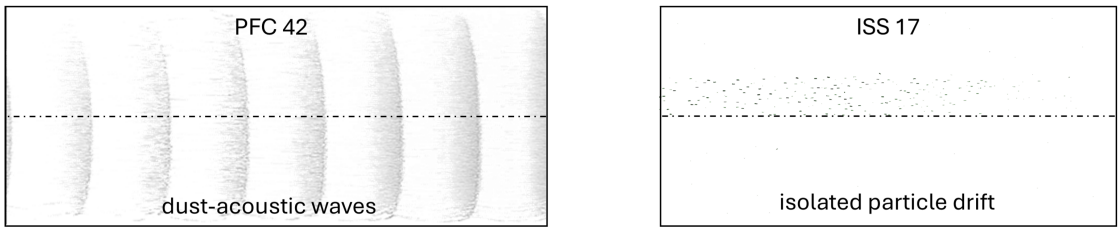

Figure 1.6: This figure presents two representative sample images for potential analysis. Both images have undergone color inversion and contrast enhancement to improve visibility. The left panel illustrates a dust-acoustic wave pattern, while the right panel depicts a low-density particle stream. Both cases were recorded under microgravity conditions.

Dust acoustic waves

Dust-acoustic waves (DAWs) are collective oscillations of charged microparticles within a plasma. Due to the rapid motion of individual particles, these waves appear as faint drift lines in recorded images, with their visibility decreasing as velocity increases and the signal-to-noise ratio (SNR) declines, potentially reaching a threshold where detection becomes infeasible. Rather than tracking individual microparticles, which is particularly challenging at high velocities, wave propagation dynamics are analyzed using the grayscale gradient signal extracted from recorded images.
A key parameter in image-based analysis is the local dust number density, n_d, and its spatial and temporal evolution. The wave crest corresponds to the regions of highest density and is directly proportional to the intensity of scattered light detected. The primary objective of this study is to accurately track the propagation of DAW wavefronts within the experimental field of view.
To achieve this, each image frame was reduced to a one-dimensional signal by summing brightness levels along the x-axis, yielding a profile proportional to local particle density variations. A representative example of the extracted raw data is presented in Figure 1.7.
To enhance signal clarity, noise reduction was performed using a frequency-domain filtering technique. Specifically, the signal was transformed into the frequency domain via Fourier

analysis, where the power spectral density (PSD) was used to identify and remove noise components through thresholding before reconstructing the signal in the time domain.

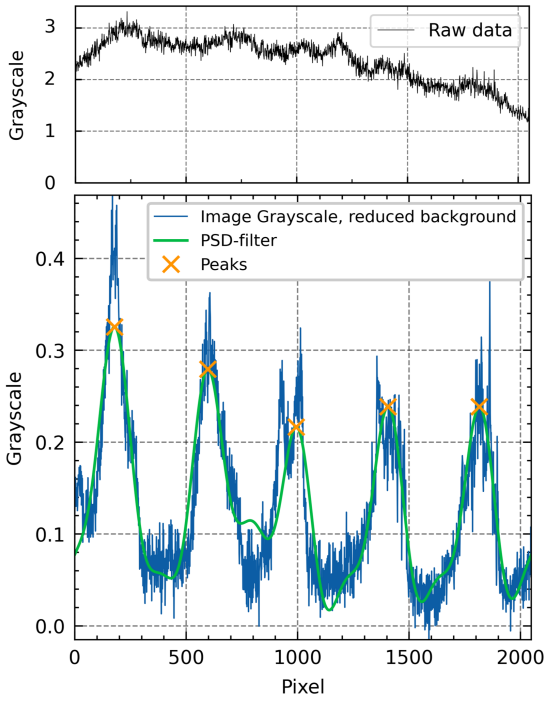

Figure 1.7: Extracted signal from a wave image: raw data (top panel) and processed signal (bottom panel) plotted along the x-axis. A power spectral density (PSD) filter was utilized to extract the wave crest position (Peaks) of a moving DAW.

This approach enables the identification of individual wavefronts within a single image and facilitates direct measurement of their wavelengths. Additionally, tracking wave peaks across multiple frames allows for high-precision measurements of wavefront velocities. The analysis pipeline, implemented in Python, provides a comprehensive framework for data acquisition and processing.
Furthermore, DAWs were observed in a compact moving cloud exhibiting a Doppler-shifted wave signature at a constant velocity. To characterize the movement of the envelope signal, a systematic parameterization approach was employed. Key parameters influencing measurement accuracy included the minimum pixel brightness threshold, the effect of Gaussian smoothing on the measured signal, the envelope step size, and the gating threshold for envelope detection. These parameters were dynamically adjusted to account for variations in the observed parameter space, including the potential impact of gravitational effects by selecting the appropriate section of the frame. To optimize envelope detection, a machine learning approach was implemented, utilizing a Bayesian search algorithm to refine parameter selection and enhance measurement precision.

Bayesian Statistics

Bayesian statistics is a probabilistic framework for statistical inference that integrates prior knowledge with observed data to iteratively refine parameter estimates. It is founded on Bayes' theorem, which provides a mathematical rule for updating probabilities upon receiving new evidence [46].
Bayes' theorem states that the posterior probability $P(\Theta|D)$ of a parameter Θ given the observed data D is proportional to the product of the prior probability $P(\Theta)$ and the likelihood $P(D|\Theta)$ [46]:

$$P(\Theta|D) = \frac{P(D|\Theta)P(\Theta)}{P(D)} \tag{1.43}$$

In this study, Bayesian statistics is employed to optimize image processing parameters by systematically refining estimates based on empirical data, as demonstrated in Chapters 2 and 3. The prior distribution encapsulates initial assumptions regarding tracking parameters such as pixel grayscale thresholds, Gaussian filter strength, and step size. The likelihood function quantifies the probability of the observed wavefront data given a specific parameter set. Through iterative updates, the posterior distribution converges toward optimal parameters, thereby enhancing the accuracy of wave tracking. Furthermore, Bayesian inference was applied in Chapter 4 to optimize plasma parameter estimations, improving model predictions of the ion drag force and ultimately increasing the reliability of the final results.

Ion Drag Force

Stationary microparticles appear as distinct, high-contrast features that remain detectable even in the presence of background noise. To analyze the ion drag force acting on these microparticles, precise trajectory tracking of individual particles in motion was essential. To achieve this, a machine-learning-based approach was implemented to enhance statistical robustness and accuracy, particularly in challenging conditions with a low SNR.
For particle tracking and tracing, a deep-learning algorithm developed by Max Klein and Nicklas Dormagen [47, 48] was adapted. This algorithm employs a U-Net convolutional neural network to detect particle drift lines, extract spatial coordinates, and link them across sequential frames. The application of this method enabled the extraction of $10^2 - 10^4$ trajectories per dataset, providing a substantial statistical sample. The resulting trajectory distributions followed a normal distribution centered around the true values, ensuring high precision and reliability.
Beyond data acquisition, Bayesian optimization was further utilized to refine the evaluation of the final computed results. This was accomplished by incorporating proposed physical models to predict experimental outcomes, iteratively adjusting parameter estimates based on observed deviations and associated uncertainties. Accurately determining plasma key parameters is crucial for computing the ion drag force. The primary parameters include the local electric field, electron temperature, and electron number density, which serve as

input variables for the model system. While plasma diagnostic in neon, free from disturbing dust grains, allowed direct parameter measurement [40], the corresponding values for argon plasma remain largely unknown. The Bayesian optimization method provided insights into how these parameters evolve in the presence of microparticle suspensions and enabled the prediction of previously undetermined values, thereby enhancing the accuracy of ion drag force calculations.

1.3 Scientific Context and Scope of this Thesis

The study of complex plasmas provides a unique platform for exploring fundamental interactions and collision processes at the atomic level. In this spirit, I aim to shed light on core plasma phenomena, particularly under extreme experimental conditions. A central challenge addressed in this thesis lies in the analysis of data obtained from observations at the lowest achievable pressures within the plasma chamber. I deployed and developed modern data analysis techniques have enabled the extraction of statistically significant insights from these measurements. This methodological advancement allowed for a new level of measurement precision, especially under demanding experimental conditions.
A key focus of this research is the difference between collective and isolated particle dynamics in complex plasmas. These two types of behavior involve different kinds of interactions and processes, and each requires its own analysis methods and experimental setup. The first part of this work focuses on collective phenomena, in particular the emergence of dust acoustic waves, which manifest as wave-like density modulations or particle groupings within the plasma. The last part of the thesis shifts attention to isolated particle dynamics, with a focus on the ion drag force acting on individual dust particles at very low pressures.

1.3.1 Publication I

This study, presented in Chapter 2, focused on analyzing dust-acoustic waves in low-pressure neon DC plasma using the PK-4 experiment in a ground-based configuration. The objective was to investigate wave structure morphology and propagation behavior and to identify deviations from predictions based on classical dispersion theory.
To meet this objective, a dedicated data processing pipeline was developed. The analysis started with basic preprocessing steps, such as background subtraction and contrast enhancement. Image sequences were then transformed into one-dimensional grayscale projections to highlight the wave profiles. A fully automated evaluation framework, implemented in Python, was established to identify dust acoustic wave crests in two-dimensional particle cloud projections and track their spatiotemporal evolution across consecutive frames. The method integrates image preprocessing, crest identification via intensity gradients and local maxima detection, and spatiotemporal tracking based on sub-pixel peak fitting and inter-frame correlation. Additionally, the observed waveforms exhibit a Doppler-like shift since the entire particle cloud is in motion. To account for this, a supplementary algorithm was implemented to detect the envelope of the moving cloud, enabling correction for the

background drift and accurate extraction of wave properties in the cloud's co-moving reference frame. This automation ensured consistent and reproducible results. It also enabled the extraction of wave parameters with high statistical accuracy, even under challenging conditions like non-uniform illumination or low signal-to-noise ratios.
Initial observations suggested the presence of screw-like or helical wave structures. However, tomographic image reconstruction revealed no evidence of such wave geometry or helical particle trajectories. Instead, the analysis showed that the observed wavefront deformations and phase velocities exceeding predictions from the linear dust-acoustic dispersion relation are attributed to spatial potential distortions near the boundary region. The wave morphology was conclusively linked to local electric field configuration asymmetries. These findings are further supported by the fact that the experiments are conducted under laboratory conditions, where gravitational forces cause a downward shift of the microparticles toward the lower boundary region of the plasma chamber.
The results underscore the strong sensitivity of dust-acoustic wave morphology to boundary-induced electric field asymmetries in DC discharges. Moreover, the developed methodology provides a robust and fully automated framework for the quantitative analysis of wave dynamics. This approach enables systematic investigations even under challenging conditions.

1.3.2 Publication II

The second study, presented in Chapter 3, investigated how the strength of the electric field influences the formation and propagation of dust-acoustic waves in neon plasma under microgravity conditions. The experiments were conducted during parabolic flight campaigns and aboard the International Space Station using the PK-4 setup.
The primary objective was to systematically investigate the influence of external electric field variations on wave excitation and the associated particle charging behavior. The experimental setup features a voltage-controlled DC discharge operating at a constant current, allowing precise adjustment of the electric field. To modulate the field acting on the microparticles, a polarity-switching procedure was applied at a defined frequency, resulting in an effective time-averaged electric field strength within the particle cloud. Image-based analysis techniques developed for previous studies were further refined and optimized using Bayesian inference, specifically for tuning parameters in the signal processing pipeline. This approach enhanced the robustness of wave crest detection and allowed for consistent evaluation across different datasets.
The results include an experimental estimation of the microparticle charge, yielding values in agreement with previously reported measurements. Furthermore, deviations from linear theoretical predictions provided clear experimental evidence of the electrorheological effect. The local charge environment was quantitatively assessed, and its influence on dust-acoustic wave propagation was identified. While the coupling between modulated electric fields and particle charging has been previously described in simulation studies, this work presents the first experimental validation of the effect under real plasma conditions, successfully confirming the exact underlying mechanism.
We also observed and demonstrated that a critical electric field strength marks the onset

of string formation among the microparticles. Beyond this threshold, the system evolved into a state of continuous string alignment, with spontaneous wave excitation consistently emerging at the boundaries. This behavior was shown systematically for the first time in an experimental context, revealing the direct coupling between electric field strength, electrorheological structuring, and wave dynamics.

1.3.3 Submitted Manuscript

The third study, presented in Chapter 4, focused on the application of machine learning techniques to improve the analysis of the ion drag force in complex plasma. The main objective was to enhance the extraction of key plasma parameters, such as electron number density, electron temperature, and electric field strength, to determine the ion drag force with the highest possible precision. The image analysis techniques developed for this purpose enabled the processing of large and noisy datasets acquired during PK-4 experiments conducted in argon and neon plasmas under microgravity conditions aboard the International Space Station.

A dedicated data processing pipeline incorporating a particle-tracking algorithm based on a trained neural network was developed. The algorithm was specifically designed to extract particle trajectories from drift lines and to link them across multiple image frames. Originally developed by collaborators, the system was extensively employed in this work to generate a high-quality trajectory dataset that served as the foundation for further analyses. The automated nature of the pipeline enabled high-statistics evaluation over large datasets and demonstrated robustness against common challenges such as non-uniform illumination and low signal-to-noise ratios.

In addition, the estimation of key plasma parameters required to compute the raw ion drag force was automated and refined using Bayesian optimization techniques. Established theoretical models were applied to predict experimental outcomes, with the optimization process systematically minimizing uncertainties in the underlying parameters. This approach ensured accurate estimation of the final ion drag force while yielding consistent and efficient determination of the relevant electron and ion properties across varying plasma conditions.

One of the key findings of this study is the influence of the electric field on ion temperatures in the ultra-low-pressure regime, as indicated by deviations from ideal Maxwellian distributions among the plasma constituents. These insights contribute to a deeper understanding of plasma behavior in non-ideal, low-collisionality environments and challenge common theoretical assumptions in plasma modeling.

Chapter 2

Publication I: Tilted Dust-Acoustic Waves in Low-Pressure DC Complex Plasma

Contributions of the Individual Co-Authors:

L. Wimmer:
Development of the experimental procedure
Data collection
Software development
Primary data acquisition
Methodology and analysis
Data visualization
Writing – original draft and revisions

A. S. Schmitz:
Support with data collection
Support analysis
Software support

M. Kretschmer:
Support with data collection
Review and editing

M. H. Thoma
Supervision
Support with data collection
Review and editing

Physics of Plasmas

RESEARCH ARTICLE | APRIL 12 2024

Tilted dust-acoustic waves in low-pressure DC complex plasma

L. Wimmer ; A. S. Schmitz ; M. Kretschmer ; M. H. Thoma

Phys. Plasmas 31, 043702 (2024)
https://doi.org/10.1063/5.0190499

Physics of Plasmas ARTICLE pubs.aip.org/aip/pop

Tilted dust-acoustic waves in low-pressure DC complex plasma

Cite as: Phys. Plasmas 31, 043702 (2024); doi: 10.1063/5.0190499
Submitted: 6 December 2023 · Accepted: 25 March 2024 ·
Published Online: 12 April 2024

L. Wimmer,[1,a)] A. S. Schmitz,[1] M. Kretschmer,[1,2] and M. H. Thoma[1]

AFFILIATIONS

[1]Institute of Experimental Physics I, Justus Liebig University Giessen, 35392 Gießen, Hesse, Germany
[2]Department of Electrical Engineering, Technische Hochschule Mittelhessen University of Applied Science, 35390 Gießen, Hesse, Germany

[a)]Author to whom correspondence should be addressed: Lukas.Wimmer@exp1.physik.uni-giessen.de

ABSTRACT

This study utilized the ground-based Plasmakristall-4 experiment to investigate the characteristics of dust-acoustic waves in low-pressure neon plasma generated through a direct current discharge. The experimental observations revealed the presence of dust-acoustic waves exhibiting a distinctive screw-like wavefront structure. Interestingly, the phase speed of these waves was slightly higher than the theoretical predictions. This deviation can be attributed to the influence of external forces and boundary conditions, which introduce asymmetry to the system and result in the deformation of wave patterns. To gain further insight, a comprehensive three-dimensional particle drift path reconstruction was conducted, providing a clearer understanding of the observed phenomena and confirming the findings obtained through the experimental analysis.

I. INTRODUCTION

Dust-acoustic waves (DAWs) are a fundamental phenomenon in dusty plasma physics and have been extensively studied both theoretically and experimentally over the last two decades. The primary plasma sources utilized in these experiments include the direct current (DC) glow discharge[1–3] and the capacitively coupled radio frequency (RF) discharge.[1,4] These setups have provided valuable insights into the behavior of DAWs and their interactions. Additionally, other plasma sources, such as inductively coupled RF-discharges,[4] have also been employed in specific investigations, broadening the scope of understanding regarding DAW phenomena and their relevance in various plasma configurations.[5] These diverse experimental approaches contribute to a comprehensive exploration of dusty plasma dynamics, specifically DAWs, with the origin associated with the ion streaming instability caused by sheath or bulk electric fields.[1]

While the self-excitation mechanism of DAWs is well-established,[5] studies have reported the emergence of unique wave patterns characterized by screw-like structures.[6] These observations challenge existing theoretical models and call for a deeper understanding of the effect of boundary conditions on DAWs.[7]

As DAWs play a major role in complex plasma research, many different models and equations were introduced to describe their behavior. The dispersion relation is a well-established method to describe and understand these waves. Various publications present the linear dispersion relation as the easiest form,[1] modifications of the linear dispersion relation,[7] as well the nonlinear dispersion relation.[8]

In this study, we investigate the properties of DAWs generated in a low-pressure DC discharge with micrometer-sized particles, executed with the experiment Plasmakristall-4 (PK-4) in ground-based environment.[9] The focus is on understanding the appearing waves in their macroscopic behavior and comparing them with theoretical predictions from the linear dispersion relation. In detail, we analyze the phase speed of the waves as well as the trajectory of the microparticles and explore the possibility of drift instability as the underlying mechanism. Furthermore, we analyze the wave structure on the microscopic level by investigating individual particle trajectories. The behavior of these waves is of great interest to researchers, as they have potential applications in various fields, including space physics, materials science, and astrophysics.

This paper is organized as follows: Sec. II provides a comprehensive description of the experimental setup, including the procedure and observations. Section III highlights the key experimental parameters and delves into a thorough discussion of the theory and final results. Finally, Sec. IV concludes the paper, summarizing the key findings and implications.

II. EXPERIMENTAL PROCEDURE AND OBSERVATIONS

The phenomenon of interest is studied using the parabolic flight setup PK-4, which is operated within a ground-based environment. Refer to Fig. 1 for an illustration of the setup. This experimental configuration enables the controlled investigation of specific phenomena under various conditions.[9,10] In detail, the plasma is created in its Π-shaped glass tube (with inner diameter $2 \times R = 3$ cm) with neon gas at a pressure range $p = 15 - 30$ Pa. The discharge current $I_{DC} = 0.5$ mA is used to generate DC discharge in the 86 cm long tube and provides a suitable environment to analyze multi-particle phenomena like DAWs with the help of green laser illumination system and a digital camera.[10] In this study, all observations were captured using a complementary metal-oxide-semiconductor (CMOS) camera with 4 Megapixel resolution, offering a pixel size of 11.8 μm. The resulting field of view was 24×24 mm, and the recordings were conducted at a frame rate of 80 fps. The experimental procedure starts with the injection of a cloud of microparticles with a diameter (d) of 1.3 μm, composed of melamine-formaldehyde material of density $\rho_d = 1.5\,\mathrm{g/cm^3}$, possessing a mass of $m_d = 1.8 \times 10^{-11}$ g. The microparticles acquire a charge of about 1500 e by collecting electrons and ions from the plasma and drift through the plasma chamber due to the longitudinal electric field of about 2 V/cm in the positive column of the discharge. The microparticles are levitated against gravity by the radial electric field in the plasma sheath above the bottom of the glass tube. This particle cloud exhibits stable drifting at a constant velocity through the chamber, with counteracting ions resulting in a two-stream instability leading to the generation of self-excited dust-acoustic waves. In the DC discharge of PK-4, self-excited DAWs are observed at pressures below 50 Pa. The phenomena under investigation reveals disturbed and tilted wavefronts, reminding of a screw-like or helical wave structure.

Reduction of the chamber pressure results in a stronger expression of the screw-like wave shape, see Figs. 2(a)–2(d). The major focus is, in this instance, on the lowest possible pressure allowing a reasonable analysis. Blue lines on the left side of the front view images

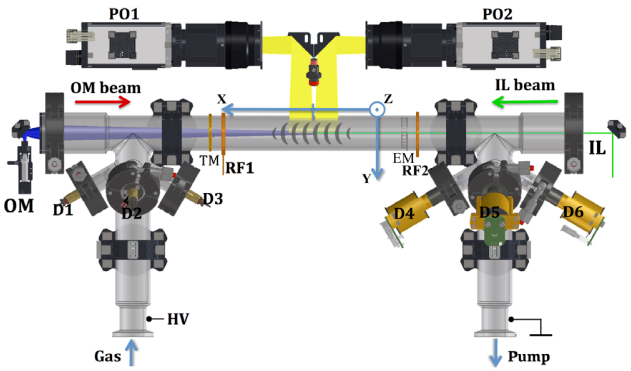

FIG. 1. A schematic depiction is presented, illustrating the experimental setup and procedure employed. Reprinted with permission from Kretschmer *et al.*, IEEE Trans. Plasma Sci. **44**, 458–462 (2016). Copyright 2016, IEEE.[11] The process involved injecting a densely populated particle cloud into the chamber, which then traversed through the chamber. Key components and manipulation tools are identified, including the illumination laser (IL) and optical manipulation laser (OM). Additionally, the setup includes radio frequency (RF) coils and electromagnetic (EM) and thermal manipulators (TM). Particle injection is achieved using dispensers D1–D6, and the observed phenomena are captured by the particle observation cameras (PO).

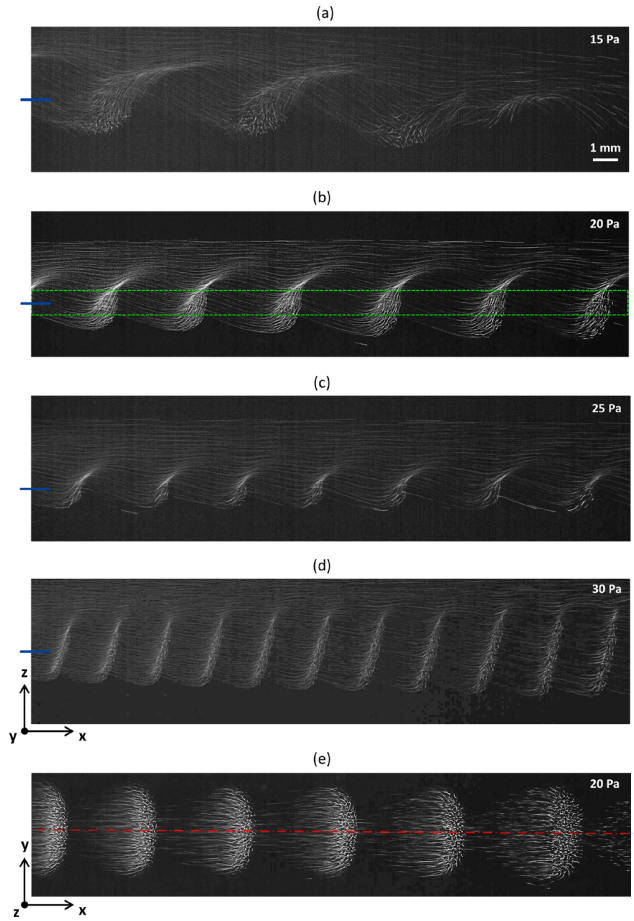

FIG. 2. DAWs with tilted wavefronts in low-pressure neon plasma are depicted, showcasing increased brightness and contrast. Utilizing PK-4 for self-excitation via DC-discharge, the phenomenon is observed at pressures ranging from 15 (a) to 30 Pa (d). Reduced pressure leads to increased deformation, influenced by the stronger impact of the radial electric field. This deformation is a consequence of gravity, pushing particles off-axis. Panels (a)–(d) provide a front view image, while panel (e) offers a bottom perspective, revealing symmetry in the front view but differing in the bottom view. The center of the tube is marked in the bottom view by the red dash-dotted line, while the cloud positions r_z in front view are indicated by solid blue lines on the left side of the images. Additionally, panel (b) features a delineated green box, highlighting a region of interest for generating the space-time pattern in Fig. 3.

indicate the central position of the cloud r_z, as documented in Table I with respect to the tube center. To introduce an alternative perspective on the wave pattern, a secondary camera setup was implemented, involving a 90-degree right-handed rotation of the experimental apparatus around the x-axis. This setup enables the wave to be observed from a bottom-view perspective, as illustrated in Fig. 2(e). The image is specifically captured at the central cloud position r_z, with the red dash-dotted line indicating the tube center.

Unveiling three-dimensional information about the structure, the camera system executes a systematic scan. Initiating from the central cloud position r_z in the front view or the tube center in the bottom view, a scan proceeds until reaching the boundary or vice versa. The

TABLE I. This table offers a comprehensive overview of the critical parameters associated with the system, drawing from both literature* sources and measured values. The discharge current $I_{DC} = 0.5$ mA and the microparticle diameter $2a_p = 1.3\ \mu$m. Furthermore, $n_{i0} = n_{e0} + Z_d n_{d0}$.

Pressure, p (Pa)	15	20	25	30
Electron density*, n_{e0} (10^8 cm^{-3})	0.74	0.79	0.88	1.04
Ion density, n_{i0} (10^8 cm^{-3})	6.6	6.8	8.2	7.4
Electron temperature*, T_e (eV)	9.8	9.0	8.7	8.5
Ion temperature*, T_i (eV)	0.057	0.050	0.030	0.030
Reduced charge, z	0.39	0.39	0.39	0.39
Particle charge number, Z_d (e)	1724	1583	1530	1495
Dust number density, $n_{d0(r)}$ (10^5 cm^{-3})	3.4	3.8	4.8	4.3
Plasma-dust frequency, ω_{pd} (1/s)	1272	1235	1342	1241
Dust-neutral friction coefficient, β (1/s)	174	232	290	348
Wigner–Seitz radius, a (μm)	89	86	76	82
Dust cloud velocity, v_c (mm/s)	87.6	76.9	59.3	56.7
Radial wave position, r_z (mm)	3.5	3.8	2.4	3.0

scan speed, denoted as $v_{scan}(y, z)$, is consistently maintained at 5 mm/s in either the z- or y-direction, depending on the chosen perspective. This observational method presents a valuable opportunity to explore and discuss individual particle pathways in Subsection III C.

A green dashed green box illustrated in Fig. 2(b) serves as an example for the region of interest employed in each image, and is stacked over time to generate a spatiotemporal pattern, as depicted in Fig. 3. The scattered light intensity $I(x, t)$ is depicted offering a quantitative 2D analysis of the waves. The intensity $I(x, t)$ in Fig. 3 is directly proportional to the local microparticle number density $n_d(x, t)$. To determine the scattered light intensity $I(x, t)$, the average pixel intensities were computed within a confined rectangular area measuring 7×7 pixels across the region of interest. A significant observation is the absence of stable wave propagation in the space-time diagram at 15 Pa, revealing irregular behavior. All other pressures show up in a reasonable stable wave mode, which motivates a focus on the examination of the results obtained at 20 Pa. Noteworthy is the wave pattern at 30 Pa, uniquely displaying a positive trend surpassing a relative speed of zero, resulting in a wave propagating in ion direction, unlike the patterns observed at other pressures.

The fast Fourier transform (FFT) was utilized to convert the spatiotemporal data $I(x, t)$ from the space and time domain into the corresponding frequency wave-number domain creating a power distribution spectrum. This transformation yielded spectra of fluctuations, represented as $I^2(k, \omega/2\pi)$, which provide valuable insights into the distribution of wave energy in the wave number-frequency plane. Figure 4 visually illustrates these spectra, showcasing the intensity with a logarithmic scale. This approach enhances the contrast within the diagram, making it easier to discern and analyze the variations in wave energy across wave numbers and frequencies. Figure 4 reveals the individual slopes of the frequency-wave number vectors, which represent the average wave phase speed over time.[3] The findings are quantified through the execution of a linear regression analysis on the binary image derived from each power spectrum, applied to those possessing an energy amplitude exceeding 15 $\log(1/\text{s}^{-2}\,\text{mm}^{-2})$ and presented in the description of Fig. 4. Notably, at 15 Pa, no prominently visible or definitively assigned bright maximum is discernible in the FFT

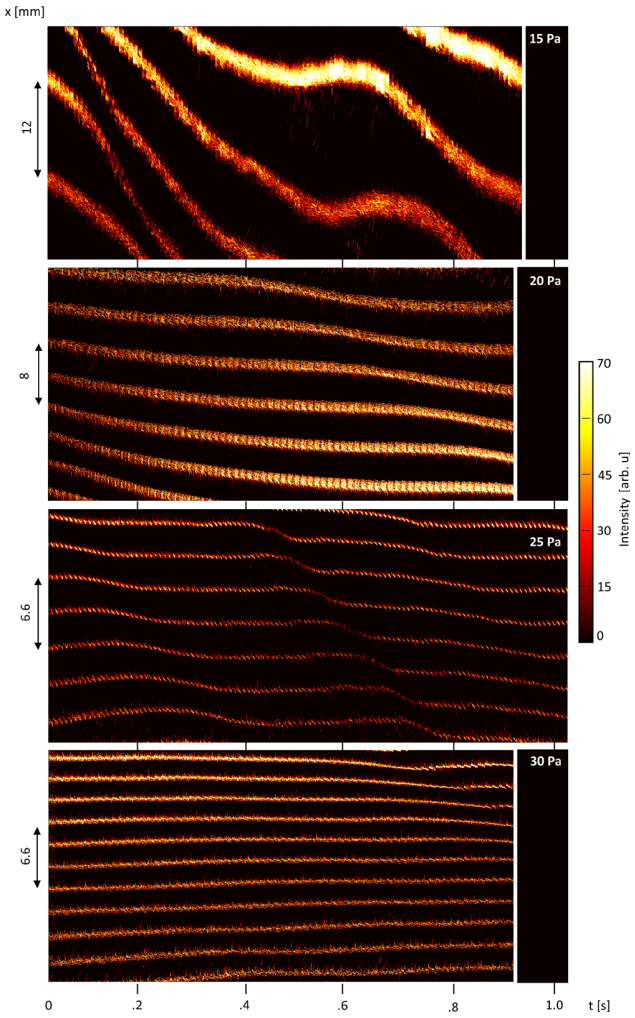

FIG. 3. This figure illustrates the spatiotemporal development of wave crests. The waves originate from wave slits that are selectively outlined within the area marked by a green dotted box, as depicted in Fig. 2(b). The intensity of scattered light, denoted as $I(x, t)$, is calculated following the description in the text. The x-axis represents the spatial expansion of crests in millimeters, while the y-axis represents time in seconds. Initially, the pattern at the lowest pressure of 15 Pa appears to be the most unstable in the ensemble, whereas all other patterns exhibit stable behavior throughout the period.

spatiotemporal spectra, indicating that the wave is not manifesting in a stable wave mode. However, in the case of higher pressures ranging from 20 to 30 Pa, clear maxima can be confidently assigned. A critical point to acknowledge is that the measured wave phase speeds do not directly represent the inherent phase speeds of the waves, as the particle cloud itself is in motion. Consequently, to obtain the original resulting phase speed $C_{DAW} = v_{ph} - v_c$, it is necessary to account for the difference between the measured phase speed and the velocity of the collective particle cloud.[12] The velocity of the particle cloud was determined through two distinct methods applied in different scenarios, specifically resolution considerations. First, a Python code based on *trackpy*[13] was employed. This reliable method is capable of accurately

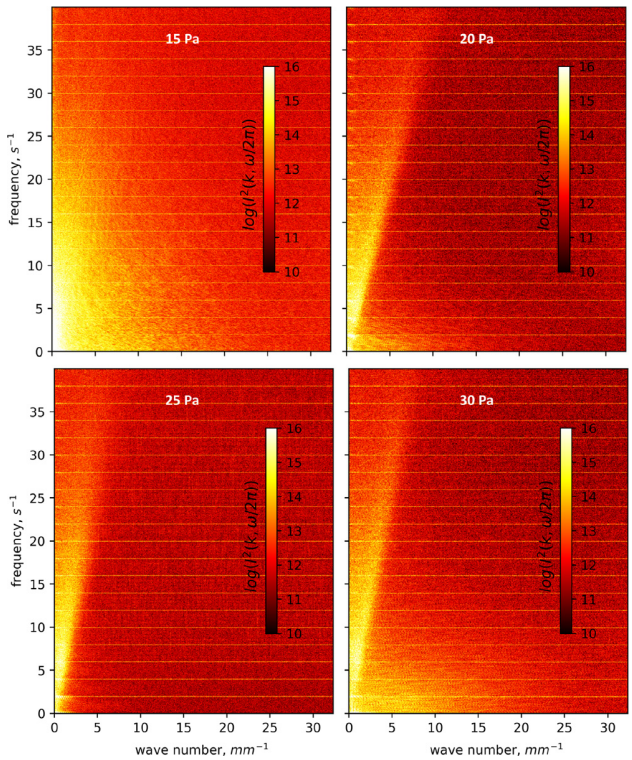

FIG. 4. The figure presents two-dimensional power distribution spectra that illustrate the relationship between frequency and wave number. These spectra are derived from the fast Fourier transform of the spatiotemporal pattern. Bright maxima in the spectra correspond to specific pressure-referenced propagation velocities. When evaluating the slopes for energy amplitudes surpassing 15 $\log(1/s^{-2}\,mm^{-2})$, approximate values for the average wave phase speeds over the period are obtained: $s_{20} \approx 4$ mm/s, $s_{25} \approx 7.5$ mm/s, and $s_{30} \approx 6$ mm/s. Notably, at 15 Pa, there is no distinct branch supporting the diagnosis of nonlinear behavior. It is crucial to emphasize that the final wave phase speed C_{DAW} is calculated as the difference between the measured speed of the cloud and the wave phase speed itself.

tracking individual particles from both the head and tail of the cloud by analyzing particle coordinates in 2D reference images. Alternatively, the cloud's collective motion was measured by condensing the 2D frame into a 1D grayscale signal. The follow up analysis involved detecting the wavefront and performing a linear regression over time to calculate the speed. To enhance the accuracy of this method, Bayesian optimization was implemented.[14]

By combining these measurements, a more precise assessment of the wave phase speed was obtained. It is noteworthy that the motion of the particle cloud introduced a maximum uncertainty of 5%. Additionally, the phase speed over time was measured by reducing the 2D frame to a 1D grayscale signal, demonstrating the capability to track each individual wavefront from frame to frame.

III. RESULTS AND DISCUSSION

A. Plasma and dust parameters

In Table I, we present a comprehensive summary of crucial plasma and dust parameters of significant importance. The electron temperature (T_e) and electron density (n_{0e}) were measured by Langmuir probe, in the absence of microparticles at the tube center.[10] To account for the radial distribution of the electron density in our model, we utilize a straightforward approximation represented by

$$n_e \approx n_{0e} J_0(2.4r/R), \tag{1}$$

where $J_0(r)$ is the Bessel function of the first kind, and R is the tube radius.[15]

The particle number density, represented by n_d, was determined through image reconstruction. The process involves stopping the waves via polarity switching, i.e., applying an AC field between 100 and 5000 Hz to the electrodes, at a specific point, resulting in the formation of a crystalline structure composed of particles. To assess the three-dimensional density, we employed the assumption of a Wigner–Seitz cell, utilizing data from particle tracking to determine the pair correlation function.[13] The first peak in this radial distribution corresponds to the mean radius r_0. The Wigner–Seitz radius is determined as $a = r_0/\rho$, with $\rho = 1.79 \pm 0.07$, enabling the calculation of the particle number density $n_d = 3(4\pi a^3)^{-1}$ with a maximum uncertainty of up to $\pm 12\%$.[16,17] Fig. 5 delineates the radial distribution of n_d measured at different pressures from the tube's off-center axis in the xz-plane. It is assumed that the particle cloud is symmetric in various directions.[18] The particle density distribution increases with r_z, indicating a saturation trend. This shift is attributed to the external influences of gravity and the opposing radial electric field. It is worth noting the vertical lines in Fig. 5, which highlight the determined radial cloud positions of the DAWs. These positions serve as reference points for quantifying particle densities based on the radial position (r_z).

The individual particle charge Z_d in the center of the discharge is estimated from[15]

$$Z_d = \frac{z a_p T_e}{e^2}; \quad z = 0.3 \pm 0.1. \tag{2}$$

The reduced charge, denoted as z, pertains to the potential of a microparticle within a neon complex plasma, considering its radius a_p. This potential was experimentally estimated and is also given in Eq. (2).[15] Several publications, including Refs. 15 and 19, have documented an observed increase in particle charge under gravitational conditions due

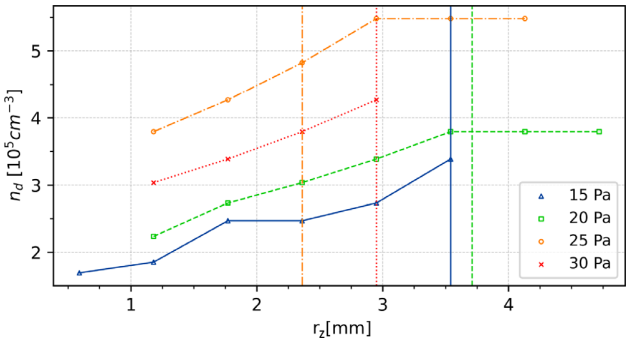

FIG. 5. The radial particle densities of individual pressures are displayed. The results were obtained by the reconstruction of the dust density from a Wigner–Seitz cell. This was accomplished by measuring the radial distribution function of each individual particle in the xz-plane. Vertical lines in the graph denote specific radial cloud positions, with r_z representing the distance measured from the tube center. Refer to Table I for all numerical values and results.

to a more substantial impact of the ambipolar electric field of the plasma sheath region. This region is distinguished by accelerated ion flows, leading to an increase in particle charge when compared to situations where particles are positioned in proximity to the tube axis (i.e., in microgravity conditions). Considering this, the adjusted reduced charge underwent a recalibration. This calibration procedure involved aligning the theoretical predictions of wave phase speeds for pressures greater than 20 Pa. This alignment was achieved by fitting the parameter z within the linear predictions for the wave phase speeds to match the experimental observations, as depicted in Fig. 6 with horizontal lines. Our focus during this fitting process was on the peak speed of individual wave phase speeds observed over time. This emphasis is justified by the wave crests exhibiting maximum amplitude, aligning with the concept of a saturation process and the peak interaction between particles.[20] The recalibration resulted in an increase in the parameter z to $z = 0.39$, while accounting for the inherent uncertainties in the measurements.

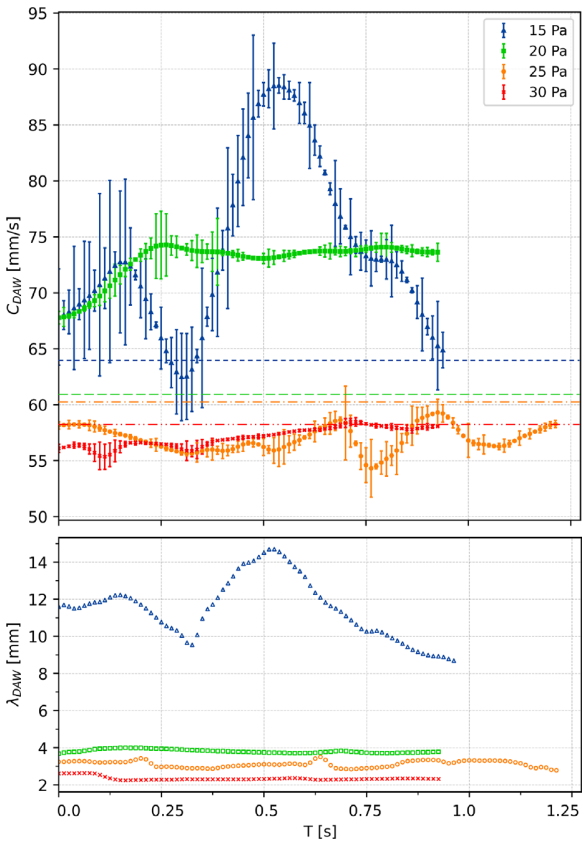

FIG. 6. In the top figure, the plot showcases the variation of the dust-acoustic wave phase speed, denoted as C_{DAW}, as a function of time. Horizontal lines represent the linear theoretical predictions corresponding to different pressures, while considering a reduced charge of $z = 0.39$, and a fixed ion temperature. In the bottom figure, the plot illustrates the temporal evolution of the dust-acoustic wavelength, represented by λ_{DAW}.

B. Linear dispersion relation

The dispersion relation is a valuable tool to assess the experimental data and results for DAWs in complex plasmas, particularly in its linear form. The derivation of the dispersion relation for DAWs takes into account three charged species: electrons, ions, and dust particles, all of which are assumed to be undergoing linear motion along the x-axis. However, following the standard textbook procedure and using the quasi-neutrality condition, $n_{i0} = n_{e0} + Z_d n_{d0}$, the dispersion relation is simplified by assuming cold dust ($T_d = 0$) and cold ions ($T_i \ll T_e$) to[21]

$$\omega^2 + i\beta\omega = \frac{\omega_{pd}^2 k^2 \lambda_{D,i}^2}{1 + k^2 \lambda_{D,i}^2}, \tag{3}$$

with the wave and dust plasma frequency ω, ω_{pd}, the dust-neutral friction coefficient β, the wave vector k, and the ion Debye length λ_{Di}. At this point, we have to take a closer look at β, given its role in characterizing the damping rate of the linear system,[21]

$$\beta = \frac{8 \cdot \delta}{\pi} \cdot \frac{p}{a_p \rho_d v_{th,n}}, \tag{4}$$

with the Epstein coefficient[22] δ assumed to be 1.44. Additionally, the neutral thermal velocity, denoted as $v_{th,n}$ and determined by $v_{th,n} = \sqrt{k_b T_n / m_n}$, is fixed at 320 m/s. Here, k_b denotes the Boltzmann constant, m_n represents the neutral mass, and $T_n = 0.025$ eV stands for the neutral gas temperature. A quantitative analysis of the interplay between the dust-friction parameter and the plasma-dust interaction frequency reveals pronounced effects,[21] particularly in the pressure range exceeding 20 Pa, expressed by the relation $\beta = (2.1 - 2.8)\omega_{pd}$. This finding predicts a significant impact in the context of wave damping. For pressures in the lower region, the damping is reduced to $\beta = (0.18 - 0.13)\omega_{pd}$. A direct comparison with the measured wave frequency and its influence is problematic, as the actual phase frequency deviates from that relative to the background gas. However, we aim for a straightforward discussion using a linear approach. Therefore, we assume zero damping in the subsequent sections of this paper. Additionally, taking into account small wave numbers where $k^2 \lambda_{Di}^2 \ll 1$, a condition met in all observed cases, the dust-acoustic phase speed C_{DAW} is determined by

$$C_{DAW} = \omega_{pd} \lambda_{Di} = \sqrt{\frac{k_B T_i}{m_d} \cdot \frac{n_{d0}}{n_{i0}} \cdot Z_d^2}, \tag{5}$$

with the ion temperature denoted as T_i and the mass of a single micro-particle denoted as m_d. All important parameters are listed in Table I. In Table II, the experimentally measured wave phase speeds are listed and compared to those theoretically calculated by the linear theory.

Figure 6 presents the results of wave phase speeds and wavelength over time for dust-acoustic waves measured within a specific pressure range. The horizontal lines in the graph represent wave phase speeds predicted by linear theory and Eq. (5). Different line styles correspond to various pressure conditions, with the particle density, and the reduced charge number ($z = 0.39$). The phase speed measurements at 30 and 20 Pa exhibit notable stability and accuracy. However, the result at 25 Pa displays some oscillation, while the observation at 15 Pa clearly demonstrates instability. This observation is consistent with the

TABLE II. This table offers a comprehensive overview of the conclusive results obtained from numerical analytics. It presents the experimental data alongside the theoretical predictions derived from the linear dispersion relation. For each specific pressure, the theoretical predictions are provided both with and without the adjusted ion temperature. The adjusted ion temperature incorporates the impact of the boundary electric field, leading to an increased mean free path of the ions, resulting in higher temperature and an augmented wave phase speed. This effect becomes significant when the pressure falls below 25 Pa, as demonstrated by a comparison with the measured experimental data. In the case of a fixed ion temperature, it is assumed to be at room temperature.

p (Pa)	λ (mm)	$C_{DAW}^{\text{exp}}\left(\frac{\text{mm}}{\text{s}}\right)$	lin. C_{DAW}^{theo}	adj. $\left(\frac{\text{mm}}{\text{s}}\right)$
15	14.5	88.1 ± 7.5	63.8	88.2
20	3.8	74.8 ± 2.1	60.5	78.9
25	3.1	59.3 ± 3.4	60.2	60.2
30	2.4	58.2 ± 1.1	58.4	58.4

periodogram depicted in Fig. 3 and the wave-energy spectrum in Fig. 4. The wavelength λ exhibits a more stable behavior over time in response to changes in phase speed.

Focusing on the two most precise measurements of the phase speed, the result at 30 Pa aligns well with the theoretical predictions but exhibits poor agreement at low neon pressure ($p = 20$ Pa). In Ref. 4, a similar discrepancy is described by considering the deviation of the ion temperature ($\tilde{T}_i$) at very low pressures ($p < 25$ Pa). Instead of the ions having room temperature, as initially assumed in Eq. (5), the mean free path ($l_i \approx T_n/p \times \sigma_{in}$, with $\sigma_{in} \approx 10^{-14}$ cm^2) of the ions increases, resulting in higher ion temperature.[23] This, in turn, increases the phase speed of the dust-acoustic waves at low pressures, as described in the following:[4]

$$\tilde{T}_i = \frac{2}{9} l_i e E_{0,r}. \tag{6}$$

The rise in velocity C_{DAW} suggests ion heating occurring within the ambipolar electric field ($E_{0,r}$), where the electric field was estimated from[15]

$$E_{0,r} = 2.4 \frac{T_e}{eR} \frac{J_1(2.4r/R)}{J_0(2.4r/R)}, \tag{7}$$

with the Bessel functions of the first kind $J_{0,1}(r)$, of order 0 and 1.

The calculated electric field values, $E_{0,r_z}(15\,\text{Pa}) = 4.62\,\text{V/cm}$ and $E_{0,r_z}(20\,\text{Pa}) = 4.57\,\text{V/cm}$ from Eq. (7), yield additional ion temperatures of $\tilde{T}_i(15\,\text{Pa}) = 0.027$ eV and $\tilde{T}_i(20\,\text{Pa}) = 0.020$ eV, respectively. The finalized ion temperatures (T_i) can be found in Table I. Now, the predictions align remarkably well with the experimental observations, underscoring the substantial impact of the ion mean free path on the phase speed of self-excited dust-acoustic waves in complex plasma. This influence is particularly notable within the low-pressure regime ($p < 25$ Pa), where the ion mean free path achieves a magnitude significant enough to exert a pronounced effect. Figure 7 presents a comparison between the experimentally measured data and the fitted theoretical predictions. These fits were accomplished through linear regression of a polyfit model. This analysis elucidates the specific pressure regime to which each individual experimental data point belongs. It highlights that linear theory aligns well for $p \geq 25$ Pa, but the inclusion of the ambipolar electric field's impact becomes necessary at lower pressures. The case of dust-acoustic waves driven by ions demonstrates that increasing T_i serves as a valid approach in this context.

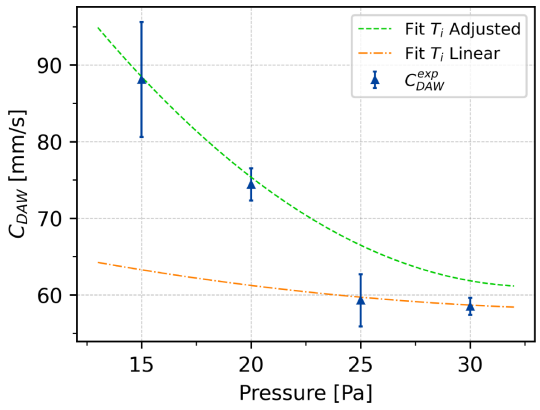

FIG. 7. The plot illustrates the experimental measurements of C_{DAW}, plotted against neon pressure. The measured data points are represented by blue triangles. Additionally, the green dashed line is employed to represent a fit of the adjusted theoretical prediction, incorporating an adjusted ion temperature T_i. The orange dash-dotted line corresponds to a fit of linear prediction, without ion temperature adjustments. The function fitted on both was $C_{DAW}^{\text{theo}} \propto p^{-1/2}$. It demonstrates that in the case of ion-driven DAWs propagating at pressures below 25 Pa ($p < 25$ Pa), the ion temperature plays a significant role in fine-tuning the predictions.

C. Dust-acoustic wave tomography

A scan in y-direction was executed to reconstruct a tomographic front view, depicted in Fig. 8. This allows us to examine the structural evolution in depth. However, no discernible changes in shape became evident while scanning through the wave, revealing sinusoidal-like pathways. To provide an alternative perspective, the experimental setup underwent a 90-degree rotation, and the scan was executed in a similar fashion. The result is displayed as image stack in Fig. 9. The bright spot indicates a particle population in a wavefront, and the

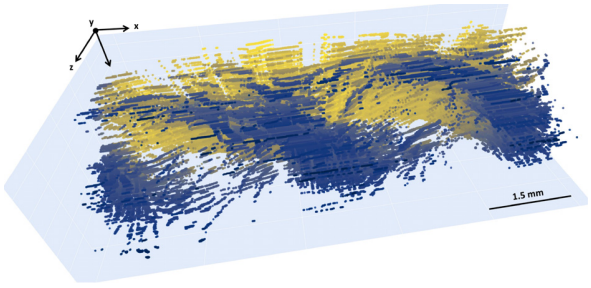

FIG. 8. This figure presents a tomographic reconstruction illustrating the drift lines of a wave at 20 Pa. The reconstruction was achieved by scanning the phenomenon in the y-direction with a depth of 1.6 mm. The color gradation signifies the depth, aiding in the identification of the three-dimensional structure. Yellow shading represents particle paths further back, while blue denotes positions closer to the front. The pathways maintain a consistent pattern throughout the y-direction scan, displaying sinusoidal behavior with a gravitational inclination. Particles unable to escape the wavefront are compelled to exit at the bottom side due to the escalating boundary layer potential, resulting in a brighter and increased concentration of particle drift lines.

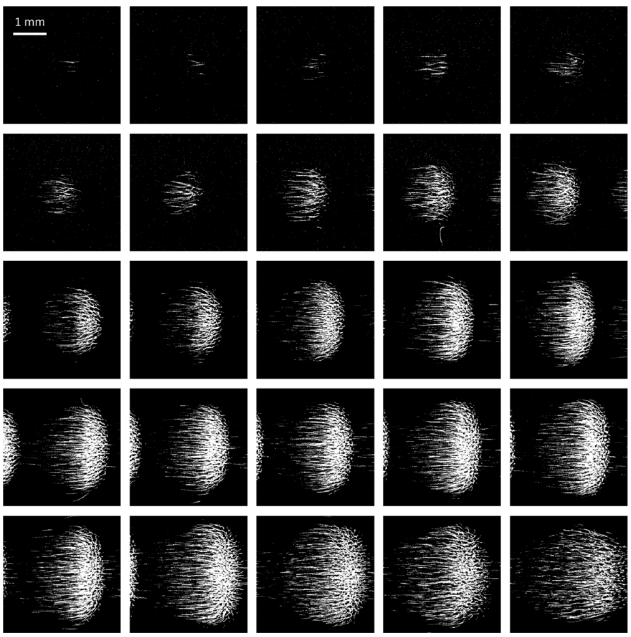

FIG. 9. This diagram illustrates a tomographic image series in the *xz*-plane, showcasing the drift lines of a wave at 20 Pa. The image was produced by scanning the phenomenon in the z-direction, covering a depth of 1.6 mm. The orientation from the upper left to the lower right corresponds to the bottom-to-top direction. Bright spots indicate particle populations, while fainter lines represent particle drift pathways. In contrast to the previous perspective, the pathways now display straight lines without any indication of circular or sinusoidal movement. The particle population decreases toward the boundary layer due to the influence of the parabolic-shaped electric field potential wall.

fainter lines represent a particle path if a particle decides to defuse to the follow-up wavefront. It is important to notice that no circular or sinusoidal movement can be found in the *xz*-plane, which allows us to make the following statement.

In the analytical framework classifying our observations, we employ the mathematical definition derived from the description of a helix.[24,25] This assumption is based on considering a helix or coil as a curve where the tangent maintains a constant angle with a fixed line. Mathematically, this can be expressed as $x = r \cdot \cos(t)$, $y = r \cdot \sin(t)$, $z = c \cdot t$, for $t \in [0, 2\pi)$, where r represents the radius of the helix, and $2\pi c$ is a constant determining the vertical separation of the helix's loops. Lancret's theorem establishes a critical property, stating that the necessary condition for a curve to be a helix is the constancy of the ratio of curvature to torsion.[25] It describes the shortest path between two points on a cylinder, offering a logic possibility for a particle pathway.[24]

In Fig. 8, we observe a periodic behavior of the wave, aligning with our anticipated expectations. The particle pathways distinctly exhibit a sinusoidal movement. However, considering the second perspective shown in Fig. 9, this symmetry is disrupted. The structure displays straightened pathways, unlike of any helical characteristics. Consequently, a mathematically defined helical pathway is not discernible in the analyzed structure. In accordance with Lancret's theorem, the presence of a constant curvature to torsion ratio is mandatory, and our analysis reveals this condition to be absent upon a 90-degree rotation of our perspective.

Physically, we are not inclined to presume a helical structure, as defined in the mathematical sense. A plausible scenario arises when overlaying the potential regions that manifest in the two perspectives. The potential is directly proportional to the brightness of the individual images. When superimposed, these patterns unveil a sinusoidal potential in the *xz*-plane (wave potential) and a quadratic rise in the *yz*-direction toward the potential wall (due to gravity). Within this potential, a particle is forced to diffuse from wavefront to wavefront, following the shortest path through the potential well. In lower pressure conditions, this potential exerts a more pronounced influence, thereby complementing the reference image.

IV. CONCLUSION

The experiments were conducted in a neon plasma, utilizing monodispersed melamine-formaldehyde microparticles with a size of 1.31 μm in diameter. The experiments were carried out at pressures ranging from $p = 15$–30 Pa. By systematically increasing the pressure, the dynamic behavior of the waves was investigated, and various wave properties were measured.

Notably, the observed waves exhibited distinctive screw-like wavefront structures, particularly at pressures below 25 Pa, with the effect being more pronounced at lower pressures. A significant emphasis was placed on comprehensively understanding this phenomenon at both microscopic and macroscopic levels. It was determined that the interaction between the particles and the plasma sheath layer played a crucial role in shaping the observed wave behavior. As the influence of the plasma sheath layer intensified with reducing pressure, not only did the wave phase speed increase, but the wavefront distortions also manifested more prominently in the form of stronger screw-like expressions.

By comparing the numerical results with the linear theory, the impact of increased ion temperature resulting from reduced pressure and ambipolar electric field was elucidated. The work presented by Ref. 26 presents an alternative treatment of the linear dispersion relation that incorporates neutral-dust collisions. Future experiments can incorporate this solution into their analysis to validate its accuracy. Furthermore, a tomographic scan of a perturbed wave was conducted, allowing for a microscopic analysis by visualizing the individual pathways of the particles. This approach provided insights into the mechanisms contributing to wave formation, revealing that the wave shape emerges from the superposition of longitudinal and radial electric fields, without substantial evidence supporting the existence of helical waves. Basically, longitudinal and radial self-excited DAWs are superposed.

In summary, by assuming a linear dispersion relation for the DAWs, we confirmed the findings of Ref. 4, implying an increase in the ion temperature at low pressures. In addition, we observed a distortion of the wave fronts in the plasma sheath, suggesting a helix or screw-like structure.

ACKNOWLEDGMENTS

This work was supported by DLR under Grant No. 50WM2044. We thank Manis Chaudhuri for reading the manuscript and providing valuable suggestions.

AUTHOR DECLARATIONS

Conflict of Interest

The authors have no conflicts to disclose.

Author Contributions

L. Wimmer: Conceptualization (equal); Data curation (lead); Formal analysis (lead); Investigation (lead); Methodology (lead); Software (lead); Visualization (lead); Writing—original draft (lead). **A. S. Schmitz:** Data curation (supporting); Formal analysis (supporting); Investigation (supporting); Software (supporting). **M. Kretschmer:** Data curation (supporting); Writing—review & editing (supporting). **M. H. Thoma:** Conceptualization (lead); Supervision (equal); Writing—review & editing (supporting).

DATA AVAILABILITY

The data that support the findings of this study are available from the corresponding author upon reasonable request.

REFERENCES

[1]R. L. Merlino, "25 years of dust acoustic waves," J. Plasma Phys. **80**, 773–786 (2014).
[2]V. E. Fortov, A. G. Khrapak, S. A. Khrapak, V. I. Molotkov, A. P. Nefedov, O. F. Petrov, and V. M. Torchinsky, "Mechanism of dust-acoustic instability in a direct current glow discharge plasma," Phys. Plasmas **7**, 1374–1380 (2000).
[3]V. V. Yaroshenko, S. A. Khrapak, M. Y. Pustylnik, H. M. Thomas, S. Jaiswal, A. M. Lipaev, A. D. Usachev, O. F. Petrov, and V. E. Fortov, "Excitation of low-frequency dust density waves in flowing complex plasmas," Phys. Plasmas **26**, 053702 (2019).
[4]V. E. Fortov, A. D. Usachev, A. V. Zobnin, V. I. Molotkov, and O. F. Petrov, "Dust-acoustic wave instability at the diffuse edge of radio frequency inductive low-pressure gas discharge plasma," Phys. Plasmas **10**, 1199–1208 (2003).
[5]R. L. Merlino, "Dust-acoustic waves driven by an ion-dust streaming instability in laboratory discharge dusty plasma experiments," Phys. Plasmas **16**, 124501 (2009).
[6]M. Chaudhuri *et al.*, "Observation of nonlinear helical and screw wave structures in PK4," in Where Manis Chauduri Was Presenting His Initial Findings on Special Shaped Waves in PK4 at PK3-plus Symposium (2009).
[7]P. K. Shukla, "Twisted dust acoustic waves in dusty plasmas," Phys. Plasmas **19**, 083704 (2012).
[8]V. V. Yaroshenko, "Nonlinear dispersion relation for dust-acoustic waves in complex plasmas," Phys. Rev. E **102**, 023201 (2020).
[9]C. Dietz, M. Kretschmer, B. Steinmüller, and M. Thoma, "Recent microgravity experiments with complex direct current plasmas," Contrib. Plasma Phys. **58**, 21–29 (2018).
[10]M. Y. Pustylnik, M. A. Fink, V. Nosenko, T. Antonova, T. Hagl, H. M. Thomas, A. V. Zobnin, A. M. Lipaev, A. D. Usachev, V. I. Molotkov, O. F. Petrov, V. E. Fortov, C. Rau, C. Deysenroth, S. Albrecht, M. Kretschmer, M. H. Thoma, G. E. Morfill, R. Seurig, A. Stettner, V. A. Alyamovskaya, A. Orr, E. Kufner, E. G. Lavrenko, G. I. Padalka, E. O. Serova, A. M. Samokutyayev, and S. Christoforetti, "Plasmakristall-4: New complex (dusty) plasma laboratory on board the International Space Station," Rev. Sci. Instrum. **87**, 093505 (2016).
[11]M. Kretschmer, T. Antonova, S. Zhdanov, and M. Thoma, "Wave phenomena in a stratified complex plasma," IEEE Trans. Plasma Sci. **44**, 458–462 (2016).
[12]S. Jaiswal, M. Y. Pustylnik, S. Zhdanov, H. M. Thomas, A. M. Lipaev, A. D. Usachev, V. I. Molotkov, V. E. Fortov, M. H. Thoma, and O. V. Novitskii, "Dust density waves in a DC flowing complex plasma with discharge polarity reversal," Phys. Plasmas **25**, 083705 (2018).
[13]J. C. Crocker and D. G. Grier, "Methods of digital video microscopy for colloidal studies," J. Colloid Interface Sci. **179**, 298–310 (1996).
[14]P. I. Frazier, "A tutorial on Bayesian optimization," arXiv:1807.02811 [stat.ML] (2018).
[15]T. Antonova, S. A. Khrapak, M. Y. Pustylnik, M. Rubin-Zuzic, H. M. Thomas, A. M. Lipaev, A. D. Usachev, V. I. Molotkov, and M. H. Thoma, "Particle charge in PK-4 DC discharge from ground-based and microgravity experiments," Phys. Plasmas **26**, 113703 (2019).
[16]V. Nosenko, M. Pustylnik, M. Rubin-Zuzic, A. M. Lipaev, A. V. Zobnin, A. D. Usachev, H. M. Thomas, M. H. Thoma, V. E. Fortov, O. Kononenko, and A. Ovchinin, "Shear flow in a three-dimensional complex plasma in microgravity conditions," Phys. Rev. Res. **2**, 033404 (2020).
[17]B. Liu, J. Goree, and W. D. Suranga Ruhunusiri, "Characterization of three-dimensional structure using images," Rev. Sci. Instrum. **86**, 033703 (2015).
[18]S. Mitic, B. A. Klumov, U. Konopka, M. H. Thoma, and G. E. Morfill, "Structural properties of complex plasmas in a homogeneous DC discharge," Phys. Rev. Lett. **101**, 125002 (2008).
[19]S. A. Khrapak, M. H. Thoma, M. Chaudhuri, G. E. Morfill, A. V. Zobnin, A. D. Usachev, O. F. Petrov, and V. E. Fortov, "Particle flows in a DC discharge in laboratory and microgravity conditions," Phys. Rev. E **87**, 063109 (2013).
[20]V. V. Yaroshenko, "Saturation of the ion drift instability in collisional complex plasmas by ion trapping," Phys. Rev. E **103**, 063209 (2021).
[21]A. Melzer, *Physics of Dusty Plasmas* (Springer, Cham, 2019).
[22]B. Liu, J. Goree, V. Nosenko, and L. Boufendi, "Radiation pressure and gas drag forces on a melamine-formaldehyde microsphere in a dusty plasma," Phys. Plasmas **10**, 9–20 (2003).
[23]S. A. Khrapak, P. Tolias, S. Ratynskaia, M. Chaudhuri, A. Zobnin, A. Usachev, C. Rau, M. H. Thoma, O. F. Petrov, V. E. Fortov, and G. E. Morfill, "Grain charging in an intermediately collisional plasma," Europhys. Lett. **97**, 35001 (2012).
[24]H. Steinhaus, *Mathematical Snapshots* (Courier Corporation, 1999).
[25]Ü. Çiftçi, "A generalization of Lancret's theorem," J. Geometry Phys. **59**, 1597–1603 (2009).
[26]S. A. Khrapak and V. V. Yaroshenko, "Low-frequency waves in collisional complex plasmas with an ion drift," Phys. Plasmas **10**, 4616–4621 (2003).

Chapter 3

Publication II: Impact of particle charge and electrorheology-effects on dust-acoutic waves in low pressure complex plasma under microgravity

Contributions of the Individual Co-Authors:

L. Wimmer:
Development of the experimental procedure
Data collection
Software development
Primary data acquisition
Methodology and analysis
Data visualization
Writing – original draft and revisions

N. Dormagen and M. Klein:
Software development
Data collection
Review and editing

M. Kretschmer, A. M. Lipaev, M. Schwarz, A.D. Usachev, O.F. Petrov:
Supporting developement of the experimental procedure and Data collection
Review and editing

M. H. Thoma:
Supervision
Data collection
Review and editing

PAPER • OPEN ACCESS

Impact of particle charge and electrorheology-effects on dust-acoustic waves in low pressure complex plasma under microgravity

To cite this article: L Wimmer *et al* 2025 *New J. Phys.* **27** 033001

IOP Publishing New J. Phys. 27 (2025) 033001 https://doi.org/10.1088/1367-2630/adb876

New Journal of Physics
The open access journal at the forefront of physics

Deutsche Physikalische Gesellschaft DPG
IOP Institute of Physics

Published in partnership with: Deutsche Physikalische Gesellschaft and the Institute of Physics

OPEN ACCESS

RECEIVED
19 November 2024

REVISED
14 February 2025

ACCEPTED FOR PUBLICATION
20 February 2025

PUBLISHED
28 February 2025

PAPER

Impact of particle charge and electrorheology-effects on dust-acoustic waves in low pressure complex plasma under microgravity

L Wimmer[1,*], N Dormagen[1,2], M Klein[1,2], M Kretschmer[1,2], A M Lipaev[3], M Schwarz[2], A D Usachev[3], O F Petrov[3], A V Zobnin[3] and M H Thoma[1]

[1] Institute of Experimental Physics I, Justus-Liebig University, 35392 Gießen, Germany
[2] NanoP, THM University of Applied Sciences, D 35390 Giessen, Germany
[3] Joint Institute for High Temperatures, Russian Academy of Sciences, 125412 Moscow, Russia
[*] Author to whom any correspondence should be addressed.

E-mail: lukas.wimmer@epx1.physik.uni-giessen.de

Keywords: complex plasma, two-stream instability, electrorheology, microgravity

Abstract

This study investigates the influence of particle charge and electrorheological (ER) effects on microparticle dynamics and dust-acoustic wave propagation in low-pressure complex plasmas under microgravity conditions. Experiments were conducted using PK-4 during parabolic flights and onboard the International Space Station to analyze dust particle behavior in direct current (DC) and DC polarity switching discharge plasma. Key findings reveal that variations in particle charge potential and ER effects significantly affect particle dynamics, especially at different gas pressures. Specifically, we validated a dimensionless charge potential of $z = 0.34 \pm 0.17$ in a DC neon plasma discharge, noting a rapid increase in this potential at pressures below 15 Pa. Furthermore, we observed a reduction in charge of up to 50% due to quadrupole effects induced by polarity switching. These results provide critical insights into plasma behavior in microgravity and the role of external electric fields in particle interactions.

1. Introduction

Plasma, commonly recognized as the fourth fundamental state of matter, exhibits unique electrical conductivity properties. It typically forms when gas molecules are ionized under conditions such as high temperatures, electrical discharges, or exposure to other ionizing sources of energy. This process results in the breakdown of the gas into a collection of freely moving charged particles, including electrons and ions. The ionized state sets plasma apart from the classical states of matter—solid, liquid, and gas. It is a key phenomenon in various technological applications, including but not limited to semiconductor processing, environmental monitoring, medical technology, and the generation of energy through controlled nuclear fusion. Significantly, plasma constitutes roughly 99% of the visible Universe, highlighting its importance in both earth-bound and cosmic contexts [1].

Within the field of plasma physics, complex plasmas containing micron-sized dust particles present intriguing properties and behaviors. One of the key phenomena observed in such environments is the dust-acoustic wave (DAW), a low-frequency and long-wavelength oscillation involving the dust particles themselves [2]. These waves are particularly interesting for study under microgravity conditions, such as those provided by space-based experiments, where gravitational effects are minimized, allowing for clearer observation of underlying plasma behaviors [3].

This study focuses on the impact of particle charge and electrorheology (ER) on the speed of DAWs in direct current (DC) discharge plasma under microgravity conditions. Electrorheology refers to the changes in the rheological properties of a fluid due to the presence of an alternating-current (AC) electric field. In the context of plasma, this phenomenon can significantly alter the interactions between charged dust particles, influencing both the characteristics of individual particles and DAWs.

Previous research has extensively explored the generation and propagation of DAWs in various plasma environments, including DC glow discharges and radio-frequency (RF) discharges [4, 5]. These studies have provided valuable insights into the mechanisms driving these waves and the conditions under which they occur. However, the influence of electrorheological (ER) effects, particularly under microgravity, remains an area requiring further investigation.

In microgravity, dust particles in plasma can achieve configurations and dynamics distinct from those observed under Earth's gravity. This environment facilitates the study of DAWs with minimal external perturbations, providing a clearer understanding of the fundamental processes involved. Additionally, the unique properties of ER fluids, where particles align into structured formations under an electric field, provide new insights into DAW dynamics [6, 7].

This paper aims to examine the phase speed of DAWs and the trajectories of dust particles in a low-pressure DC discharge plasma under microgravity. By analyzing these aspects, we aim to enhance the understanding of how particle charge and electrorheology influence wave propagation. The findings are expected to contribute to broader applications in space physics, materials science, and astrophysics, where understanding plasma dynamics at a granular level is crucial.

The effective interparticle interaction is governed by the time-averaged wake potential. Within the framework of the linear response formalism, this interaction becomes rigorously reciprocal (Hamiltonian). Consequently, one can directly apply the principles of statistical physics to describe the dynamics of ER plasmas. This theoretical understanding is crucial for predicting and controlling the behavior of DAWs under the influence of ER effects [8].

The organization of this paper is as follows: section 2 describes the experimental setup and procedures used to generate and observe DAWs. Section 3 discusses the key parameters and theoretical models applied in the analysis of experimental results. Finally, section 4 summarizes the key findings and implications of the study, providing insights into the complex interactions within plasmas influenced by ER effects under microgravity conditions.

2. Experimental setup and procedure

The investigation of dust acoustic waves (DAWs) was conducted using the PK-4 setup during parabolic flight (PFC) DLR campaign 42 and onboard the International Space Station (ISS) during campaign 15. Both plasma chambers, illustrated in figure 1, are identical, enabling a controlled study of specific phenomena under various conditions [9, 10].

In both setups, plasma is generated within a Π-shaped glass tube (inner diameter $2R = 3\,\mathrm{cm}$) filled with neon gas at a pressure range of $p = 15 - 40$ Pascal (Pa). A discharge current of $I_{\mathrm{DC}} = 0.5\,\mathrm{mA}$ is used to create a DC discharge in the 86 cm long tube, providing a suitable environment to analyze multi-particle phenomena using a green laser illumination system and a digital camera [10].

For the parabolic flight setup, observations were captured using a CMOS camera with a 4-megapixel resolution and a pixel size of $11.8\,\mu\mathrm{m}$. This setup resulted in a field of view (FOV) of $24 \times 24\ \mathrm{mm}^2$, with recordings conducted at a frame rate of 80 fps, as shown in the images in figure 1, right panel, for 40 and 15 Pascal. Due to the limited operation time in microgravity (approximately 22 s per maneuver), the procedure had to be both rapid and efficient.

In contrast, the ISS setup utilized cameras with a resolution of $14.2\,\mu\mathrm{m}$ and a smaller FOV of $23 \times 17\ \mathrm{mm}^2$, operating at 35 fps. The FOV height was adjusted to half in order to improve readout time and boost the frame rate to 60 fps. Additionally, the ISS setup allowed for the confinement of the particle cloud using RF coils, enabling detailed scans through the cloud to examine particle density and ensure a fully extended cloud with a high particle population [10].

The experimental procedure involved injecting a cloud of microparticles into the plasma chamber. Each microparticle had a diameter of $2a = 3.4\ \mu\mathrm{m}$, was composed of melamine-formaldehyde (MF) material with a density $\rho_{\mathrm{d}} = 1.5\,\mathrm{g\,cm^{-3}}$, and a mass of $m_{\mathrm{d}} = 3.24 \cdot 10^{-11}\,\mathrm{g}$. These particles acquired a charge of approximately 1500 e by collecting electrons and ions from the plasma. The longitudinal electric field of about $2\,\mathrm{V\,cm^{-1}}$ in the positive column of the discharge caused the particles to drift through the plasma chamber [10].

During the experiment, the particle cloud was transported bidirectionally through the tube by systematically modulating the effective electric field strength (E_{eff}) through polarity switching. Specifically, the duty cycle of the polarity-switching electric field was adjusted to directly control the E_{eff}. A 50% duty cycle results in an effectively neutral field ($E_{\mathrm{eff}} = 0\%$), while reducing the duty cycle proportionally increases the magnitude of E_{eff}. This method allowed us to observe the behavior of self-excited DAWs, which occur at pressures below 50 Pa. The particle cloud exhibited stable drifting at a constant velocity, with counteracting ions resulting in a two-stream instability that generated DAWs [7, 10].

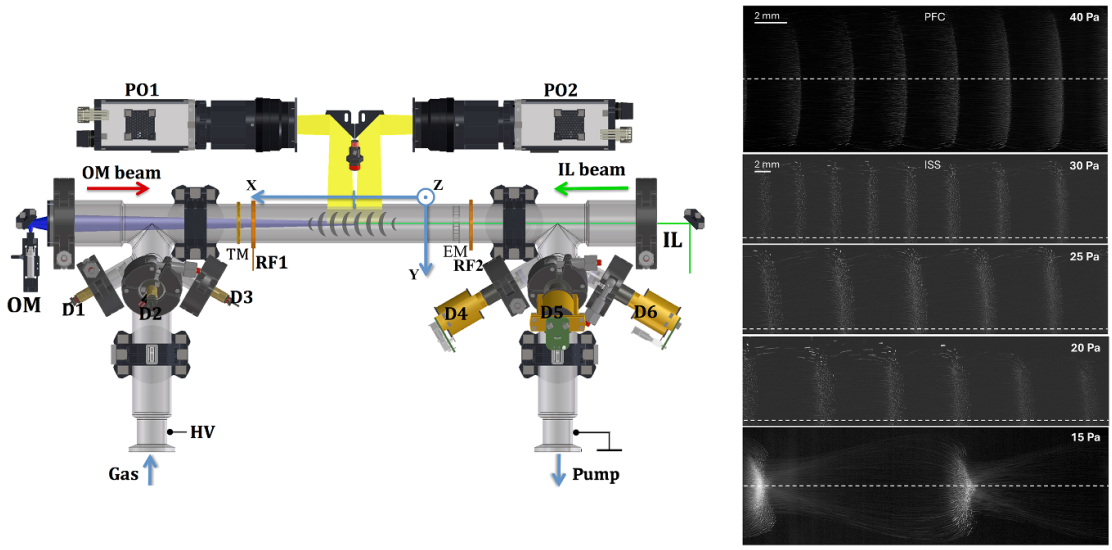

Figure 1. A schematic depiction is presented in the left panel, illustrating the experimental setup and procedure employed. © [2016] IEEE. Reprinted, with permission, from [12]. The process involved injecting a densely populated particle cloud into the chamber, which then traversed through the chamber. Key components and manipulation tools are identified, including the illumination laser (IL) and optical manipulation laser (OM). Additionally, the setup includes radio-frequency (RF) coils, electromagnetic (EM) manipulators, and thermal manipulators (TM). Particle injection is achieved using dispensers D1–D6, and the observed phenomena are captured by the particle observation cameras (PO). The right panel displays example images of self-excited Dust Acoustic Waves (DAWs) at different gas pressures, captured during the ISS and PF campaigns. In particular, high-contrast images of these waves are presented for gas pressures of 15 Pa and 40 Pa from the PF campaign, and 20 Pa to 30 Pa from the ISS campaign. A dashed line marks the center of the plasma chamber in each image.

In the ISS setup, the procedure included trapping of the particle cloud using RF-coils, providing sufficient time to experiment under microgravity conditions. The confined particle cloud expanded to the plasma sheath with enough density to excite DAWs. With this it was possible to systematically scan the particle cloud and examine the particle cloud density for every configuration, see analysis section. By controlling the current and pressure, we could adjust the impact of the plasma on the particle cloud, altering their behavior.

The experimental procedure concluded with a series of runs where the particle cloud was sent back and forth through the tube. During these runs, the effective electric field in the chamber was systematically reduced by adjusting the DC polarity switching (DC-PS) duty cycle. When an alternating electric field is applied to the complex plasma at a frequency much higher than the microparticle plasma frequency ($f_{\mathrm{pd}} =$ 10–100 z) and much lower than the ion plasma frequency (about 10 MHz) [11], the microparticles experience an averaged electric field that depends on the duty cycle of the polarity switching. This manipulation of the electric field influenced the behavior of the DAWs and provided valuable insights into the ER effects impacting the multi-particle system. The polarity switching was carried out at a frequency of 500 Hz, ensuring precise control over the microparticle dynamics and the resultant wave phenomena.

3. Theoretical methodes

In this section, we outline the theoretical framework employed for the analysis of individual particles and DAWs. We begin by detailing the particle charge potential and its behavior in large particle clouds. Subsequently, we present the force equations governing the trajectories of individual particles. A key aspect of our methodology involves describing DAWs through the dispersion relation. Finally, we address ER effects, establishing the theoretical foundation for the subsequent discussion and analysis.

3.1. Charge and charge depletion

The methodology for estimating the charge on microparticles in a complex plasma is outlined here, along with an analysis of how the Havnes Parameter influences the overall charge of multiparticle clouds in the plasma environment.

The charge of individual particles, denoted as Z_{d}, in the bulk of the discharge is estimated using the model presented in Antonova *et al* [13]. The charge formula, expressed as a function of the particle's potential, is given by:

$$Z_{\mathrm{d}} = (4\pi\varepsilon_0 k_{\mathrm{B}})\,\frac{zaT_{\mathrm{e}}}{e^2}; \qquad z = 0.3 \pm 0.1. \tag{1}$$

Here, z represents the reduced charge, which relates to the potential of a microparticle within a neon complex plasma, taking into account its radius a_p, with T_e denoting the electron temperature. This potential was experimentally estimated as indicated in equation (1) and is used as basic [13].

The Havnes parameter, denoted as P_H, plays a significant role in modifying the bulk particle charge due to interactions within a densely packed grain environment [14, 15]. It is defined as the ratio of the charge residing on the dust component to that on the electron component, calculated by the following formula:

$$P_H = \frac{4\pi\epsilon_0 a}{e}\left(k_B T_e/e\right)\left(n_d/n_i\right) \tag{2}$$

where n_d and n_i are the grain and ion number densities, respectively and k_B denotes the Boltzmann constant [14]. This parameter effectively captures the interaction effects among closely packed grains, which contribute to the quasineutrality condition, $n_i = n_e + Z_d n_d$, making the ion density larger than the electron density. This interaction increases the ratio of ion-to-electron flux, thereby reducing the absolute magnitude of the grain charge compared to an isolated grain scenario [14].

The estimation of electron and ion fluxes via the orbital motion limited (OML) approach, together with the quasineutrality condition, leads to a dimensionless representation:

$$\sqrt{\tau}\exp\left(-z\right) = \sqrt{\frac{m_e}{m_i}}\left(1+z\tau\right)\left(1+P_H\right) \tag{3}$$

where m_e and m_i are the electron and ion masses, respectively. This equation incorporates the effects of particle density and the Havnes parameter, with $\tau = T_e/T_i$, where T_i is the ion temperature, on the overall charge dynamics within the plasma, providing a comprehensive perspective on how microscale interactions influence macroscale plasma characteristics.

The application of basic OML theory involves certain limitations that warrant discussion. Specifically, this theory's limitations are partially addressed by incorporating charge modification due to closely packed dust particles, as accounted for by the Havnes parameter. However, our model omits an additional critical effect: ion collisions with neutral particles, which diminish the current flow into the microparticles, subsequently reducing the particle charge number, z [5, 16]. It is essential to emphasize that our results represent the upper boundary for particle charge, as they do not account for the potential charge reduction caused by ion-neutral collisions.

3.2. Force balance

The velocity of particles within a stable flow regime is dictated by the equilibrium of various forces acting upon them. These forces include the electric force, $F_E = -Z_d eE$, the neutral drag force, $F_n = -\delta\frac{4}{3}\pi a^2 m_n \nu_{th,n} n_n \nu_d$, and the ion drag force, $F_{id} = m_d \nu_{di}(u_i - v_d) \approx m_d \nu_{di} v_d$ [17]. Within the observed conditions, the electron drag force is significantly smaller, by almost two orders of magnitude, than the ion drag force, thus, it is neglected in our theoretical assumptions. This disparity arises due to the substantial electron-to-ion temperature ratio $\tau = T_e/T_i$ [18]. In the expressions for the neutral drag force, $\delta = 1.4$ represents a factor that characterizes the interactions between gas molecules and spherical particles, accounting for the resultant velocity distribution of particles reflected from the surface [19]. Moreover, m_n represents the mass of a neutral gas atom, $\nu_{th,n}$ denotes the thermal velocity of the neutrals, and n_n their number density. In the general description of the ion drag force, u_i denotes the ion drift velocities, and ν_{di} correspond to the effective momentum transfer frequencies for dust-ion collisions. The measured velocity of a microparticle with mass m_d and radius a is represented by v_d. Finally, the addressed forces are collected in a balance equation given by:

$$F_n + F_E + F_{id} = 0. \tag{4}$$

However, the ion drag force is complex in many ways, especially the interaction between microparticles and ions. For the momentum transfer during dust-ion collisions, we adopt an established heuristic expression suitable for our experimental parameter space [17]:

$$\delta\frac{4}{3}\pi a^2 m_n \nu_{th,n} n_n \nu_d = -Z_d eE + \left(8\sqrt{2\pi/3}\right) a^2 n_i m_i \nu_{Ti} u \cdot \Phi_\Lambda, \tag{5}$$

$$\Phi_\Lambda = \left[1 + \frac{\beta_T}{2}\frac{\lambda_D}{a} + \frac{\beta_T^2}{4}\frac{\lambda_D^2}{a^2}\Lambda\right], \tag{6}$$

where m_i is the ion mass, $v_{Ti} = \sqrt{T_\mathrm{i}/m_\mathrm{i}}$ represents the ion thermal velocity and,

$$\Lambda = 2\int_0^\infty \left[\exp(-x)\ln\left(\frac{2x+\beta_T}{2ax/\lambda_\mathrm{D}+\beta_T}\right)\right]\mathrm{d}x, \tag{7}$$

is the modified Coulomb logarithm, integrated over the Maxwellian velocity distribution function for ions, with the thermal scattering parameter $\beta_T = Ze^2/T_\mathrm{i}\lambda_\mathrm{D}$ and Debye length λ_D representing the effective screening length [18]. The ion drift velocity and the electric field are related via the ion mobility coefficient, $u = \mu E = M \cdot v_{Ti}$. The ion flow, caused by the electric field, naturally results in the momentum transfer from the ions drifting relative to the particle component. The modified Frost approximation of the mach number, M, is given by [20]:

$$M = A \cdot \left[1 + \left(B \cdot \frac{E}{N}\right)^C\right]^{-1/2C} \frac{E}{N}. \tag{8}$$

Here, E/N represents the ratio of electric field strength to the neutral gas number density, expressed in Townsend units ($1\,\mathrm{Td} = 10^{-17}\,\mathrm{V}\cdot\mathrm{cm}^2$), and coefficients $A = 0.0354\,[\mathrm{Td}^{-1}]$, $B = 0.0118\,[\mathrm{Td}^{-1}]$, and $C = 1.181\,[\mathrm{Td}^{-1}]$.

An additional adjustment is required when operating in low-pressure complex plasmas, as it affects the ion temperature, T_i. Typically, the ion temperature is assumed to be equal to that of neutral atoms, approximately 300 K. However, under low-pressure conditions, the ion temperature increases due to heating in the ambipolar diffusion field, E, resulting in a temperature corresponding to two-thirds of the mean energy of ions drifting in the electric field. Consequently, the interparticle distance increases, which directly impacts the ion temperature, as described in [21, 22]:

$$\tilde{T}_\mathrm{i} = \frac{2}{9} l_\mathrm{i} e E. \tag{9}$$

This adjustment is critical for accurately modeling the behavior of ions in low-pressure plasmas involving the ion mean free path l_i and electric field potential E.

3.3. Linear dispersion relation

The dispersion relation is a valuable tool to assess the experimental data and results for DAWs in complex plasmas, particularly in its linear form. The derivation of the dispersion relation for DAWs takes into account three charged species: electrons, ions, and dust particles, all of which are assumed to be undergoing linear motion along the x-axis. However, following the standard textbook procedure and using the quasi-neutrality condition, $n_\mathrm{i} = n_\mathrm{e} + Z_\mathrm{d} n_d$, the dispersion relation is simplified by assuming cold dust ($T_\mathrm{d} = 0$) and hot electrons ($T_\mathrm{i} << T_\mathrm{e}$) to [15],

$$\omega^2 + i\beta_\mathrm{d}\omega = \frac{\omega_\mathrm{pd}^2 k^2 \lambda_\mathrm{D,i}^2}{1 + k^2\lambda_\mathrm{D,i}^2}, \tag{10}$$

with the wave and dust plasma frequency ω, ω_pd, the dust-neutral friction coefficient β_d, the wave vector k and the ion Debye length λ_Di. At this point, we have to take a closer look at β_d, characterizing the damping rate of the linear system [15],

$$\beta_\mathrm{d} = \frac{8\cdot\delta}{\pi} \cdot \frac{p}{a\rho_\mathrm{d} v_\mathrm{th,n}}, \tag{11}$$

with the Epstein coefficient δ, pressure p and MF-density ρ_d [19]. Additionally, the neutral thermal velocity, denoted as $v_\mathrm{th,n}$ and defined by $v_\mathrm{th,n} = \sqrt{T_\mathrm{n}/m_\mathrm{n}}$, is fixed at 320 m s^{-1}, where m_n represents the neutral mass. All important quantities are given in table 1. A quantitative analysis of the interplay between the dust-friction parameter and the plasma-dust interaction frequency indicates minimal effects [15]. This result suggests a negligible impact on wave damping, as the dust friction coefficient β_d ranges from $0.52\cdot\omega_\mathrm{pd}$ to $0.13\cdot\omega_\mathrm{pd}$. A direct comparison with the measured wave frequency and its influence maybe problematic, as the actual phase frequency deviates from that relative to the background gas. However, we aim for a straightforward discussion using a linear approach. Therefore, we assume zero damping in the subsequent sections of this

paper. Additionally, taking into account small wave numbers where $k^2\lambda_{\mathrm{Di}}^2 \ll 1$, a condition met in all observed cases, the dust-acoustic phase speed C_{DAW} is determined by

$$C_{\mathrm{DAW}} = \omega_{\mathrm{pd}}\lambda_{\mathrm{Di}} = \sqrt{\frac{k_{\mathrm{B}}T_{\mathrm{i}}}{m_{\mathrm{d}}} \cdot \frac{n_{\mathrm{d}}}{n_{\mathrm{i}}} \cdot Z_{\mathrm{d}}^2}, \tag{12}$$

with the ion temperature T_{i} and the mass of a single micro-particle m_{d}.

3.4. ER effect

This section addresses the analytic aspects of the ER effects influencing the speed of micro particles and DAWs in complex plasmas. The primary focus is on the particle charge potential and the interaction dynamics shaped by the external electric field.

In a complex plasma, the effective radius of the polarizable cloud attached to a microparticle, typically defined by the ion screening length, is typically a few orders of magnitude larger than the particle size itself, $2 \cdot a/\lambda_{\mathrm{D}} \ll 1$. In the absence of an external electric field, this polarizable cloud maintains a spherical shape, known as the Debye sphere. However, upon the application of an external field, the cloud loses its symmetry and assumes a more complicated, asymmetric shape. The center of this asymmetric cloud, termed the ion wake, is displaced downstream relative to the grain along the direction of the field-induced ion drift. This leads to a nonreciprocal (non-Hamiltonian) interaction between charged grains. Such nonreciprocity arises because the wakes, which are essentially extensions of the surrounding plasma, act as a tenuous third body in the interaction dynamics. Nonreciprocity could be eliminated only if the wake potential were an even function of coordinates, i.e. $\Phi(r) = \Phi(-r)$. A method to achieve a reciprocal wake potential involves applying an AC or DC-PS field. The frequency of this field should be significantly lower than the ion plasma frequency (typically $\sim 10^7\,\mathrm{s}^{-1}$) yet substantially higher than the dust plasma frequency (typically $\sim 10^2\,\mathrm{s}^{-1}$). Under these conditions, the ions respond almost instantaneously to the alternating field, while the microparticles remain essentially unresponsive. The effective interparticle interaction is then governed by the time-averaged wake potential.

Within the framework of the linear response formalism, this interaction becomes rigorously reciprocal (Hamiltonian). Consequently, we can directly apply the principles of statistical physics to describe the dynamics of ER plasmas with $\Phi \approx \Phi_Y + \Phi_Q$, where Φ_Y represents the ideal Yukawa-Potential and:

$$\Phi_Q(r,\Theta) \simeq Z_{\mathrm{d}}\left[-\left(2-\frac{\pi}{2}\right)\cdot\frac{M^2\lambda_{\mathrm{D}}^2}{r^3}\left(3\cos^2\Theta - 1\right)\right] \tag{13}$$

represents the quadrupole term [8, 23], with relative microparticle distance r and particle charge Z_{d}. This interplay results in measurable side effects, including the formation of string-like structures composed of microparticles. Strings are defined as electrorheologically connected particles that appear in a chain-like structure. They are identified by analyzing the angle between neighboring particles at a constant distance, which determines the likelihood of string formation [24]. Evidence suggests that the likelihood of string formation between microparticles increases in the presence of ER effects [6]. Furthermore, the influence of string formation on DAWs has been quantified [7].

4. Results and analysis

In this section, we present the evaluation of the charge and collective behavior of a microparticle ensemble under varying effective electric field strengths, E_{eff}. As an initial step, table 1 provides an overview of essential physical parameters, excluding the final results. Parameters marked with a star ($\star$) were measured in the absence of microparticles using a Langmuir probe and subsequently adjusted to reflect the experimental conditions [10].

The particle number density, n_{d}, is determined using image reconstruction techniques incorporating machine learning methods [25]. In this approach, particle motion is arrested by inducing an electric field through an RF coil, which applies an alternating current (AC) field of 300 mW at a frequency of 81.36 MHz. This leads to the formation of a crystalline particle structure, characterized by a central void in the confined particle cloud. For a detailed description of the procedure, refer to section 2. The three-dimensional particle density is estimated using the Wigner–Seitz cell approximation, based on particle tracking data to determine the pair correlation function. The mean radius, r_0, is identified from the first peak of the radial distribution function, and the Wigner–Seitz radius is subsequently calculated as $a_w = r_0/\rho$, where $\rho = 1.79 \pm 0.07$ represents the assumed packing density [26]. This provides an estimate of the particle number density with a maximum uncertainty of $\pm 12\%$, assuming isotropic cloud symmetry [23, 27]. However, due to the symmetric distribution of particles induced by the RF coil, the reference particle density was determined as

Table 1. Summary of system parameters and performance metrics. Quantities marked by ($\star$) are measured in the absence of microparticles, taken from [10], while others are deduced from theoretical considerations. Detailed descriptions and applications are provided in the text.

Parameter	15 Pa	20 Pa	25 Pa	30 Pa	40 Pa
$E^\star$ [V m^{-1}]	−249	−248	−248	−247	−246
$n_\mathrm{d} \cdot 10^{11}$ [m^{-3}]	0.65	1.50	1.90	2.30	2.50
$n_\mathrm{i} \cdot 10^{14}$ [m^{-3}]	3.66	2.86	2.84	2.86	2.73
$n_\mathrm{e}^\star \cdot 10^{14}$ [m^{-3}]	0.85	0.92	0.99	1.06	1.20
$n_0 \cdot 10^{21}$ [m^{-3}]	3.75	4.99	6.24	7.49	9.99
$T_\mathrm{e}^\star$ [eV]	10.08	9.59	9.20	8.91	8.56
T_i [eV]	0.0448	0.0411	0.0388	0.0373	0.0355
$l_\mathrm{i} \cdot 10^{-4}$ [m]	2.67	2.00	1.60	1.33	1.00
λ_D [μm]	82	89	87	85	84
M	1.68	1.34	1.10	0.94	0.72
u_i [m s^{-1}]	647.5	484.7	387.0	321.9	240.5
P_H	1.80	2.17	2.13	2.08	2.14
ω_pd [1/s]	796	549	522	509	433
β_d [1/s]	98.14	130.86	163.57	196.28	261.71

$n_\mathrm{d} = 2 \cdot 10^{11}$ [m^{-3}] for all pressures. A more detailed analysis reveals stronger deviations, which will be discussed in the following sections.

The electron number density, n_e, and electron temperature, T_e, are measured in the absence of microparticles [10]. Conversely, the ion number density, n_i, and ion temperature, T_i, are inferred based on the quasineutrality condition, $n_\mathrm{i} = n_\mathrm{e} + Z_\mathrm{d} n_\mathrm{d}$, and the ion mean free path, l_i, using equation (9).

The ion mean free path is determined by the neutral gas density and calculated using the ideal gas equation: $l_\mathrm{i} = 1/(n_\mathrm{n}\sigma_\mathrm{in}) \approx T_\mathrm{n}/p\sigma_\mathrm{in}$, where $\sigma_\mathrm{in} = 10^{-18}$ m^2 represents the ion-neutral cross-section of neon plasma [18].

Other significant parameters, such as the ion velocity u_i, are derived using the Frost formula, equation (8), which relates the Mach number of the ion species to the system parameters. The ion velocity's direct proportionality to the electric field forms the basis of the analysis presented in section 4.2.

4.1. Charge

The initial findings from the measurements performed during the ISS campaign (blue) and the parabolic flight campaign (red) are presented in figure 2. We observe the expected trend of the measured data, showing a higher particle velocity, v_group, and wave phase velocity, C_DAW, at low pressure, reducing to higher pressure values within the observed range. Notably, the data collected during the PFC are slightly higher. This discrepancy may stem from procedural differences between the flight and ISS campaigns, which could influence the microparticle trajectories and their interaction with the radial electric field before reaching the FOV, leading to an increase in particle charge an effect likely more pronounced at lower pressures [22]. However, it is important to note that a direct comparison assumes equivalency in the electric field potential across both the PFC and ISS setups, which cannot be guaranteed and may also account for observed deviations.

The figures also show the theoretical prediction for each observation. The combination of the two theoretical models allows us to estimate the charge potential by solving equations (5) and (12) numerically. This also involves solving equation (3) to account for charge depletion caused by closely packed particles, as predicted by the Havnes parameter P. The Havnes parameter is plotted in the top panel and the resulting depleted charge potential z_depl in the bottom panel, on the second axis of figure 2. By fitting these models, we obtain a final charge estimation, with error estimates derived from fitting the solutions to the measured maximum combined uncertainties. This method has been established and used in various prior publications [7, 22, 26].

Table 2 provides a summary of the key findings. Figure 3, presents the final results for z (z_depleted) and compares them with findings from previous studies. For this comparison, the charge potential is plotted against a dimensionless parameter, defined as the ratio of the ion Debye length to the ion mean free path. Our results show a trend consistent with those reported in earlier publications, indicating that the model accurately describes our experimental observations. However, there is a discrepancy in the absolute values of the dimensionless charge potential z when compared to the values presented by Khrapak *et al* (2005) and Fortov *et al* (2004) [17, 28]. It should be noted, however, that both publications report errors of approximately 50% and 30%, respectively. Consequently, our results are consistent within the given uncertainties. Additionally, our results for the depleted charge potential align closely with the true values

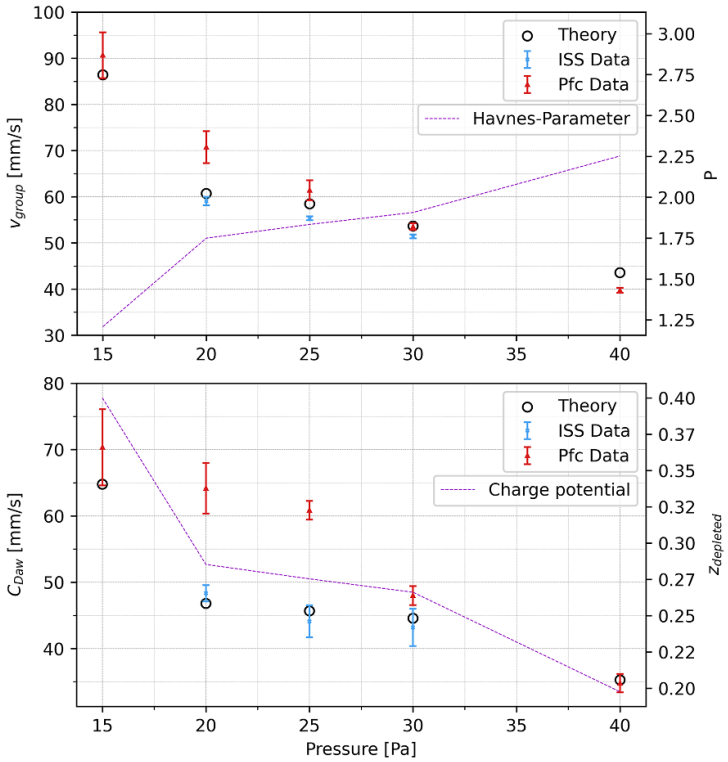

Figure 2. The figure presents the variation of group velocity v_{group} (top panel) and DAW phase velocity C_{DAW} (bottom panel) as functions of gas pressure. The data points originate from both parabolic flight (Pfc Data) and International Space Station (ISS Data) experiments, which are contrasted against theoretical predictions (denoted as 'Theory'). Additionally, the depleted charge potential z_{depleted} and the Havnes parameter P are shown to highlight the influence of large dust particle clouds on the system.

Table 2. Summary of primary performance metrics from experimental data.

Parameter	15 Pa	20 Pa	25 Pa	30 Pa	40 Pa
v_{group} $[\text{mm}\,\text{s}^{-1}]$	90.66 ± 4.98	59.06 ± 0.93	55.33 ± 0.40	51.40 ± 0.42	39.74 ± 0.53
C_{DAW} $[\text{mm}\,\text{s}^{-1}]$	70.35 ± 5.75	48.35 ± 1.24	44.11 ± 2.41	43.18 ± 2.81	34.96 ± 0.60
z	0.54 ± 0.06	0.43 ± 0.03	0.42 ± 0.02	0.41 ± 0.02	0.32 ± 0.03
z_{depl}	0.40 ± 0.06	0.29 ± 0.03	0.28 ± 0.02	0.27 ± 0.02	0.20 ± 0.03

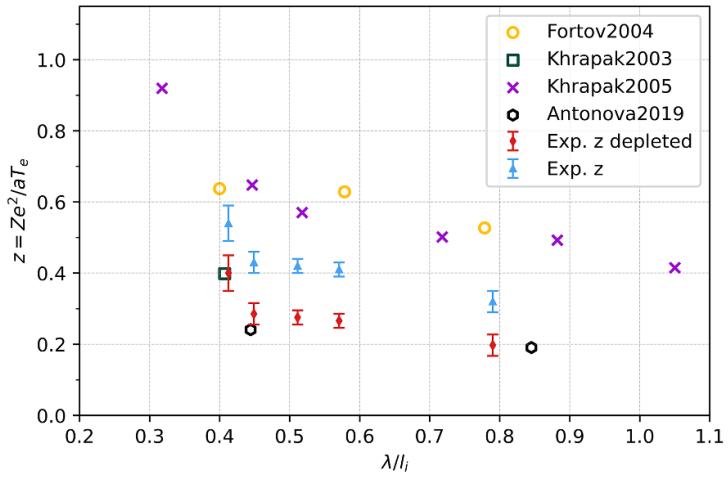

Figure 3. The charge evolution data shows variability among different studies, with experimental data points aligning with or deviating from theoretical predictions. The experimental z values, along with their reduced counterparts z_{depleted}, are illustrating these charge dynamics. The data are measured under microgravity conditions in neon with a discharge current of $I = 0.5$ mA. These results are based on multiple events, supporting significant statistical relevance.

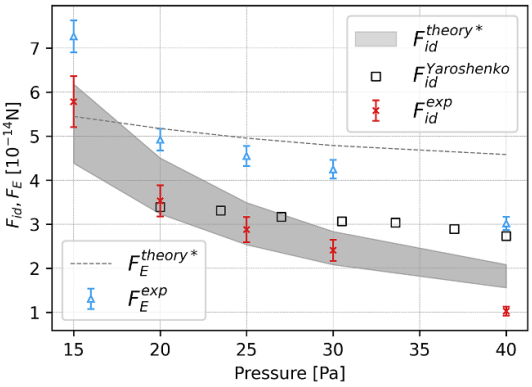

Figure 4. This figure compares the experimental findings and theoretical model predictions for the ion-drag force (F_{id}) acting on microparticles in a low-pressure plasma environment. Our experimental data are closely aligned with those published by Yaroshenko *et al* [30] and the theoretical predictions denoted as *theory**. It should be noted that the theoretical model assumes no charge depletion, highlighting its impact on the electric forces and ion-drag force.

reported by Khrapak *et al* (2003) [29] and with data from Antonova *et al* (2019) [13]. It is important to note that depletion effects were not considered in Antonova's work, likely due to the negligible particle density in those experiments.

It is important to note that the data reported herein, gathered during the ISS campaign, are derived from a comprehensive statistical database, rather than a single measurement event. The findings have been systematically and statistically analyzed across 14 experimental runs, with a total of ≈6000 frames extracted and evaluated. In contrast, the PFC data are based on a singular event for each data point measurement with ≈300 frames.

Finally, we can numerically compare the ion-drag force with previously reported results. Yaroshenko *et al* presented a method to estimate the ion-drag force without directly estimating the charge of a microparticle, using a mathematical trick involving the charge-gradient of two different microparticle sizes [30]. However, with our analytical method and improved measurements of the plasma environment through important diagnostic papers [10], we are able to make a direct comparison.

Our findings are consistent with the absolute values of the ion-drag force reported by Yaroshenko, as illustrated in figure 4. Although the previous study by Yaroshenko [30] addressed deviations in charge potential associated with reduced pressure, it did not directly account for the effects of microparticle number density and charge depletion within densely populated microparticle clouds. To highlight the importance of these factors, we compare the experimentally determined values of the ion-drag force, $F_{\mathrm{id}}^{\mathrm{exp}}$ and $F_{\mathrm{id}}^{\mathrm{Yaroshenko}}$, with theoretical predictions depicted by the light grey area and dashed line in the figure. The theoretical models, $F_{\mathrm{id}}^{\mathrm{theory}^*}$ and $F_{\mathrm{E}}^{\mathrm{theory}^*}$ assume a constant microparticle charge potential of $z^{\mathrm{theory}^*} = 0.3$ and neglect charge depletion, with a microparticle density range of $n_{\mathrm{d}}^{\mathrm{theory}^*} = 1.5 \pm 0.5 \cdot 10^{11}\,\mathrm{m}^{-3}$. The model suggests that increased particle densities enhance the ion-drag force, more pronounced at low pressure. However, they do not exert a similar influence on the electric force $F_{\mathrm{E}}^{\mathrm{theory}^*}$ in the absence of charge depletion. Our analysis reveals that lower microparticle densities are necessary when modeling at pressures below 20 Pa correctly to prevent the ion-drag force from exceeding the electric force $F_{\mathrm{E}}^{\mathrm{theory}^*}$, which would result in microparticles moving against the direction of the electric field. In consequence, the experimental data demonstrate the influence of charge depletion on the electric force, with a notable increase in deviation at lower pressures and a breakdown at higher pressure levels, affecting both $F_{\mathrm{E}}^{\mathrm{exp}}$ and $F_{\mathrm{id}}^{\mathrm{exp}}$.

To support these findings, we analyzed the absolute brightness of the images across the entire data set, where the absolute brightness is directly proportional to the particle number density n_{d}. The brightness levels during the ISS campaign were relatively constant, in contrast to those during the PFC Campaign, where absolute pixel values varied by 20% between pressures of 25–40 Pa, a variation not detectable at even lower pressures.

4.2. Electro-Rheology-Effect

In the previous section, the charge potential z of an individual particle, under the current experimental conditions, was estimated and discussed. This serves as the foundation for the subsequent analysis of the measured data. As previously described, the experimental procedure involves modulating the effective electric field by periodically switching the system's polarity with a defined duty cycle. This modulation introduces an additional phenomenon termed the electro-rheology effect where micro-particle plasma

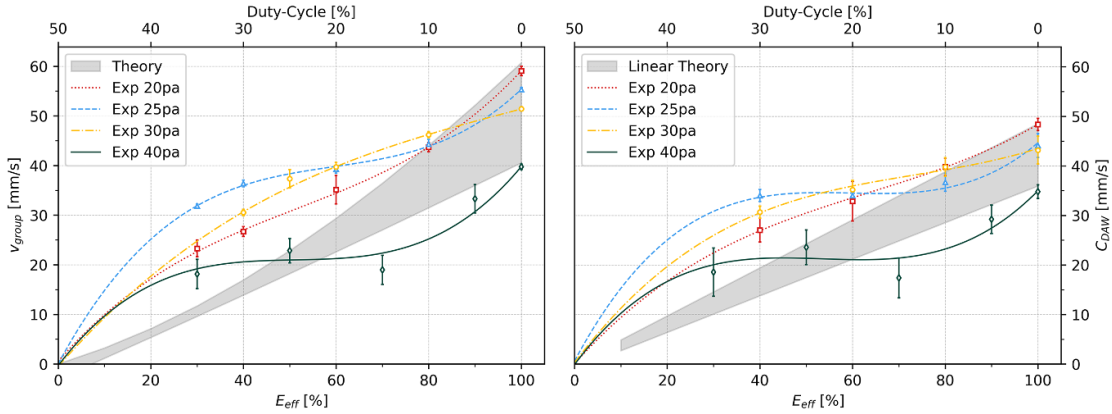

Figure 5. This figure shows the impact of the electrorheological effect on particle charge potential under varying electric field conditions. The experimental data from different pressures is fitted against a theoretical model, revealing deviations that suggest additional forces or interactions not accounted for by the model, with significant influence on DAW phase velocity.

interactions are altered. This effect modifies the potential of individual particles, influencing their interaction with both the electric field and the surrounding plasma.

This relationship is illustrated in figure 5, where the experimental data are presented in distinct colors corresponding to different pressures. A fitted curve is included to facilitate comparison with the theory, represented by the light grey region. The theory is derived from the numerical solution of the force equation (5) under the assumption of the estimated charge. The reduction of the effective electric field due to polarity switching, is modeled by adjusting the electric force (F_{E}) and the ion velocity distribution (u_{i}), calculated using the Frost formula, equation (8), contributing to the ion-drag force (F_{id}). The observed deviation of the experimental data from the theoretical prediction indicates a force or potential not accounted by the model. Notably, this deviation is also reflected in the measured DAW speeds, as these waves are determined by the Doppler shift of the collective particle cloud speed. Interestingly, the DAW velocity resembles a decelerated form of the group velocity.

To further elucidate the missing potential interaction and the differing responses of complex plasmas to DC-PS and DC fields, it is essential to consider the role of the particle potential. This potential can be modeled using a polynomial expansion that accounts for subthermal ion drift, with Mach number $M \lesssim 1$. A commonly used solution is given by equation (13). In this model, we focus on the quadrupole term, as this effect is specifically induced by the alternating current field. To estimate the behavior of the charge potential as a function of the duty cycle of the applied DC-PS field, we use the following model:

$$f_Q(x) = c_0 \cdot \left(2 - \frac{\pi}{2}\right) \cdot \left(3 \cdot \left(ax^3 + bx^2 + cx + d\right) - 1\right). \tag{14}$$

This function reconstructs the quadrupole term as defined by equation (13), with the input parameter x, representing the duty cycle applied. Using this model, the force balance equation (4) was solved by adjusting the particle charge according to the relationship $Z_{\mathrm{d}}^{\mathrm{new}} = Z_{\mathrm{d}} - Z_{\mathrm{d}} \cdot f_Q$. The final results are represented by the polynomial $p(x) = (ax^3 + bx^2 + cx + d)$, which approximates $\cos^2\Theta$, as illustrated in the right panel of figure 6. Here, the polynomial $p(x)$ demonstrates how the quadrupole influences the charge potential depending on the duty cycle [6, 31]. The outcomes of this adjustment, which reveal how the particle group velocity v_{group} responds to the duty cycle or variations of the effective electric field E_{eff}, are displayed in the left panel of figure 6. The plotted lines represent the updated model predictions, with constants a, b, c, and d determined through regression optimization methods. The experimental data was targeted, and the optimization was constrained to a maximum of 1000 steps to ensure computational efficiency. The scaling factor $c_0 \cdot \left(2 - \frac{\pi}{2}\right)$ is included to account for specific quadrupole influences.

A significant improvement in the model's predictive accuracy is observed in the left-hand panel, particularly between 20% and 60% of the effective electric field. This improvement showcases the interplay of the quadrupole effect, with the surounding plasma. Generally we find the predicted reduction of the potential, resulting in an increase of the micro particle speed v_{group}. Notable similarities are observed in the trend of our model compared to those reported by Kana *et al* [31].

Figure 6 further demonstrates how the DC-PS mode affects the particle charge potential, influencing the likelihood of particle string formation. We observe a reduction in the potential across a wide range of effective electric fields, consistent with the expected quadratic dependence of the quadrupole potential on the thermal Mach number, $\Phi_Q \propto M^2$.

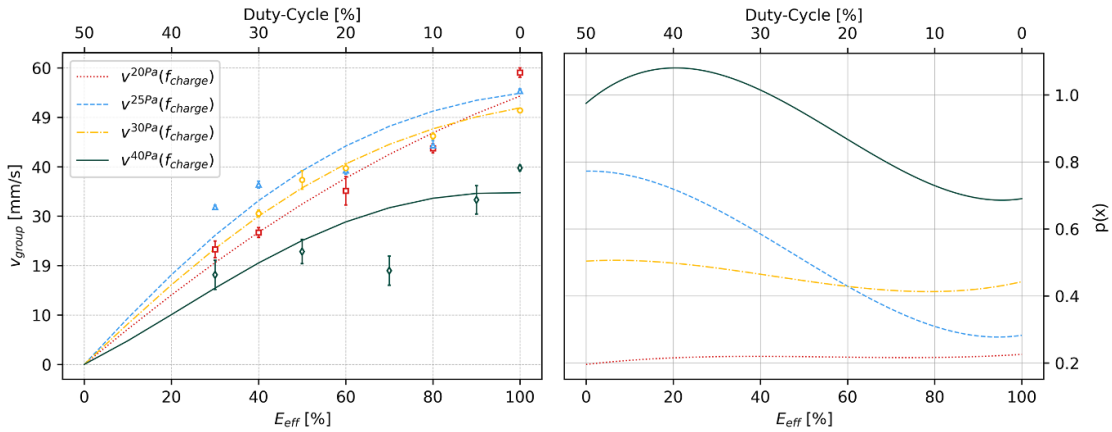

Figure 6. This figure illustrates the effects of direct current polarity switching (DC-PS) fields on particle dynamics and interactions, which lead to changes in the dust drift velocity, v_{group}, shown in the left panel, and alterations in individual particle charge through the function f_Q. The right panel displays the polynomial $p(x)$ of the model, which adjusts theoretical predictions to align with experimental data points. It represents the probability of interaction between neighboring particles, serving as a measure of electrorheological interactions [31].

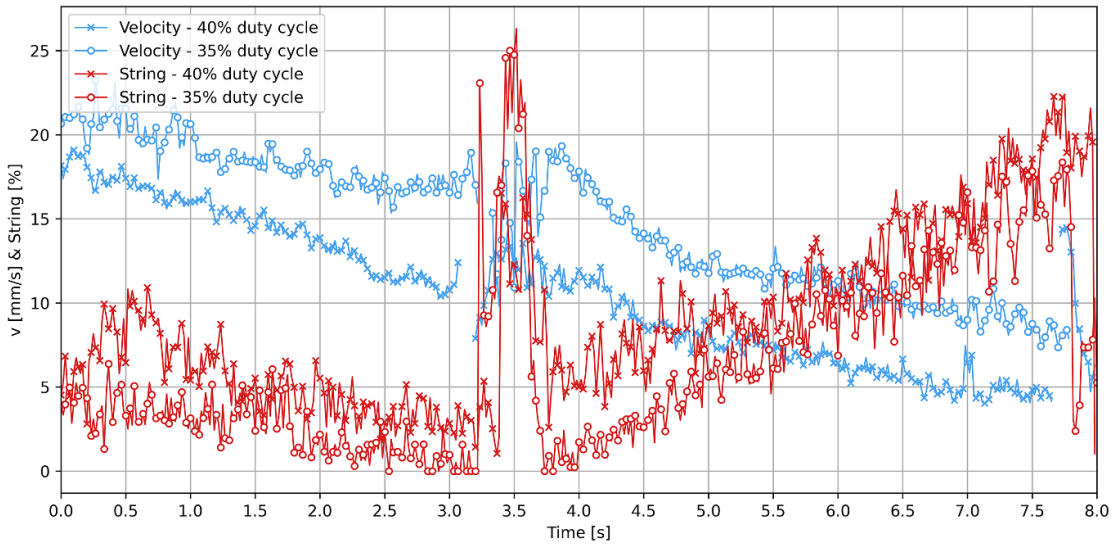

Figure 7. Velocity and string formation as a function of image number under two different duty cycles (40% and 35%) at 20 Pascal. The blue curves represent the velocity (in mm s^{-1}), while the red curves indicate the string formation percentage measured [24]. Crosses denote the 40% duty cycle, and circles indicate the 35% duty cycle for both velocity and string formation.

4.3. String formation

Polarity switching modulates the charge potential, affecting the interactions between microparticles and their surrounding environment. This modulation increases the likelihood of string formation, as reported in previous studies [8, 23], while also influencing the interaction with counteracting ions. Figure 7 illustrates a unique phenomenon observed during the ISS campaign, where a drifting microparticle cloud was exposed to a low effective electric field, revealing the impact of string formation on individual particle velocities and potentials. The observations were conducted at a pressure of 20 Pa, with two distinct duty cycles of 40% and 35%, corresponding to effective electric fields of 20% and 30%, respectively. The images were analyzed using a specialized code for particle tracing and string detection, enhanced by machine learning methods [24, 32].

An amplification in the signal is observed in the central region of the graph, corresponding to the polarity reversal of the electric field. This reversal not only induced a change in the direction of microparticle motion but also altered the charge distribution of the surrounding individual microparticles. Following the polarity switch, a distinct onset of string formation was observed, serving as a seed for crystal growth. In consequence, a notable increase in string formation was observed alongside a reduction in particle velocity, likely triggered by the reversal of the electric field potential.

During the ISS campaign, we observed a consistent discrepancy between the measured microparticle velocity and the wave phase speed, which showed an approximate increase of +15% at 20 Pa across different

polarities. This difference is most likely attributable to variations in electric field strength ($dE^{\pm} \sim 5\%$). Based on this observation, we expected an increase in measured velocity after the polarity switch. However, this was followed by a notable reduction in microparticle velocity, v. This reduction suggests that the additional energy added to the charge potential, which exceeded the interaction distance of the particles, likely facilitated the formation of strings. This formation disrupted the usual behavior of the particles, resulting in a decrease in their velocity [7, 33].

The phenomenon described involves the coupling of microparticles, indicating a transition from a liquid-like to a solid-like state in complex plasma. A comparison of the interaction radius of a microparticle, λ_D, with the interparticle distance, $(\Delta = n_d^{-1/3})$, reveals that the potential extends due to the higher electric field, such that $(2 \cdot \lambda_D/\Delta \to 1)$. The particle density was measured as constant throughout the entire data set, with $(n_d = 2 \pm 0.1 \cdot 10^{11}\,\mathrm{m}^{-3})$, using image reconstruction techniques [24]. The system then progressively consumes energy during string formation, ultimately leading to a chaotic state, characterized by the excitation of DAWs at the boundary region.

The presence of strings is expected to not only reduce the microparticle speed but also influence the phase velocity of the excited DAWs [7]. Quantitative analysis indicates that $C_{DAW}(40\%\,duty\,cycle) = 17.0 \pm 1.5\,\mathrm{mm\,s}^{-1}$, which aligns with predictions for a pressure of 20 Pa, as shown in the left panel of figure 6 and assuming a negligible Doppler shift at low effective electric field strengths. Although the electric field strength increases following the polarity switch, this does not significantly alter the DAW phase velocity, C_{DAW}. However, given the low effective Mach number, $M_{eff} = 0.3$, a slight reduction in C_{DAW} is acceptable. It is probable that the increased electric field and ER effects counteract each other, leading to the observed outcome. For the first time, a phase transition was observed in a particle cloud moving at a constant velocity, demonstrating a measurable ER effect that induced string formation.

5. Conclusion

The experimental results demonstrate that particle charge and ER effects are critical factors influencing the dynamics of microparticles in low-pressure complex plasmas under microgravity conditions. First, the charge potential, $z = 0.34 \pm 0.17$, was experimentally estimated and compared with values reported in previous studies, revealing discrepancies due to electron depletion in systems with high microparticle populations. Additionally, an increase in the charge potential to $z = 0.54 \pm 0.12$ was observed at pressures below $p \lesssim 15\,Pa$. Furthermore, we identified qualitative evidence that the potential of a microparticle is perturbed and reduced under reduced duty cycle and DC-discharge plasma conditions.

Our findings further contribute to understanding the influence of external electric fields and particle interactions on plasma wave propagation. We directly observed stepwise string formation within a particle cloud moving at a constant velocity, which affects and decelerates the multiparticle system.

Data availability statement

The data that support the findings of this study will be openly available following an embargo at the following URL/DOI: https://github.com/luki58/PFC42.

Acknowledgments

This work was supported by DLR under Grant Nos. 50WM2044 and 50WK2270B.

The work in scope of this paper of A V Z, A M L, A D U and O F P was also supported by the Ministry of Science and Higher Education of the Russian Federation (State Assignment No. 075-00269-25-00).

All authors greatly acknowledge the joint ESA-Roscosmos 'Experiment Plasmakristall-4' onboard the ISS. We also express our gratitude to Mikhail Pustylnik and Hubertus Thomas from DLR for their support, as well as to CAMDMOS for their assistance during the ISS campaigns.

ORCID iDs

L Wimmer https://orcid.org/0009-0008-8970-8203
M Klein https://orcid.org/0009-0009-9596-7671
A M Lipaev https://orcid.org/0000-0002-2559-3696

References

[1] Zohm H 2012 Plasmaphysik *Technical Report* (Ludwig-Maximilian-University Munich) (available at: www.ipp.mpg.de/2155286/Plasmaphysik)
[2] Merlino R 2009 Dust-acoustic waves driven by an ion-dust streaming instability in laboratory discharge dusty plasma experiments *Phys. Plasmas* **16** 124501
[3] Schwabe M *et al* 2008 Nonlinear waves externally excited in a complex plasma under microgravity conditions *New J. Phys.* **10** 033037
[4] Merlino R L 2014 25 years of dust acoustic waves *J. Plasma Phys.* **80** 773–86
[5] Fortov V E, Khrapak A G, Khrapak S A, Molotkov V I, Nefedov A P, Petrov O F and Torchinsky V M 2000 Mechanism of dust-acoustic instability in a direct current glow discharge plasma *Phys. Plasmas* **7** 1374–80
[6] Dietz C, Budak J, Kamprich T, Kretschmer M and Thoma M H 2021 Phase transition in electrorheological plasmas *Contrib. Plasma Phys.* **61** e202100079
[7] Schwabe M *et al* 2020 Slowing of acoustic waves in electrorheological and string-fluid complex plasmas *New J. Phys.* **22** 083079
[8] Ivlev A V, Thoma M H, Räth C, Joyce G and Morfill G E 2011 Complex plasmas in external fields: the role of non-hamiltonian interactions *Phys. Rev. Lett.* **106** 155001
[9] Dietz C, Kretschmer M, Steinmüller B and Thoma M 2018 Recent microgravity experiments with complex direct current plasmas *Contrib. Plasma Phys.* **58** 21–29
[10] Pustylnik M Y *et al* 2016 Plasmakristall-4: new complex (dusty) plasma laboratory on board the International Space Station *Rev. Sci. Instrum.* **87** 093505
[11] Thoma M H *et al* 2010 Recent complex plasma experiments in a dc discharge *IEEE Trans. Plasma Sci.* **38** 857–60
[12] Kretschmer M, Antonova T, Zhdanov S and Thoma M 2015 Wave phenomena in a stratified complex plasma *IEEE Trans. Plasma Sci.* **44** 458–62
[13] Antonova T, Khrapak S A, Pustylnik M Y, Rubin-Zuzic M, Thomas H M, Lipaev A M, Usachev A D, Molotkov V I and Thoma M H 2019 Particle charge in PK-4 dc discharge from ground-based and microgravity experiments *Phys. Plasmas* **26** 113703
[14] Fortov V, Ivlev A, Khrapak S, Khrapak A and Morfill G 2005 Complex (dusty) plasmas: current status, open issues, perspectives *Phys. Rep.* **421** 1–103
[15] Melzer A 2019 *Physics of Dusty Plasmas* (Springer Cham)
[16] Zobnin A V, Usachev A D, Petrov O F and Fortov V E 2008 Ion current on a small spherical attractive probe in a weakly ionized plasma with ion-neutral collisions (kinetic approach) *Phys. Plasmas* **15** 043705
[17] Khrapak S A *et al* 2005 Particle charge in the bulk of gas discharges *Phys. Rev.* E **72** 016406
[18] Khrapak S A, Ivlev A V, Morfill G E and Thomas H M 2002 Ion drag force in complex plasmas *Phys. Rev.* E **66** 046414
[19] Liu B, Goree J, Nosenko V and Boufendi L 2002 Radiation pressure and gas drag forces on a melamine-formaldehyde microsphere in a dusty plasma *Phys. Plasmas* **10** 9–20
[20] Khrapak S A and Khrapak A G 2019 Modified Frost formula for the mobilities of positive ions in their parent gases *AIP Adv.* **9** 095008
[21] Fortov V E, Usachev A D, Zobnin A V, Molotkov V I and Petrov O F 2003 Dust-acoustic wave instability at the diffuse edge of radio frequency inductive low-pressure gas discharge plasma *Phys. Plasmas* **10** 1199–208
[22] Wimmer L, Schmitz A S, Kretschmer M and Thoma M H 2024 Tilted dust-acoustic waves in low-pressure DC complex plasma *Phys. Plasmas* **31** 043702
[23] Mitic S *et al* 2021 Long-term evolution of the three-dimensional structure of string-fluid complex plasmas in the pk-4 experiment *Phys. Rev.* E **103** 063212
[24] Klein M, Dormagen N, Dietz C, Thoma M and Schwarz M 2024 Enhancing particle string detection in electrorheological plasmas using asymmetrical kernel convolutional networks *Mach. Learn.: Sci. Technol.* **5** 025050
[25] Dormagen N, Klein M, Schmitz A S, Thoma M and Schwarz M 2024 Multi-particle tracking in complex plasmas using a simplified and compact u-net *J. Imaging* **10** 40
[26] Nosenko V *et al* 2020 Shear flow in a three-dimensional complex plasma in microgravity conditions *Phys. Rev. Res.* **2** 033404
[27] Liu B, Goree J and Suranga Ruhunusiri W D 2015 Characterization of three-dimensional structure using images *Rev. Sci. Instrum.* **86** 033703
[28] Fortov V E, Petrov O F, Usachev A D and Zobnin A V 2004 Micron-sized particle-charge measurements in an inductive rf gas-discharge plasma using gravity-driven probe grains *Phys. Rev.* E **70** 046415
[29] Khrapak S *et al* 2003 Compressional waves in complex (dusty) plasmas under microgravity conditions *Phys. Plasmas* **10** 1–4
[30] Yaroshenko V *et al* 2005 Determination of the ion-drag force in a complex plasma *Phys. Plasmas* **12** 093503
[31] Kana D, Dietz C and Thoma M H 2020 Simulation of electrorheological plasmas with superthermal ion drift *Phys. Plasmas* **27** 103703
[32] Klein M, Dormagen N, Schmitz A S, Thoma M H and Schwarz M 2023 Machine learning approach for particle matching, tracing and velocimetry with self-organizing map: application to complex plasmas *2023 Int. Conf. on Machine Learning and Applications (ICMLA)* (IEEE) pp 839–44
[33] Rosenberg M 2015 Waves in a 1d electrorheological dusty plasma lattice *J. Plasma Phys.* **81** 905810407

Chapter 4

Submitted Manuscript: Investigation of the ion-drag force in low pressure complex plasma

Contributions of the Individual Co-Authors:

L. Wimmer:
Development of the experimental procedure
Data collection
Primary Software development and data acquisition
Methodology and analysis
Data visualization
Writing – original draft and revisions (ongoing)

N. Dormagen and M. Klein:
Software development
Data collection
Review and editing

S. Beppler and T.A. Zeller:
Support software development and data acquisition

M. Kretschmer, A. M. Lipaev, M. Schwarz, A.D. Usachev, O.F. Petrov:
Supporting developement of the experimental procedure and Data collection
Review and editing

M. H. Thoma:
Supervision
Data collection
Review and editing

Investigation of charge and ion drag force dynamics in complex plasma experiments with neon and argon under microgravity

L. Wimmer[1], S. Beppler[1], N. Dormagen[1,2], M. Klein[1,2], M. Kretschmer[1,2], A. M. Lipaev[3], M. Schwarz[2], A. D. Usachev[3], O. F. Petrov[3], T.A. Zeller[1], A. V. Zobnin[3], M. H. Thoma[1]

[1] Institute of Experimental Physics I, Justus-Liebig University, 35392 Gießen, Germany

[2] NanoP, THM University of Applied Sciences, D 35390 Giessen, Germany

[3] Joint Institute for High Temperatures, Russian Academy of Sciences, 125412 Moscow, Russia

E-mail: lukas.wimmer@epx1.physik.uni-giessen.de

March 2025

Abstract. In complex dusty plasmas, micron-sized particles immersed in ionized gas acquire a significant negative charge and experience various forces. One of the primary forces acting on these particles is the ion drag force. The PK-4 facility aboard the International Space Station enables precise studies of such systems under microgravity. During campaigns #17 and #18, we investigated the ion drag force on 3.4 μm melamine-formaldehyde microparticles in argon and neon plasmas across a pressure range of 10–120 Pa. We combined experimental data with advanced machine learning techniques and ion drag force modeling. This allowed us to evaluate and improve theoretical models, including an analytical approach for weak and intermediate ion coupling, as well as a hybrid model that incorporates kinetic simulations. Our results reveal a pronounced enhancement of the ion drag force measured at low pressures (below 30 Pa), especially in neon, where ion collisions and drift velocities significantly affect particle dynamics. These findings emphasize the role of ion-neutral collisions and plasma composition in determining dust-plasma interactions, offering new insight into the limitations of existing theoretical models and the need for gas-specific model refinements.

1. Introduction

Plasma, often referred to as the fourth fundamental state of matter, is characterized by its high electrical conductivity and collective behavior arising from the presence of free-moving charged particles. It forms when neutral gas molecules undergo ionization due to high temperatures, electrical discharges, or other ionizing energy sources, resulting in a system comprising electrons, ions, and neutral particles. The ionized nature of plasma fundamentally differentiates it from the classical states of matter: solid,

liquid, and gas. Plasma plays a crucial role in numerous technological applications, including semiconductor processing, environmental monitoring, medical technology, and controlled nuclear fusion. Notably, plasma constitutes approximately 99% of the observable universe, underscoring its significance in both terrestrial and astrophysical contexts [1].

When micron-sized dust particles are introduced into plasma, they become negatively charged due to electron attachment, forming a system known as dusty or complex plasma. These systems exhibit collective behaviors governed by Coulomb interactions and ion flows. The Plasma Kristall 4 (PK-4) experiment represents the latest in a series of microgravity plasma crystal investigations. It is designed to study fundamental processes at the microscopic level and makes it possible to observe particle dynamics under stable drift conditions in a uniform plasma, allowing for detailed trajectory analysis.

One of the principal forces influencing the motion of dust particles in complex plasmas is the ion drag force. This force originates from the interaction between counter-streaming ions and negatively charged microparticles, driven by the discharge's longitudinal electric field. The resulting ion flow makes use of a directional force that is partially counteracted by the electrostatic interaction with the dust particles. Since the early stages of complex plasma research, this force has been recognized as a key factor influencing particle transport and structure formation. The theoretical description of the ion drag force was initially developed by Barnes and later refined by Hutchinson and Khrapak. However, significant discrepancies between theoretical predictions and experimental observations have highlighted the limitations of these models. For instance, the formation of voids in radio-frequency (RF) complex plasmas is poorly explained by existing theoretical frameworks [2].

To address the complexities of dust-ion interactions, Khrapak proposed an alternative analytical approach, shifting the focus towards accurately characterizing the interaction cross-section. Rather than seeking a universal solution, this method classifies interactions based on dominant physical mechanisms and provides corresponding descriptions for different regimes [3].

In 2013, Graves and Schwabe introduced a hybrid approach that combines elements of Hutchinson's and Khrapak's theories with results from particle-in-cell (PIC) and Monte Carlo simulations. This model has demonstrated improved predictions, particularly in RF discharges, sheath regions, and multi-particle phenomena observed in plasma crystal experiments [4].

Beyond measuring the ion drag force, this study we aim to evaluate the predictive accuracy of existing theoretical models by comparing them with experimental results obtained from the PK-4 setup. For this purpose, data analysis and the determination of key plasma parameters are optimized using machine learning algorithms. The findings will contribute to refining theoretical descriptions of dust-ion interactions in complex plasmas and improving our understanding of plasma dynamics.

2. Experimental Setup and Procedure

The experimental investigation began with the confinement of a microparticle cloud within one section of a Π-shaped glass tube using a movable radio-frequency coil (RF1), as illustrated in Figure 1. The tube, characterized by an inner diameter of $2R = 3\,\mathrm{cm}$, was filled with either neon or argon gas at pressures ranging from $p = 10 - 120\,\mathrm{Pa}$. A direct current (DC) discharge was established within the 86 cm-long tube by applying discharge currents of $I_{DC} = 1.0\,\mathrm{mA}$ and $1.5\,\mathrm{mA}$, thereby creating a plasma environment enabling the study of ion drag force. The micro particles were illuminated using an incident green laser system (IL beam), and the microparticle dynamics were recorded using digital imaging systems [5].

The microparticles utilized in this study consisted of melamine-formaldehyde (MF) with a diameter of $2a_p = 3.4\,\mu\mathrm{m}$, a density of $\rho_d = 1.5\,\mathrm{g/cm^3}$, and a mass of $m_d = 3.24 \times 10^{-11}\,\mathrm{g}$. These particles acquired an approximate charge of $1500 - 5000\,\mathrm{e}$ through electron and ion collection from the plasma. A longitudinal electric field of approximately $2-5\,\mathrm{V/cm}$ in the positive column of the discharge facilitated the directed drift of the particles through the plasma chamber [5]. Parameters, such as the actual electric field strength E (V/m), electron number density n_e, and electron temperature T_e, have been precisely measured in the PK-4 neon configuration but remain incompletely characterized in argon. Significant diagnostic work by Pustilnik and Zobnin [5, 6] has provided key plasma parameters for neon within the parameter space of interest in this study. These parameters were obtained using Langmuir probe diagnostics in the PK-4 setup, increasing the accuracy of analytical findings. In contrast, for argon, the available data are less accurate and incomplete for the parameter space relevant to our study [7]. However, these measurements were conducted only within a limited pressure range of $p = 20$–$60\,Pa$, which does not cover the full range of interest. Additionally, no measurements exist for a discharge current of $1.5\,mA$. To address the absence of experimental data for argon, we employed mathematical inter- and extrapolation techniques to estimate plasma parameters while ensuring physical plausibility. This was achieved by incorporating the measured data points obtained via Langmuir probe diagnostics to guide the inter- and extrapolation process. The results are presented in Section 4.2.

The experimental studies were conducted as part of the 17th and 18th International Space Station (ISS) campaigns, employing two particle observation (PO) cameras, PO1 (Camera 1) and PO2 (Camera 2). Both cameras were capable of full-field-of-view (FOV) recording, covering an area of $22.7 \times 17.0\,\mathrm{mm^2}$ with a resolution of $14.2\,\mu\mathrm{m}$. To optimize data acquisition, PO1 operated with a reduced FOV of $22.7 \times 3.8\,\mathrm{mm^2}$, thereby minimizing readout time and achieving a maximum frame rate of 100 frames per second (fps). PO2 recorded with an FOV of $22.7 \times 10.9\,\mathrm{mm^2}$ reaching a frame rate of 50 fps.

During the experimental runs, the suspended particles exhibited bidirectional drift along the tube, induced by periodic polarity switching of the electric field at a frequency

of 0.25–0.5 Hz. This procedure was repeated under varying experimental conditions. A minor but significant discharge anomaly was detected during the campaign, which was observed to influence microparticle velocity. This anomaly was linked to variations in the longitudinal electric field strength and electron temperature, with noticeable deviations observed for different field polarities. Additionally, particle trajectories exhibited a slight off-axis displacement across all experimental runs, as shown in Figure 1, which was attributed to a weak thermal gradient induced by the heat of the experimental base plate.

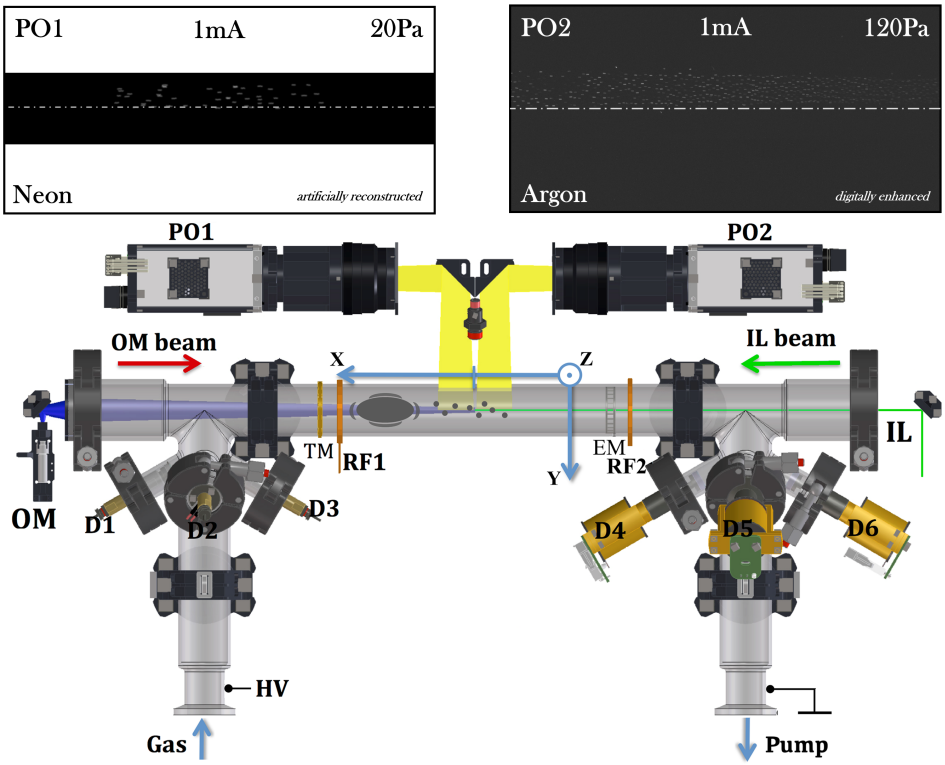

Figure 1: A schematic representation of the experimental setup and procedure is shown in the lower panel, adapted from [8]. The experiment involved injecting microparticles that drift bidirectionally along the tube, with the procedure repeated under varying parameters. Key components and manipulation mechanisms are labeled, including the illumination laser (IL) and optical manipulation laser (OM). The setup further incorporates radio-frequency (RF) coils, electromagnetic (EM) manipulator, and thermal manipulator (TM). Microparticle injection was facilitated through dispensers D1–D6, while particle dynamics were recorded using particle observation cameras (PO). The upper panel presents example images capturing microparticles at high speed and high frame rate in a neon plasma environment, highlighted with images obtained under high-pressure argon plasma conditions.

Image data acquired during the experiments were processed using a machine

learning algorithm developed by Dormagen et al. [9], enabling the extraction of microparticle velocities. This analysis provided a comprehensive investigation of microparticle dynamics by tracking particle coordinates over multiple frames under varying discharge conditions and electric field configurations.

The primary limiting factors were the brightness of the scattered light and the signal-to-noise ratio. High-speed microparticles required capture by a high-speed camera to prevent drift line overlay. An example image is shown in Figure 1 (top-left panel), which was necessarily artificially reconstructed, as no first-order enhancement produces a visually useful image for the naked eye.

3. Theoretical Framework

3.1. Force balance

The analysis strategy aims to solve the force equation governing the system. The primary driving force is the electric field force, counteracted by both the neutral drag force and the ion drag force, expressed as:

$$F_E = F_{id} + F_n, \tag{1}$$

where F_E denotes the electric force, F_{id} represents the ion drag force, and F_n corresponds to the neutral drag force.

The electric force follows the classical formulation $F_E = Z_d e E_0$, while the neutral drag force is given by:

$$F_n = v_d \delta_{epstein} \frac{4}{3} \pi a_p^2 m_n v_{tn} \left(\frac{p}{T_n k_B} \right), \tag{2}$$

with v_d being the microparticle velocity, the neutral thermal velocity v_{tn} for the plasma at room temperatur from $T_n = 300K$. Furthermore the Epstein damping rate is given by $\delta_{epstein} = 1.44$ for both neon and argon [10]. The neutral mass is m_n, and k_B denotes the Boltzmann constant. The ion drag force, F_{id}, is of particular interest due to the inherent complexity of ion-dust interactions, which poses significant challenges in deriving a general analytical solution. To refine our understanding of ion drag phenomena in plasma environments, we incorporate an analytical approach proposed by Khrapak [3], focused on the expression of the interaction cross section between microparticles and ions. Furthermore a hybrid model combining first-principles derivations with analytic results and findings from particle-in-cell (PIC) and Monte Carlo simulations [4] is used. Finally, we compare the results with the most recent theoretical framework derived from first principles by Hutchinson and Khrapak [11]. The integration of these models enhances the accuracy and predictive capability of our analysis, providing a more comprehensive description of ion drag effects in complex plasmas. The individual theories on ion drag are described in subsection 3.3 in more detail.

3.2. Charge and charge depletion

The charge of a microparticle, denoted as Z_d, is a fundamental parameter in complex plasma studies. However, its precise determination remains challenging due to multiple influencing factors. The Orbital Motion Limited (OML) theory provides a useful first-order approximation of the charge state, yet it is inherently limited. Notably, OML theory assumes a collisionless environment and does not account for charge modifications arising from interparticle interactions or plasma-mediated effects in dense microparticle suspensions [12].

Numerous studies have experimentally investigated microparticle charging mechanisms [7, 13]. These investigations demonstrate that microparticle charge potential is significantly influenced by collisional effects, and the particle charge can be expressed as:

$$Z_d = (4\pi\varepsilon_0 k_B)\frac{z a_p T_e}{e^2} \tag{3}$$

where z is the reduced charge potential, characterizing the electrostatic potential of a microparticle in a neon or argon plasma, ε_0 is the vacuum permittivity, T_e is the electron temperature, and e denotes the elementary charge. Experimental measurements indicate that the reduced charge potential assumes values of 0.3 ± 0.1 in neon plasma and 0.4 ± 0.1 in argon plasma [7]. These values serve as reference parameters for charge estimations based on Equation 3.

The impact of collective interactions in a dense dust environment is characterized by the Havnes parameter, P_H, which modifies the plasma quasineutrality condition, expressed as $n_i = n_e + Z_d n_d$. In such a regime, the ion number density, n_i, surpasses the electron number density, n_e, increasing the ion-to-electron flux ratio and consequently reducing the absolute charge of individual microparticles relative to their isolated counterparts [12]. The Havnes parameter is defined as:

$$P_H = \frac{4\pi\epsilon_0 a_p}{e}(k_B T_e/e)(n_d/n_i) \tag{4}$$

The effects of P_H on charge estimation are incorporated via the electron and ion fluxes, determined using the OML approach alongside the quasineutrality condition, yielding the dimensionless relation [12]:

$$\sqrt{\tau}\exp(-z) = \sqrt{\frac{m_e}{m_i}}(1 + z\tau)(1 + P_H) \tag{5}$$

where m_e and m_i denote the masses of electrons and ions, respectively, and $\tau = T_e/T_i$ is the electron-to-ion temperature ratio. This equation provides a comprehensive framework for analyzing the interplay between particle density, the Havnes parameter, and charge dynamics in a plasma environment.

Moreover, at low plasma pressures, ion heating significantly affects charge dynamics. The ion mean free path, governed by neutral gas density, is estimated using the ideal gas equation:

$$l_i = \frac{1}{n_n \sigma_{in}} \approx \frac{T_n}{p\sigma_{in}}, \tag{6}$$

where n_n is the neutral number density and σ_{in} represents the ion-neutral collision cross-section, with values of $\sigma_{in}^{Ne} = 10^{-18}\,m^2$ and $\sigma_{in}^{Ar} = 2.3 \times 10^{-18}\,m^2$ [14]. Under reduced pressure conditions, as considered in this study, the ion mean free path approaches or exceeds the system scale, leading to significant ion temperature variations. These variations, in turn, affect charge dynamics according to:

$$\tilde{T}_i = \frac{2}{9} l_i e E_0 \tag{7}$$

where E_0 is the discharge electric field. The total ion temperature is then given by, $T_i = \tilde{T}_i + T_{i,room}$, with the ion room temperature given by $0.025eV$.

3.3. Ion drag force

The ion drag force arises from the interaction between ions and dust particles. This interaction mechanism can be broadly categorized into two components: (i) Coulomb scattering, which is governed by long-range electrostatic interactions, and (ii) direct ion collection, where ions collide with and are absorbed by the microparticles. While the ion drag force due to direct ion collection can be described straightforwardly, a comprehensive first-principles derivation of the force resulting from field interactions remains unsolved, lacking a general theoretical framework [15].

To address this, an analytical approach has been proposed, incorporating the thermal scattering parameter introduced by Khrapak et al. [3]

$$\beta_T = \frac{\rho_0}{\lambda_{Di}} \tag{8}$$

This parameter quantifies the relationship between the Coulomb radius, $\rho_0 = Z_d e^2 / 2\pi\epsilon_0 m_i v_{ti}^2$, of a microparticle and its interaction potential, which is characterized by the ion Debye length, $\lambda_{Di} = \sqrt{\epsilon_0 k_B T_i / (n_i e^2)}$. The ion drift velocity and the electric field are related via the ion mobility coefficient, $u = \mu E = M \cdot v_{ti}$, were M is the mach number of the ions calculated by the modified Frost approximation [16]. The scattering parameter serves as a fundamental descriptor of ion-dust interactions in complex plasma environments and can be categorized into three distinct interaction regimes. When the scattering parameter is significantly less than unity ($\beta \ll 1$), the interaction is classified as weak. Conversely, for $\beta \gg 1$, the interaction is considered strong. An intermediate interaction regime is defined when the scattering parameter is of the order of unity ($\beta \approx 1$) [3].

The theoretical models proposed by Khrapak in 2004 and 2005 [3, 17] provide a comprehensive framework for describing ion-dust interactions across weak, intermediate, and strong coupling regimes. Under the experimental conditions investigated in this study (see Section 4.1), which correspond to weak and moderate coupling interactions characterized by $\beta_T \lesssim 5$, the ion drag force is described by [3]:

$$F_{id}^{weak,int} = \frac{8\sqrt{2\pi}}{3} \cdot n_i \cdot m_i \cdot v_{ti} \cdot u_i \cdot \left(a_p^2 + \frac{a_p \rho_0}{2} + \frac{\rho_0^2 \cdot \Lambda}{4} \right), \tag{9}$$

where the modified Coulomb logarithm is expressed as:

$$\Lambda = 2 \cdot \int_0^\infty e^{-x} \ln\left(\frac{2\lambda_D x + \rho_0}{2a_p x + \rho_0}\right) dx. \tag{10}$$

The ion mass, ion thermal velocity, and ion drift velocity are denoted as m_i, v_{ti}, and u_i, respectively. Furthermore, the effective Debye length is calculated from linear combination of the electron Debye length and the ion Debye length and is assumed to be $\lambda_D \sim \lambda_{Di}$.

In this study, we additionally employ a hybrid model based on kinetic theory, as formulated by Hutchinson [11], incorporating a scattering term as described by Khrapak [18]. This combined approach enables the development of an analytical framework, which has been previously applied and refined through particle-in-cell (PIC) and Monte Carlo simulations by Schwabe and Graves [4].

$$F_{id}^{hybrid} = n_i \cdot m_i \cdot v_{ti} \cdot u_i \cdot \left(\sigma_c + \pi\rho_0^2 \left[\Lambda_{0,k}(\tilde{u}_i) + K\left(\frac{\lambda_s(\tilde{u}_i)}{l_i}\right)\right]\right) \tag{11}$$

In the proposed model, the term σ_c denotes the cross-section for ion capture [4]:

$$\sigma_c = \pi a^2 \left(1 + \frac{\rho_0}{a_p}\right) \tag{12}$$

The Coulomb logarithm $\Lambda_{0,k}$ and the collisional function K account for angular momentum loss during ion-neutral collisions [19]:

$$\Lambda_{0,k}(\tilde{u}_i) = \ln\left[\frac{\rho_{0,k}(\tilde{u}_i) + \lambda_s(\tilde{u}_i)}{\rho_{0,k}(\tilde{u}_i) + a_p}\right] \tag{13}$$

and

$$K(x) = x\arctan(x) + \left(\sqrt{\frac{\pi}{2}} - 1\right)\frac{x^2}{1+x^2} - \sqrt{\frac{\pi}{2}}\ln(1+x^2) \tag{14}$$

These terms are adapted to account for interactions extending beyond the Debye length [11]. Numerical calculations indicate that the evaluation of the Coulomb logarithm, $\Lambda_{0,k}(\tilde{u}_i)$, requires an effective ion velocity, $\tilde{u}_i$, which incorporates both the Coulomb radius, $\rho_{0,k}(\tilde{u}_i)$, and a velocity-dependent screening length, defined as [11]:

$$\lambda_s^2 = \frac{\lambda_{D,e}^2}{1 + \frac{2kT_e}{m_i\tilde{u}_i^2}} + a_p^2 \tag{15}$$

The effective ion velocity $\tilde{u}_i$ is given by [11]:

$$\tilde{u}_i^2 = \frac{8k_BT_n}{\pi m_i} + u_i^2\left[1 + \left(\frac{|u_i|/u_B}{0.6 + 0.05\ln(m_\mu) + (\lambda_{D,e}/5a_p)(\sqrt{T_i/T_e} - 0.1)}\right)^3\right] \tag{16}$$

where m_μ denotes the atomic mass corresponding to the plasma species (argon or neon), u_B represents the Bohm velocity, defined as $u_B = \sqrt{k_BT_e/m_i}$. Since the interaction parameters are defined differently, the scattering parameter is accordingly modified as:

$$\beta_T^{hybrid} = \frac{\rho_{0,k(\tilde{u})}}{\lambda_s(\tilde{u})} \tag{17}$$

4. Results and Analysis

In the following, we present a qualitative analysis of the ion drag force by solving the force balance equation (Eq. 1) to extract its contribution. However, this equation strongly depends on several key plasma parameters that are not precisely known, including the individual particle charge, the exact electric field, particle number densities, and temperature distributions.

To address these uncertainties and refine the plasma parameters, we evaluate two proposed ion drag models within a comparative framework (Section 4.1) to identify the model yielding the most accurate predictions. This evaluation is enhanced through a machine learning algorithm based on Bayesian statistics [20]. Key plasma parameters, along with their associated measurement uncertainties, are used as inputs and optimized via regression of an error function, which quantifies the deviation between the model predictions and observed values of the dust particle velocity, v_{mean} and ion drag force, F_{id}, see Figure 2. The optimized plasma parameters, including the derived individual particle charge, are presented in Section 4.2. This methodology provides a robust foundation for the final analysis and results discussed in Section 4.3.

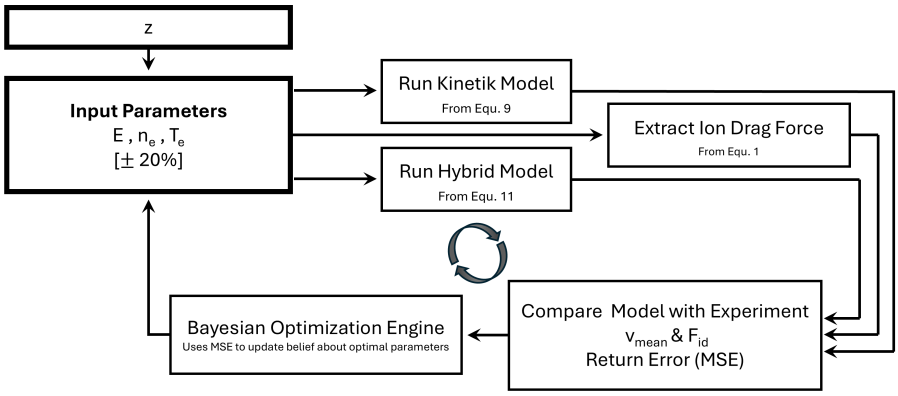

Figure 2: This diagram illustrates the iterative optimization process used to determine key plasma parameters. The parameter space for the electric field E, electron density n_e, and electron temperature T_e is varied within ±20%, while the particle charge potential z remains fixed. For each parameter set, the ion drag models under consideration are evaluated, and the resulting mean dust velocity v_{mean} is compared to experimental data. Additionally, the model-predicted ion drag force F_{id} is compared with values extracted via the force balance Equ. 1. The resulting mean squared error (MSE) serves as feedback for the Bayesian optimization loop, guiding the selection of new parameter sets. The optimization process converged within 200 cycles as the regression model reached saturation.

4.1. Data and Models

The individual velocities of microparticles were determined using machine learning techniques, as described by Dormagen et al. [9]. Specifically, a U-Net [21], a type of convolutional neural network designed for image segmentation, was employed to estimate the weighted center coordinates of particle drift lines. These coordinates were then tracked and linked across multiple images to reconstruct the particle trajectories, thus enabling the calculation of their velocities. The resulting dataset is presented as the average velocity, v_{mean}, in Figure 3 measured in both argon and neon plasmas. The uncertainty associated with v_{mean} was quantified by calculating the standard deviation, based on the assumption that the data adheres to a Gaussian distribution. This assumption is justified by the high statistical significance of the dataset, which indicates that the velocity distribution is centered around the true value.

Our measurements indicate the presence of both positively and negatively polarized velocity distributions, which correspond to the opposing directions of the applied electric field. This is illustrated in the experimental data (+) and (-) shown in Figure 3. The data suggest a reduction in the electric field strength within the positive column. However, deviations of all the key plasma parameters must be considered, to accurately simulate the behavior using the best-fitting models. The final parameter results are discussed in Section 4.2. In the initial stage of the analysis, we focus on the experimental data obtained from the negatively charged discharge column, as this dataset exhibits comparatively smoother trends.

In this study we evaluated the predictive accuracy of theoretical models describing the ion drag force. The analytical model, specifically derived for weak and intermediate ion-particle coupling regimes [3], is denoted as $F_{id}^{weak,int}$ (blue dashed line). In contrast, the hybrid model, which incorporates simulation data [4], is referred to as F_{id}^{hybrid} (yellow dash-dotted line). Model predictions corresponding to the experimental data obtained in the positively charged column are shown in gray, using the respective line styles for clarity.

The model predictions are shown in Figures 3a and 3c for neon, and Figures 3b and 3d for argon, corresponding to discharge currents of 1 mA and 1.5 mA, respectively. In all cases, both models showed consistent predictive performance within the experimental uncertainties and conditions. The optimization procedure aimed to achieve the best possible agreement with experimental data using a unified set of parameters for both model predictions.

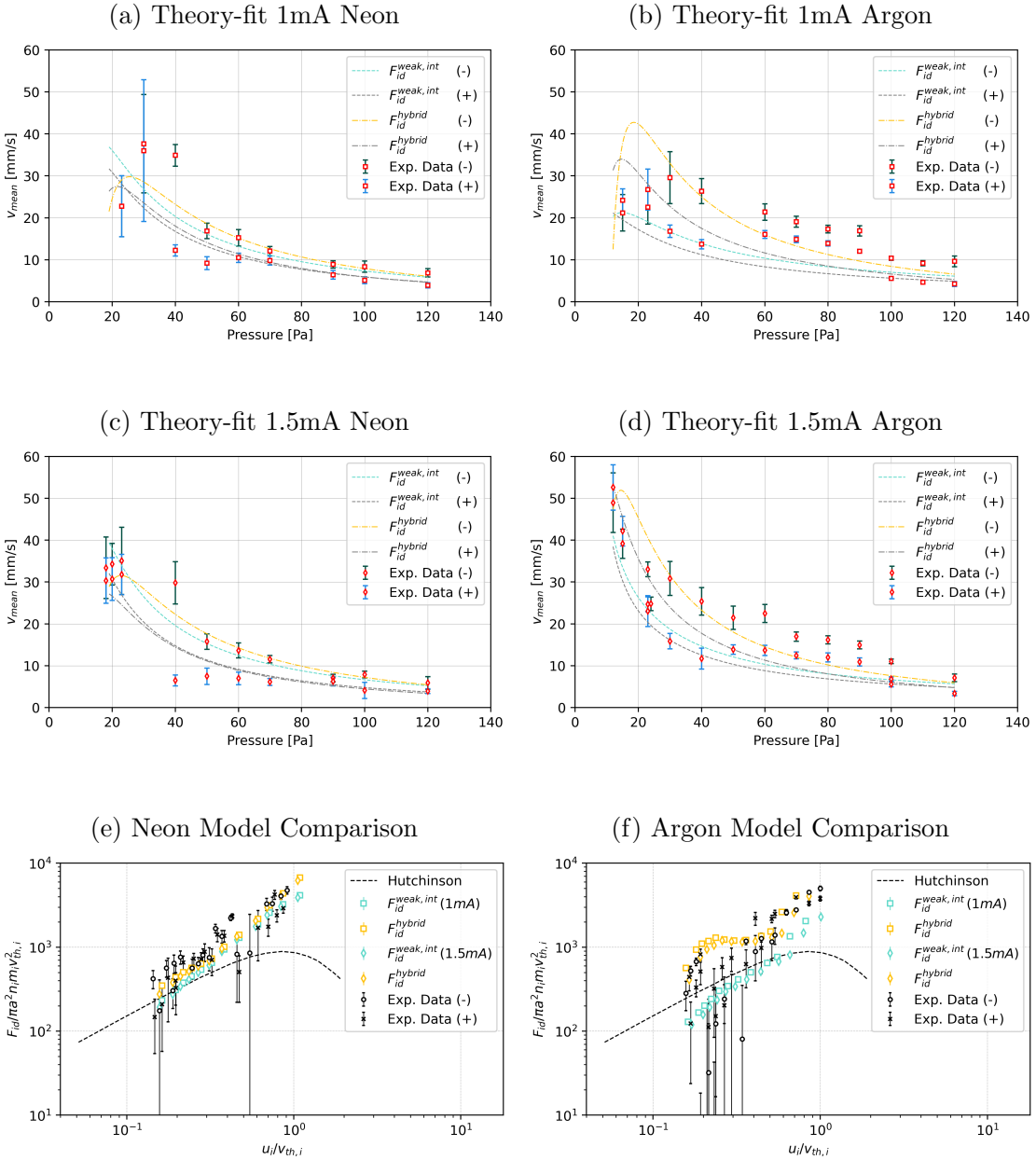

Figure 3: Experimental data obtained during ISS campaigns #17 and #18 are compared with model predictions from an analytical approach for weak and intermediate ion interactions (blue dashed line) and a hybrid model supported by simulations (yellow dash-dotted line). This comparison highlights the effectiveness of the different modeling approaches in reproducing the experimental data and evaluates their predictive accuracy relative to the theoretical framework established by Hutchinson and Khrapak [2].

All models demonstrate strong agreement with experimental measurements within the stated uncertainties up to a critical pressure threshold. Beyond this threshold, deviations are observed, primarily attributed to the increasing influence of neutral gas

damping at elevated pressures. Specifically, for plasma pressures exceeding 40 Pa, the ratio of the neutral drag force to the electric force surpasses approximately $F_n/F_E \gtrsim 0.70$ in neon and $F_n/F_E \gtrsim 0.75$ in argon. Furthermore, in this pressure regime, the neutral drag force exceeds the ion drag force by a factor of at least $F_n/F_i > 2.5$, indicating that neutral damping becomes the dominant mechanism governing the system's dynamics.

4.1.1. Neon Model We observe that the acceleration of microparticles in low-pressure plasma (< 30 Pa) either saturates or decreases, indicating that the ion drag force and the electric field force are of comparable magnitude and in direct competition. This observation, which has not been previously reported [22], suggests a significant amplification of the ion drag force for microparticles with a diameter of $2a_p = 3.4\,\mu m$. This effect becomes more pronounced at a lower discharge current of 1 mA, refered to the electric field being lower.

Furthermore, the F_{id}^{hybrid} model (yellow dash-dotted line) predicts a stronger ion drag force at low pressures (< 30 Pa) compared to the $F_{id}^{weak,int}$ model (blue dashed line) in low-pressure neon discharges, aligning more closely with the trends observed in the experimental data. A key distinction between these models lies in their kinetic treatment of ion dynamics: the hybrid model incorporates an average ion velocity, $\tilde{u}_i$, which accounts for both the thermal motion of ions at room temperature and the ion drift speed. This results in a slightly increased interaction potential of the microparticle.

To further validate our findings, we compare our results with the established kinetic model developed by Hutchinson and Khrapak [2], represented by the dashed line in Figure 3e. The experimental data shown are derived using Equ. 1. At low flow-to-thermal ion velocity ratios ($u_i/v_{th,i} < 1$), the fitted model and experimental data show good agreement with the Hutchinson model, although the experimental data exhibit a slight tendency to overestimate the normalized ion drag force. At higher flow-to-thermal velocity ratios ($u_i/v_{th,i} \sim 1$), observed under low-pressure conditions where kinetic effects become significant, a marked increase in the normalized ion drag force is evident, substantially exceeding the predictions of the Hutchinson and Khrapak model. This enhancement indicates that ion collisions play a crucial role in modifying the ion drag force under moderately collisional conditions [15]. This effect is not explicitly captured in Hutchinson's original formulation, which assumes a Maxwellian ion velocity distribution in a collisionless regime. The better agreement with the hybrid model trend F_{id}^{hybrid} supports the idea that the ion drift speed becomes comparable to or even exceeds the thermal speed. As a result, this has a stronger impact on the calculation of the ion drag force in low-pressure plasmas, leading to improved agreement with experimental data.

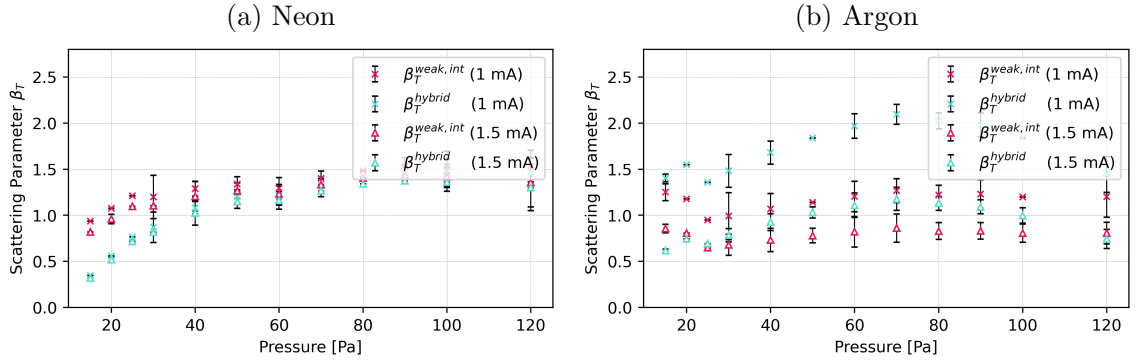

Figure 4: Comparison of the scattering parameter, β_T, across the modeling approaches expressed by the equations 17 and 8 over pressure. Notably, the hybrid model incorporates a mean ion velocity $\tilde{u}_i$, as defined in equation (16), which influences the capture radius $\rho_0(\tilde{u}_i)$ and the screening length $\lambda_s(\tilde{u}_i)$.

The scattering parameter is consistent with our expectations under the conditions we examined. As shown in Figure 4a [17], the scattering parameter $\beta_T \lesssim 5$, which confirms that our model is a good fit for describing microparticle dynamics in the investigated neon plasma environment [3]. Furthermore, we find a significant difference in the scattering parameter between the considered models. The hybrid model, which incorporates the mean ion velocity into its calculations, results in a lower scattering parameter, particularly at low pressures, due to the increased interaction potential.

4.1.2. Argon Model The ion drag force models also yield reliable results when compared with the experimental data obtained in argon plasma (see Figures 3b and 3d). However, a more detailed analysis reveals a larger deviation of the hybrid model, F_{id}^{hybrid}, in the low-pressure regime. This suggests that the improved performance of the weak and intermediate coupling model, $F_{id}^{weak,int}$, is dependent on the type of background gas.

The comparative analysis of model performance, shown in Figure 3f, in conjunction with the kinetic framework of Hutchinson and Khrapak [2], provides additional insights. The experimental data presented are calculated using Equation 1. In argon plasma, the flow-to-thermal ion velocity ratio ($u_i/v_{th,i}$) is higher than in neon plasma at elevated pressures, due to the greater mass of argon ions. Moreover, the ion drift speed u_i does not increase as significantly at lower pressures, resulting in a narrower range of $u_i/v_{th,i}$ compared to neon. This allows the conclusion that, in argon, the plasma conditions are more consistently described by a Maxwellian ion velocity distribution across the full pressure range observed, thereby supporting the improved performance of the weak and intermediate coupling model, $F_{id}^{weak,int}$. The significant deviation in the absolute value of the normalized ion drag force observed in Figure 3f may be attributed to limitations in the plasma model accuracy, as well as the constraint of using a common set of plasma parameters for optimizing both ion drag force models. Nevertheless, this approach allows

for a consistent comparison, as both models are evaluated under identical conditions, providing a fair basis for assessing their relative performance.

The scattering parameter, shown in Figure 4b, does not exhibit a significant increase, with values remaining below $\beta_T \lesssim 5$ across the examined pressure range. However, variations in the adjusted ion velocity, $\tilde{u}_i$, influence the interaction parameter differently than in neon. The hybrid model systematically overestimates the scattering parameter, supporting the conclusion that plasma conditions in argon are less affected by ion collision effects.

4.2. Plasma Parameters

The plasma parameters for the PK-4 experiment have been extensively measured and documented [5]. However, similar data for argon plasma remains scarce. Therefore, we used interpolation and extrapolation techniques to estimate the plasma parameters while ensuring physical consistency. This approach was guided by experimentally measured data obtained via Langmuir probe diagnostics. The triangular (cross) markers in Figure 5 correspond to experimental data recorded at discharge currents of 1 mA (2 mA).

The electron number density in argon, n_e, was assumed to vary linearly with pressure, based on an empirically established trend for neon plasma [5]. This assumption was validated against available experimental data, with the final results shown in the upper panel of Figure 5. Model fitting and optimization revealed a 30% reduction in the electron number density for neon at a discharge current of 1.5 mA compared to values reported in the literature, while no reduction was observed at 1 mA. No significant deviation was detected with respect to discharge polarity. This discrepancy remains within the reported measurement uncertainties [5].

A similar methodology was employed to estimate the electron temperature in argon, T_e, in argon plasma. The trend was extrapolated from neon plasma data and adjusted within the uncertainty bounds of the measurements. The resulting analysis indicates a 10-15% reduction in electron temperature at a 1 mA discharge current in the positive column compared to prior published values. This deviation is particularly relevant in explaining discrepancies observed in the measured microparticle velocities under positive and negative discharge polarities.

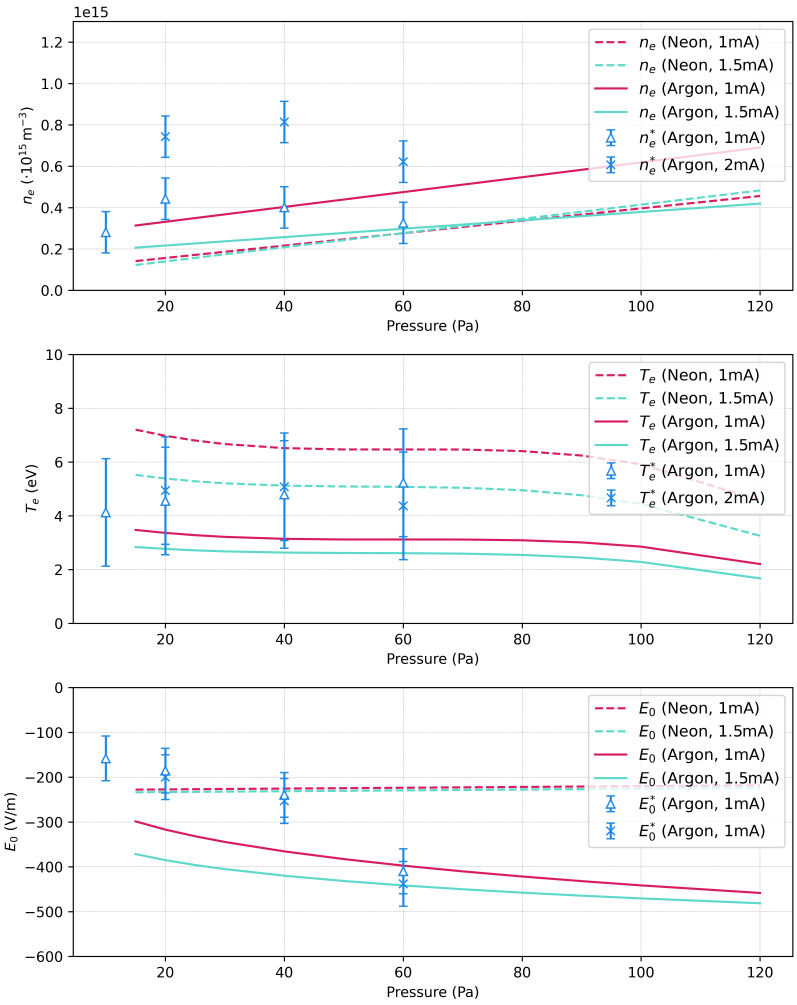

Figure 5: The figure presents measured plasma parameters in argon plasma, with triangular (cross) markers indicating data obtained at discharge currents of 1 mA (2 mA), which were used as reference points for extrapolation and optimization. The results (solid) follow trends taken from precise measurements in neon (dashed) for the electron number density, n_e, and temperature, T_e, while a distinct approach was applied to the electric field in argon, E_0, to achieve the most accurate results.

The variations in microparticle speeds, as previously discussed, suggest that the electric field, E_0, plays a critical role. For neon plasma, an increase of 5-15% of the electric field was observed in the negative column in contrast to the values reported in the literature [5]. The electric field for argon plasma was determined through modeling, with the most accurate results obtained by fitting a power-law function within the expected parameter range. A final empirical relationship describing the electric field as a function of pressure and discharge current was derived using this power-law model. The resulting expression is given by:

$$E_0(V/cm) \approx -(1.636 \cdot I_{DC}^{1.309}) \cdot P^{(0.31-0.135 \cdot I_{DC})} \tag{18}$$

where P is the pressure in pascal (Pa) and I_{DC} is the discharge current in milliamperes (mA). This equation describes the dependence of the electric field on the operating conditions of the discharge plasma, covering a current range from 1 mA to 2 mA. Additionally, no deviations in the electric field were observed under specific plasma conditions, for neither positive nor negative column.

Beyond the direct influence of plasma parameters on the analysis, we additionally accounted for the microparticle density, n_d, which indirectly affects the plasma composition through the quasi-neutrality condition, $n_i = n_e + Z_d n_d$. During experimental investigations, efforts were made to minimize the microparticle density. However, precise control over the injection of microparticles remains challenging, and the complexities associated with multi-particle interactions must also be considered.

A widely used approach for estimating microparticle density is based on the formation of crystalline structures, where the density is inferred from the average interparticle distance. Conversely, in cases where microparticles are randomly distributed while drifting, a broader range of densities can be encountered. Since our experimental setup was not specifically designed to investigate structural variations, density estimates were also derived by referencing prior studies [23]. These studies report interparticle distances consistent with our estimates, corresponding to microparticle densities in the range of 0.08 to $1.01 \times 10^{11}\,\mathrm{m}^{-3}$. While this range may appear broad, its impact on the final results remains minimal, as the Havnes parameter varies between 0.1 and 0.7, remaining below unity and thereby indicating a weak influence on the overall plasma system [2, 12].

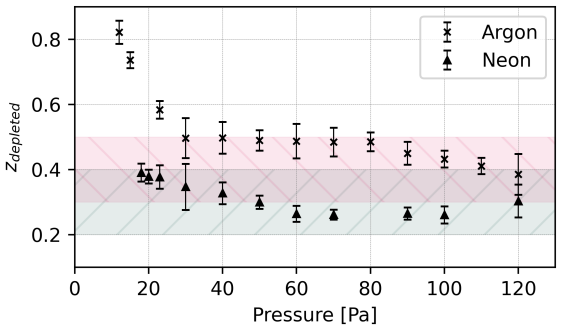

Figure 6: The dimensionless reduced charge potential, $z_{depleted}$, of an isolated microparticle in both neon and argon plasmas is presented. The term "depleted" reflects the consideration of multiparticle effects in the charge estimation. The results are consistent with previous studies, which suggest a charge potential of $z_{argon} = 0.4$ and $z_{neon} = 0.3$, as indicated by the hatched regions (pink and blue).

The optimized model predictions provide valuable insights into specific plasma parameters and enable refined micro-adjustments. Notably, these findings are obtained through parameter optimization, allowing for an estimation of the individual microparticle charge potential, as illustrated in Figure 6. The final results are compared

with previous studies [7, 23], which suggest a microparticle charge potential of $z = 0.3 \pm 0.1$ in neon and $z = 0.4 \pm 0.1$ in argon.

4.3. Ion drag force

The final results for the ion drag force, extracted from the force balance Equ. 1, are presented in Figure 7 as a function of pressure for both plasma types. The corresponding model predictions are also shown, including an uncertainty corridor that represents the range of variation in the measured ion drag force data.

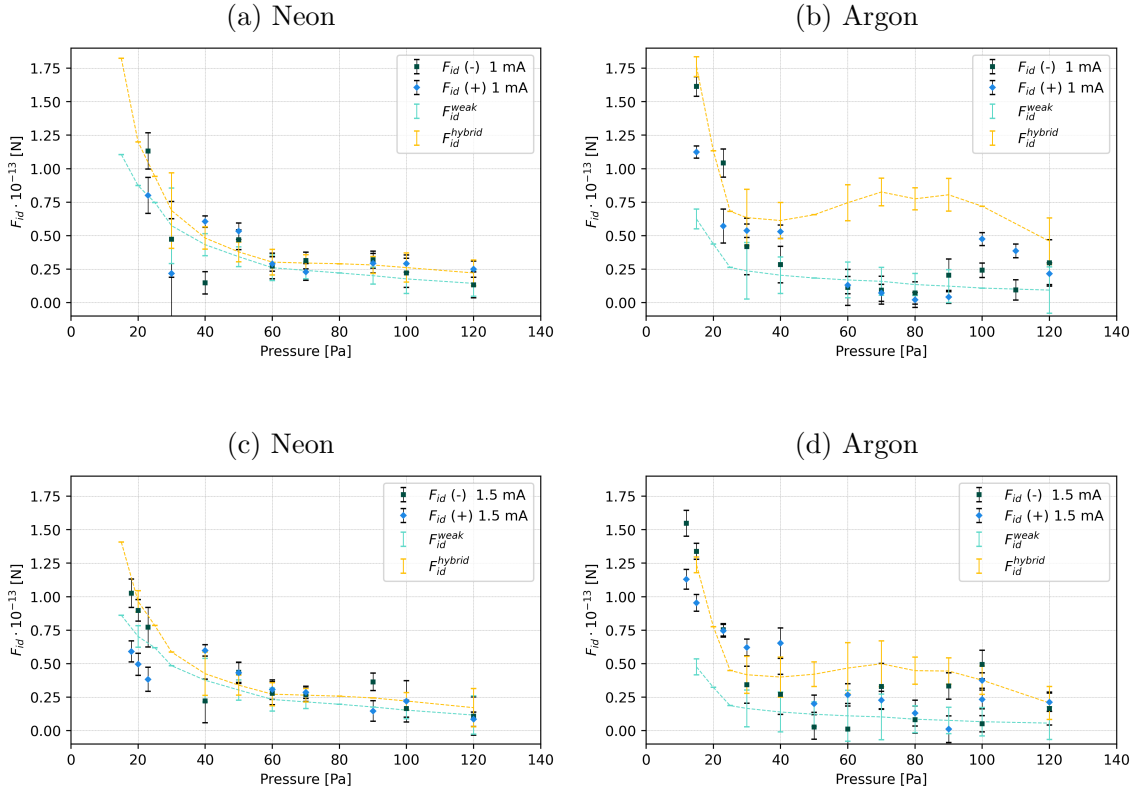

Figure 7: The extracted ion drag force, F_{id}, obtained from equation (1), represents the experimentally measured data and is compared to the values derived from the best-fitting model (dotted lines) over pressure. The uncertainties are determined based on measurement errors.

5. Conclusion

This study presents a comprehensive investigation of ion drag force dynamics in low-pressure complex plasmas using data from the PK-4 facility aboard the ISS. By analyzing microparticle motion in both neon and argon plasmas under varying discharge currents and pressures, we extracted the ion drag force and compared the results with two

theoretical models. The analytical model for weak and intermediate coupling, and a hybrid model integrating kinetic effects have been tested.

Our results demonstrate that both models reproduce experimental trends well across a broad range of conditions, but notable differences arise at low pressures. In neon plasmas, the hybrid model shows better agreement with experimental data, particularly when the ion drift speed approaches or exceeds the thermal speed, leading to enhanced scattering and interaction potentials. In contrast, argon plasmas are less sensitive to these effects. As a result, the analytical model provides more accurate predictions, indicating that a Maxwellian ion velocity distribution is more applicable in this regime.

The scattering parameter analysis further supports these findings, as the microparticle–ion interaction behaves differently in argon compared to neon depending on the chosen model. In particular, kinetic effects become less significant and tend to overestimate the ion drag force in argon. This study also highlights the importance of accurately determining plasma parameters, which was achieved here through machine learning-based optimization and extrapolation of Langmuir probe diagnostics.

Overall, this work confirms that ion drag models must be tailored to the specific gas environment to yield accurate predictions. To promote transparency and reproducibility, the models and analysis routines used in this study are openly available on GitHub [24], providing a valuable resource for future modeling and analysis of dust-plasma interactions in microgravity and laboratory settings.

6. Acknowledgments

This work was supported by DLR under Grant No. 50WM2044 and 50WK2270B.
The work in scope of this paper of A.V.Z, A.M.L., A.D.U. and O.F.P. was also supported by the Ministry of Science and Higher Education of the Russian Federation (State Assignment No. 075-00269-25-00).
All authors greatly acknowledge the joint ESA-Roscosmos "Experiment Plasmakristall-4" onboard the International Space Station. We also express our gratitude to Mikhail Pustylnik and Hubertus Thomas from DLR for their support, as well as to the CADMOS Operations Team for their work during the ISS campaigns.

References

[1] Hartmut Zohm. *Plasmaphysik*. Tech. rep. https://www.ipp.mpg.de/2155286/Plasmaphysik. Ludwig-Maximilian-University Munich, 2012.

[2] André Melzer. *Physics of Dusty Plasmas*. Springer Cham, 2019. DOI: https://doi.org/10.1007/978-3-030-20260-6.

[3] S. A. Khrapak et al. "Particle charge in the bulk of gas discharges". In: *Phys. Rev. E* 72 (1 July 2005), p. 016406. DOI: 10.1103/PhysRevE.72.016406. URL: https://link.aps.org/doi/10.1103/PhysRevE.72.016406.

[4] M. Schwabe and D. B. Graves. "Simulating the dynamics of complex plasmas". In: *Phys. Rev. E* 88 (2 Aug. 2013), p. 023101. DOI: 10.1103/PhysRevE.88.023101. URL: https://link.aps.org/doi/10.1103/PhysRevE.88.023101.

[5] M. Y. Pustylnik et al. "Plasmakristall-4: New complex (dusty) plasma laboratory on board the International Space Station". In: *Review of Scientific Instruments* 87.9 (Sept. 2016), p. 093505. ISSN: 0034-6748. DOI: 10.1063/1.4962696. eprint: https://pubs.aip.org/aip/rsi/article-pdf/doi/10.1063/1.4962696/15757864/093505_1_online.pdf. URL: https://doi.org/10.1063/1.4962696.

[6] A. V. Zobnin et al. "Ion current on a small spherical attractive probe in a weakly ionized plasma with ion-neutral collisions (kinetic approach)". In: *Physics of Plasmas* 15.4 (Apr. 2008), p. 043705. ISSN: 1070-664X. DOI: 10.1063/1.2903052. eprint: https://pubs.aip.org/aip/pop/article-pdf/doi/10.1063/1.2903052/13598502/043705_1_online.pdf. URL: https://doi.org/10.1063/1.2903052.

[7] T. Antonova et al. "Particle charge in PK-4 dc discharge from ground-based and microgravity experiments". In: *Physics of Plasmas* 26.11 (Nov. 2019), p. 113703. ISSN: 1070-664X. DOI: 10.1063/1.5122861. eprint: https://pubs.aip.org/aip/pop/article-pdf/doi/10.1063/1.5122861/15963866/113703_1_online.pdf. URL: https://doi.org/10.1063/1.5122861.

[8] Michael Kretschmer et al. "Wave phenomena in a stratified complex plasma". In: *IEEE Transactions on Plasma Science* 44.4 (2015), pp. 458–462. DOI: 10.1109/TPS.2015.2501831.

[9] N Dormagen et al. "Local classification of crystalline structures in complex plasmas using a PointNet". In: *Machine Learning: Science and Technology* 5.4 (Oct. 2024), p. 045006. DOI: 10.1088/2632-2153/ad8062. URL: https://dx.doi.org/10.1088/2632-2153/ad8062.

[10] Jan Carstensen et al. "Probing the plasma sheath by the continuous mass loss of microparticles". In: *IEEE Transactions on Plasma Science* 41.4 (2012), pp. 764–768.

[11] IH Hutchinson. "Collisionless ion drag force on a spherical grain". In: *Plasma physics and controlled fusion* 48.2 (2006), p. 185.

[12] V.E. Fortov et al. "Complex (dusty) plasmas: Current status, open issues, perspectives". In: *Physics Reports* 421.1 (2005), pp. 1–103. ISSN: 0370-1573. DOI: https://doi.org/10.1016/j.physrep.2005.08.007. URL: https://www.sciencedirect.com/science/article/pii/S0370157305003339.

[13] L Wimmer et al. "Impact of particle charge and electrorheology-effects on dust-acoustic waves in low pressure complex plasma under microgravity". In: *New Journal of Physics* 27.3 (Feb. 2025), p. 033001. DOI: 10.1088/1367-2630/adb876. URL: https://dx.doi.org/10.1088/1367-2630/adb876.

[14] S. A. Khrapak et al. "Ion drag force in complex plasmas". In: *Phys. Rev. E* 66 (4 Oct. 2002), p. 046414. DOI: 10.1103/PhysRevE.66.046414. URL: https://link.aps.org/doi/10.1103/PhysRevE.66.046414.

[15] I. H. Hutchinson and C. B. Haakonsen. "Collisional effects on nonlinear ion drag force for small grains". In: *Physics of Plasmas* 20.8 (Aug. 2013), p. 083701. ISSN: 1070-664X. DOI: 10.1063/1.4818144. eprint: https://pubs.aip.org/aip/pop/article-pdf/doi/10.1063/1.4818144/16056909/083701_1_online.pdf. URL: https://doi.org/10.1063/1.4818144.

[16] Sergey A. Khrapak and Alexey G. Khrapak. "Modified Frost formula for the mobilities of positive ions in their parent gases". In: *AIP Advances* 9.9 (Sept. 2019), p. 095008. ISSN: 2158-3226. DOI: 10.1063/1.5113793. eprint: https://pubs.aip.org/aip/adv/article-pdf/doi/10.1063/1.5113793/12919042/095008_1_online.pdf. URL: https://doi.org/10.1063/1.5113793.

[17] S.A. Khrapak et al. "Scattering in the attractive Yukawa potential: application to the ion-drag force in complex plasmas". In: *IEEE Transactions on Plasma Science* 32.2 (2004), pp. 555–560. DOI: 10.1109/TPS.2004.826073.

[18] S. A. Khrapak et al. "Ion drag force in complex plasmas". In: *Phys. Rev. E* 66 (4 Oct. 2002), p. 046414. DOI: 10.1103/PhysRevE.66.046414. URL: https://link.aps.org/doi/10.1103/PhysRevE.66.046414.

[19] SA Khrapak et al. "Hybrid approach to the ion drag force". In: *Physics of plasmas* 12.4 (2005).

[20] Milica Miočević, Roy Levy, and Rens van de Schoot. "Introduction to Bayesian statistics". In: *Small Sample Size Solutions*. Routledge, 2020, pp. 3–12.

[21] Olaf Ronneberger, Philipp Fischer, and Thomas Brox. "U-net: Convolutional networks for biomedical image segmentation". In: *Medical image computing and computer-assisted intervention–MICCAI 2015: 18th international conference, Munich, Germany, October 5-9, 2015, proceedings, part III 18*. Springer. 2015, pp. 234–241.

[22] S. A. Khrapak et al. "Particle flows in a dc discharge in laboratory and microgravity conditions". In: *Phys. Rev. E* 87 (6 June 2013), p. 063109. DOI: 10.1103/PhysRevE.87.063109. URL: https://link.aps.org/doi/10.1103/PhysRevE.87.063109.

[23] L. Wimmer et al. "Tilted dust-acoustic waves in low-pressure DC complex plasma". In: *Physics of Plasmas* 31.4 (Apr. 2024), p. 043702. ISSN: 1070-664X. DOI: 10.1063/5.0190499. eprint: https://pubs.aip.org/aip/pop/article-pdf/doi/10.1063/5.0190499/19880579/043702_1_5.0190499.pdf. URL: https://doi.org/10.1063/5.0190499.

[24] L. Wimmer. *Ion Drag Modeling*. https://github.com/luki58/Ion-Drag-Modeling. Accessed: 2025-04-01. 2025.

Chapter 5

Conclusion and Outlook

This thesis presents a systematic investigation of dust acoustic wave (DAW) dynamics and particle-plasma interactions in low-pressure DC discharges, with a focus on the role of electric field modulation and boundary effects. Across multiple experimental campaigns, the interplay between particle charge, wave excitation, and ion drag forces was examined using advanced analysis techniques and newly developed data pipelines.

A central and recurring observation throughout all publications is the increase of ion temperature at very low neutral gas pressures. This effect, attributed to the increasing ion mean free path under low-collision conditions, leads to significant acceleration of ions in the electric field and alters the energy balance in the plasma. The elevated ion temperature was consistently observed to impact dust dynamics, force balance, and wave excitation thresholds across all experiments.

In the first study, enhanced ion temperatures were linked to observed deviations in DAW propagation. Contrary to initial assumptions of screw-like or helical wave structures, three-dimensional particle tracking and tomographic reconstruction ruled out such trajectories. Instead, wavefront deformations and elevated phase velocities were attributed to spatial asymmetries in the electric field near the boundary, with gravitational settling of microparticles further contributing to confinement effects.

The second study investigated the influence of temporally modulated electric fields on particle charging. The electrorheological effect was experimentally identified through deviations from linear dispersion predictions and shown to modulate the local charge environment, affecting wave propagation. While previously described only in simulations, this study provided the first experimental confirmation of the effect in realistic plasma conditions. Refined charge models, validated through these findings, significantly improved predictions of DAW phase velocities. This coupling between field modulation and charge dynamics was further demonstrated during the crystallization of a drifting cloud, where string-like structures emerged before the onset of self-excited DAWs, driven by sustained external energy input.

In the final study, a novel method was introduced for measuring the ion drag force on isolated microparticles. This approach combined a neural network-based particle tracking algorithm with Bayesian optimization to extract plasma parameters and evaluate theoret-

ical ion drag models. The pipeline enabled high-accuracy force estimation across extended datasets and under imaging conditions typically challenging for manual analysis. Application to both neon and argon plasmas revealed a distinct difference in ion drag behavior, with neon showing increased sensitivity at low pressures, further supporting the presence of non-Maxwellian ion distributions under these conditions.

In summary, this work establishes a coherent framework for analyzing complex plasma dynamics under driven, low-pressure conditions. It highlights the critical influence of ion temperature, modulated electric fields, and boundary effects on both microscopic and macroscopic phenomena. The combination of refined diagnostics, data-driven modeling, and theoretical analysis advances the understanding of wave-particle coupling and ion drag in complex plasmas.

All analysis codes developed for this thesis are available as open-source software. In particular, the pipeline for ion drag force estimation offers a flexible tool for exploring a broader range of plasma parameters. Its continued application can support future efforts to map out complex plasma behavior with greater precision, especially in regimes characterized by low neutral pressure and strong non-equilibrium effects.

Bibliography

[1] George K Parks. *Physics of space plasmas: an introduction*. CRC Press, 2019.

[2] Ulrich Stroth. *Plasmaphysik*. Springer, 2011.

[3] P. K. Shukla and A. A. Mamun. *Introduction to Dusty Plasma Physics*. IOP Publishing, 2002.

[4] Alexander GGM Tielens. *The physics and chemistry of the interstellar medium*. Cambridge University Press, 2005.

[5] Katia M. Ferrière. "The interstellar environment of our galaxy". In: *Reviews of Modern Physics* 73.4 (2001), pp. 1031–1066. DOI: 10.1103/RevModPhys.73.1031.

[6] Weston M Stacey. *Fusion: An introduction to the physics and technology of magnetic confinement fusion*. John Wiley & Sons, 2010.

[7] SS Harilal, CV Bindhu, MS Tillack, F Najmabadi, and AC Gaeris. "Internal structure and expansion dynamics of laser ablation plumes into ambient gases". In: *Journal of applied physics* 93.5 (2003), pp. 2380–2388.

[8] Irving Langmuir. "Oscillations in Ionized Gases". In: *Proceedings of the National Academy of Sciences* 14.8 (1928), pp. 627–637. DOI: 10.1073/pnas.14.8.627.

[9] André Melzer. *Physics of Dusty Plasmas*. Springer Cham, 2019. DOI: https://doi.org/10.1007/978-3-030-20260-6.

[10] Vladimir E. Fortov, Anatoly P. Nefedov, and et al. *Dusty Plasmas: Physics, Chemistry, and Technological Impacts in Plasma Processing*. Springer, 2005.

[11] D. A. Mendis and M. Rosenberg. "Cosmic dusty plasma". In: *Annual Review of Astronomy and Astrophysics* 32 (1994), pp. 419–463. DOI: 10.1146/annurev.aa.32.090194.002223.

[12] Bruce T. Draine. "Interstellar Dust Grains". In: *Annual Review of Astronomy and Astrophysics* 41.1 (2003), pp. 241–289. DOI: 10.1146/annurev.astro.41.011802.094840.

[13] Christoph K. Goertz and G. E. Morfill. "A model for the formation of spokes in Saturn's rings". In: *Icarus* 53.2 (1983), pp. 219–229. DOI: 10.1016/0019-1035(83)90143-0.

[14] Gregor E. Morfill and Alexei V. Ivlev. "Complex plasmas: An interdisciplinary research field". In: *Reviews of Modern Physics* 81.4 (2009), pp. 1353–1404. DOI: 10.1103/RevModPhys.81.1353.

[15] Fortov, A.V. Ivlev, S.A. Khrapak, A.G. Khrapak, and G.E. Morfill. "Complex (dusty) plasmas: Current status, open issues, perspectives". In: *Physics Reports* 421.1 (2005), pp. 1–103. ISSN: 0370-1573. DOI: https://doi.org/10.1016/j.physrep.2005.08.007. URL: https://www.sciencedirect.com/science/article/pii/S0370157305003339.

[16] Themis Matsoukas and Marc Russell. "Particle charging in low-pressure plasmas". In: *Journal of Applied Physics* 77.9 (May 1995), pp. 4285–4292. ISSN: 0021-8979. DOI: 10.1063/1.359451. eprint: https://pubs.aip.org/aip/jap/article-pdf/77/9/4285/18675535/4285_1_online.pdf. URL: https://doi.org/10.1063/1.359451.

[17] Iris Kock, T Edler, and Stefan G Mayr. "Growth behavior and intrinsic properties of vapor-deposited iron palladium thin films". In: *Journal of Applied Physics* 103.4 (2008).

[18] Vladimir E Fortov, Aleksei G Khrapak, Sergei A Khrapak, Vladimir I Molotkov, and Oleg F Petrov. "Dusty plasmas". In: *Physics-Uspekhi* 47.5 (2004), p. 447.

[19] V. E. Fortov et al. "Mechanism of dust-acoustic instability in a direct current glow discharge plasma". In: *Physics of Plasmas* 7.5 (May 2000), pp. 1374–1380. ISSN: 1070-664X. DOI: 10.1063/1.873954. eprint: https://pubs.aip.org/aip/pop/article-pdf/7/5/1374/12332163/1374_1_online.pdf. URL: https://doi.org/10.1063/1.873954.

[20] H. Rothermel, T. Hagl, G. E. Morfill, M. H. Thoma, and H. M. Thomas. "Gravity Compensation in Complex Plasmas by Application of a Temperature Gradient". In: *Phys. Rev. Lett.* 89 (17 Oct. 2002), p. 175001. DOI: 10.1103/PhysRevLett.89.175001. URL: https://link.aps.org/doi/10.1103/PhysRevLett.89.175001.

[21] Paul S. Epstein. "On the Resistance Experienced by Spheres in their Motion through Gases". In: *Phys. Rev.* 23 (6 June 1924), pp. 710–733. DOI: 10.1103/PhysRev.23.710. URL: https://link.aps.org/doi/10.1103/PhysRev.23.710.

[22] Jan Carstensen et al. "Probing the plasma sheath by the continuous mass loss of microparticles". In: *IEEE Transactions on Plasma Science* 41.4 (2012), pp. 764–768.

[23] Michael S Barnes, John H Keller, John C Forster, James A O'Neill, and D Keith Coultas. "Transport of dust particles in glow-discharge plasmas". In: *Physical review letters* 68.3 (1992), p. 313.

[24] S. A. Khrapak et al. "Particle charge in the bulk of gas discharges". In: *Phys. Rev. E* 72 (1 July 2005), p. 016406. DOI: 10.1103/PhysRevE.72.016406. URL: https://link.aps.org/doi/10.1103/PhysRevE.72.016406.

[25] S.A. Khrapak, A.V. Ivlev, G.E. Morfill, S.K. Zhdanov, and H.M. Thomas. "Scattering in the attractive Yukawa potential: application to the ion-drag force in complex plasmas". In: *IEEE Transactions on Plasma Science* 32.2 (2004), pp. 555–560. DOI: 10.1109/TPS.2004.826073.

[26] S. A. Khrapak, A. V. Ivlev, G. E. Morfill, and S. K. Zhdanov. "Scattering in the Attractive Yukawa Potential in the Limit of Strong Interaction". In: *Phys. Rev. Lett.* 90 (22 June 2003), p. 225002. DOI: 10.1103/PhysRevLett.90.225002. URL: https://link.aps.org/doi/10.1103/PhysRevLett.90.225002.

[27] W.J. Goedheer, V. Land, and J. Venema. "Modelling of Voids in Complex Radio Frequency Plasmas". In: *Contributions to Plasma Physics* 49.4-5 (2009), pp. 199–214. DOI: https://doi.org/10.1002/ctpp.200910023. eprint: https://onlinelibrary.wiley.com/doi/pdf/10.1002/ctpp.200910023. URL: https://onlinelibrary.wiley.com/doi/abs/10.1002/ctpp.200910023.

[28] M. Schwabe and D. B. Graves. "Simulating the dynamics of complex plasmas". In: *Phys. Rev. E* 88 (2 Aug. 2013), p. 023101. DOI: 10.1103/PhysRevE.88.023101. URL: https://link.aps.org/doi/10.1103/PhysRevE.88.023101.

[29] NN Rao, PK Shukla, and M Yu Yu. "Dust-acoustic waves in dusty plasmas". In: *Planetary and space science* 38.4 (1990), pp. 543–546.

[30] M Schwabe et al. "Slowing of acoustic waves in electrorheological and string-fluid complex plasmas". In: *New Journal of Physics* 22.8 (Aug. 2020), p. 083079. DOI: 10.1088/1367-2630/aba91b. URL: https://dx.doi.org/10.1088/1367-2630/aba91b.

[31] Tian Hao. *Electrorheological fluids: The non-aqueous suspensions*. Vol. 22. Elsevier, 2011.

[32] A. V. Ivlev, M. H. Thoma, C. Räth, G. Joyce, and G. E. Morfill. "Complex Plasmas in External Fields: The Role of Non-Hamiltonian Interactions". In: *Phys. Rev. Lett.* 106 (15 Apr. 2011), p. 155001. DOI: 10.1103/PhysRevLett.106.155001. URL: https://link.aps.org/doi/10.1103/PhysRevLett.106.155001.

[33] Max Klein, Niklas Dormagen, C Dietz, Markus Thoma, and Mike Schwarz. "Enhancing particle string detection in electrorheological plasmas using asymmetrical kernel convolutional networks". In: *Machine Learning: Science and Technology* 5 (May 2024). DOI: 10.1088/2632-2153/ad4d3e.

[34] S. Mitic et al. "Long-term evolution of the three-dimensional structure of string-fluid complex plasmas in the PK-4 experiment". In: *Phys. Rev. E* 103 (6 June 2021), p. 063212. DOI: 10.1103/PhysRevE.103.063212. URL: https://link.aps.org/doi/10.1103/PhysRevE.103.063212.

[35] Christopher Dietz, Johannes Budak, Tobias Kamprich, Michael Kretschmer, and Markus H. Thoma. "Phase transition in electrorheological plasmas". In: *Contributions to Plasma Physics* 61.10 (2021). e202100079 ctpp.202100079.R1, e202100079. DOI: https://doi.org/10.1002/ctpp.202100079. eprint: https://onlinelibrary.wiley.com/doi/pdf/10.1002/ctpp.202100079. URL: https://onlinelibrary.wiley.com/doi/abs/10.1002/ctpp.202100079.

[36] V Fortov et al. "The project 'Plasmakristall-4'(PK-4)—A new stage in investigations of dusty plasmas under microgravity conditions: First results and future plans". In: *Plasma physics and controlled fusion* 47.12B (2005), B537.

[37] Hubertus M Thomas, Mierk Schwabe, and Mikhail Pustylnik. "PK-4–Complex Plasma Research on the International Space Station". In: *Munich Aerospace* (2020).

[38] Anatoli P Nefedov et al. "PKE-Nefedov*: Plasma crystal experiments on the international space station". In: *New journal of physics* 5.1 (2003), p. 33.

[39] C A Knapek et al. "COMPACT—a new complex plasma facility for the ISS". In: *Plasma Physics and Controlled Fusion* 64.12 (Nov. 2022), p. 124006. DOI: 10.1088/1361-6587/ac9ff0. URL: https://dx.doi.org/10.1088/1361-6587/ac9ff0.

[40] M. Y. Pustylnik et al. "Plasmakristall-4: New complex (dusty) plasma laboratory on board the International Space Station". In: *Review of Scientific Instruments* 87.9 (Sept. 2016), p. 093505. ISSN: 0034-6748. DOI: 10.1063/1.4962696. eprint: https://pubs.aip.org/aip/rsi/article-pdf/doi/10.1063/1.4962696/15757864/093505_1_online.pdf. URL: https://doi.org/10.1063/1.4962696.

[41] Michael Kretschmer, Tetyana Antonova, Sergey Zhdanov, and Markus Thoma. "Wave phenomena in a stratified complex plasma". In: *IEEE Transactions on Plasma Science* 44.4 (2015), pp. 458–462. DOI: 10.1109/TPS.2015.2501831.

[42] Vladimir Pletser et al. "European parabolic flight campaigns with Airbus ZERO-G: Looking back at the A300 and looking forward to the A310". In: *Advances in Space Research* 56.5 (2015), pp. 1003–1013. ISSN: 0273-1177. DOI: https://doi.org/10.1016/j.asr.2015.05.022. URL: https://www.sciencedirect.com/science/article/pii/S0273117715003622.

[43] Eshita Joshi, Markus H Thoma, and Mierk Schwabe. "Particle-resolved study of the onset of turbulence". In: *Physical Review Research* 6.1 (2024), p. L012013.

[44] L. Wimmer. *PFC42*. https://github.com/luki58/PFC42. Accessed: 2025-04-01. 2024.

[45] L. Wimmer. *Ion Drag Modeling*. https://github.com/luki58/Ion-Drag-Modeling. Accessed: 2025-04-01. 2025.

[46] Milica Miočević, Roy Levy, and Rens van de Schoot. "Introduction to Bayesian statistics". In: *Small Sample Size Solutions*. Routledge, 2020, pp. 3–12.

[47] Niklas Dormagen, Max Klein, Andreas Sylvester Schmitz, Markus Thoma, and Mike Schwarz. "Multi-Particle Tracking in Complex Plasmas Using a Simplified and Compact U-Net". In: *Journal of Imaging* 10 (Jan. 2024), p. 40. DOI: 10.3390/jimaging10020040.

[48] Max Klein, Niklas Dormagen, Lukas Wimmer, Markus H. Thoma, and Mike Schwarz. "Advancing Particle Tracking: Self-Organizing Map Hyperparameter Study and Long Short-Term Memory-Based Outlier Detection". In: *Machine Learning and Knowledge Extraction* 7.2 (2025). ISSN: 2504-4990. URL: https://www.mdpi.com/2504-4990/7/2/37.

Publications During the Ph.D.

This section enumerates all scientific publications resulting from research conducted during the Ph.D. period. The list includes both first-author and co-authored works, presented in chronological order.

1. Drescher, A., Fabricius, M., Shimizu, T., Woillez, J., Bourget, P., Widmann, F., ... Wimmer, L., Yazici, S. *GRAVITY+ Wide: Towards hundreds of $z \sim 2$ AGN.* **arXiv preprint**, arXiv:2209.11602, 2022. `https://arxiv.org/abs/2209.11602`

2. Wimmer, L., Schmitz, A. S., Kretschmer, M., Thoma, M. H. *Tilted dust-acoustic waves in low-pressure DC complex plasma.* **Physics of Plasmas**, **31**(4), 043702, 2024. DOI: 10.1063/5.0190499 `https://doi.org/10.1063/5.0190499`

3. Dormagen, N., Klein, M., Schmitz, A. S., Wimmer, L., Thoma, M. H., Schwarz, M. *Local classification of crystalline structures in complex plasmas using a PointNet.* **Machine Learning: Science and Technology**, **5**(4), 045006, 2024. DOI: 10.1088/2632-2153/ad8062

4. Wimmer, L., Dormagen, N., Klein, M., Kretschmer, M., Lipaev, A. M., Schwarz, M., Usachev, A. D., Petrov, O. F., Zobnin, A. V., Thoma, M. H. *Impact of particle charge and electrorheology-effects on dust-acoustic waves in low pressure complex plasma under microgravity.* **New Journal of Physics**, **27**(3), 033001, 2025. DOI: 10.1088/1367-2630/adb876 `https://dx.doi.org/10.1088/1367-2630/adb876`

5. Klein, M., Dormagen, N., Wimmer, L., Thoma, M. H., Schwarz, M. *Advancing Particle Tracking: Self-Organizing Map Hyperparameter Study and Long Short-Term Memory-Based Outlier Detection.* **Machine Learning and Knowledge Extraction**, **7**(2), Article 37, 2025. DOI: 10.3390/make7020037 `https://www.mdpi.com/2504-4990/7/2/37`

Declaration of Authorship

I declare that I have completed this dissertation single-handedly without the unauthorized help of a second party and only with the assistance acknowledged therein. I have appropriately acknowledged and cited all text passages that are derived verbatim from or are based on the content of published work of others, and all information relating to verbal communications. I consent to the use of an anti-plagiarism software to check my thesis. I have abided by the principles of good scientific conduct laid down in the charter of the Justus Liebig University Giessen *„Satzung der Justus-Liebig-Universität Gießen zur Sicherung guter wissenschaftlicher Praxis“* in carrying out the investigations described in the dissertation.

Signed: _____

Date: _____

Acknowledgements

First and foremost, I would like to express my sincere gratitude to my supervisor, Prof. Dr. Markus H. Thoma, for his continuous support, trust, and the many opportunities he provided throughout my Ph.D. He granted me the freedom and time necessary to fully concentrate on my work, and his expertise was invaluable during both the research and writing phases of this thesis.

I would also like to thank the members of my thesis committee, Prof. Dr. Simone Sanna, Prof. Dr. Stefan Schippers, and Prof. Dr. Annika Thiel, for their time and valuable feedback.

My thanks also go to the Deutsches Zentrum für Luft- und Raumfahrt (DLR) for funding this work under Grant Nos. 50WM2044 and 50WK2270B. I am especially grateful to Mikhail Pustylnik from DLR for his collaboration and support throughout the projects.

Many hours at the university were made both productive and enjoyable thanks to my colleagues. In particular, I would like to thank Andreas, Max, Niklas, Alisa, and Roman for their friendship, teamwork, and inspiring discussions. I also gratefully acknowledge the support received during experimental work and the parabolic flight campaigns from Christian Schinz, Thomas Nimmerfroh, and Dr. Michael Kretschmer, as well as the CADMOS Operations Team for their dedicated work during the ISS campaigns.

Last, but by no means least, I would like to thank my family, especially my parents and my brother, for their unwavering belief in me. I am also thankful to Ludi31, whose support, friendship, and love were given selflessly and made my time there truly special. Thank you. Most importantly, I thank Antonia, whose endless love and support have meant everything to me throughout this journey.